Doctoral Dissertation
博士論文

Search For Vacuum Magnetic Birefringence with a high repetitive pulsed magnet

(高速繰り返し磁石を用いた真空複屈折の探索)

A Dissertation Submitted for the Degree of Doctor of Philosophy
December 2020

令和 2 年 12 月博士 (理学) 申請

Department of Physics, Graduate School of Science,
The University of Tokyo
東京大学理学系研究科物理学専攻

Shusei Kamioka
上岡修星

Abstract

This theses reports search for the vacuum magnetic birefringence (VMB) with a high repetitive pulsed magnet. VMB is an anisotropy of the refractive index of the vacuum in the magnetic field. VMB is predicted to be induced by the virtual electron-positron pair in the vacuum. The light new particles which could couple to 2 photons, including ALPs and MCPs, could also induce VMB. VMB is a good prove for the precision test of QED and search for the new physics, but has not been observed yet.

The strongest limit was obtained by using the rotating permanent magnets. In that experiment, the unexpected noise which is not correlated with the magnetic field was observed, and it is found that stronger magnetic field is required to observe the VMB. One of the solutions is the application of the pulsed magnet. In the previous experiment with the pulsed magnet, the effect of the disturbance of the magnet to the optical system was observed, and the slow repetition rate of the magnet resulted in the low statistics.

In this thesis, we proposed the experiment aiming for the first observation of VMB induced by QED with the high repetitive magnet and the high sensitive optical anisotropy detection system. The experimental setup is designed to isolate the optical system from disturbance of the magnet. The operation field of the pulsed magnet is 8.2 T and repetition rate is 0.05 Hz, which is 25 times faster than the previous experiment. The dedicated study is performed for the study of the intrinsic birefringence noise of the optical system at higher frequency region up to 1 kHz, which is important for the experiment with pulsed magnet, and where few studies has been reported. The sensitivity of the optical anisotropy detection system is reached to around 1×10^{-19} [m/$\sqrt{\text{Hz}}$]. The sensitivity is about 5 times better than the sensitivity around 10 Hz which is used in the previous experiment with the permanent magnets. With the developed setup, the search for VMB with the pulsed magnet was performed. With total 26000 pulses, no significant signal was observed. The obtained limit is

$$|k_{\text{CM}}| < 1.8 \times 10^{-20}\ [\text{T}^{-2}]. \tag{1}$$

The strongest magnetic field and the fastest repetition rate of the pulsed magnet as VMB search has been achieved. The statistic is about 100 times larger than the previous experiment with the pulsed magnet. This result shows the establishment of the VMB search with the repetitive pulsed magnet.

Contents

List of Figures

List of Tables

Chapter 1

Introduction

This thesis describes a search for Vacuum Magnetic Birefringence (VMB) using a high-finesse Fabry-Pérot cavity and a high repetitive strong pulsed magnet. VMB is an anisotropy of the refractive index of the vacuum in a magnetic field. This unique property of the vacuum is predicted by quantum electrodynamics (QED). In addition to that, new particles which could couple to 2 photons including Axion-Like-Particles (ALPs) and Milli-Charged Particles (MCPs) also contribute to VMB. In this section, a theoretical background of VMB based on the nonlinear electrodynamics is shown firstly. The contribution from the new physics is also described in Section. 1.3. Previous experiments for VMB search are shown secondly. Finally, the aim of this thesis is described.

1.1 Nonlinear interaction of photons in vacuum

In the classical electromagnetism where superposition principle holds, the light can not interact with each other in vacuum. This is not the case when considering the quantum effect. According to QED, the vacuum is filled with virtual particle and anti-particle pairs which exists very shot time. The interaction between photons could occur mediated by the virtual electron-positron loop in the vacuum. This interaction is expressed by a "box diagram" in Fig. 1.1. In 1930, an effective Lagrangian of electrodynamics including this nonlinear interaction was derived [1]. The Lagrangian is called Eular-Heisenberg Lagrangian and expressed as follows,

$$\mathcal{L}_{\mathrm{EH}} = -\mathcal{F} - \frac{1}{8\pi^2}\int_0^\infty \frac{ds}{s^3}\exp(-m_{\mathrm{e}}^2 s)\left[(es)^2\frac{\mathrm{Re}\cosh\left(es\sqrt{2\left(\mathcal{F}+i\mathcal{G}\right)}\right)}{\mathrm{Im}\cosh\left(es\sqrt{2\left(\mathcal{F}+i\mathcal{G}\right)}\right)}\mathcal{G} - \frac{2}{3}(es)^2\mathcal{F} - 1\right], \tag{1.1}$$

where m_{e} is the mass of electron and $\mathcal{F} = F_{\mu\nu}F^{\mu\nu} = \frac{1}{2}(\boldsymbol{E}^2 - \boldsymbol{B}^2)$ and $\mathcal{G} = F_{\mu\nu}\tilde{F}^{\mu\nu} = \frac{1}{2}(\boldsymbol{E}\cdot\boldsymbol{B})$. When the electromagnetic field is much smaller than critical field, Eular-

Heisenberg Lagrangian can be further approximated as follows,

$$\mathcal{L}_{\mathrm{EH}} = \frac{1}{2}(\boldsymbol{E}^2 - \boldsymbol{B}^2) + A_e[(\boldsymbol{E}^2 - \boldsymbol{B}^2)^2 + 7(\boldsymbol{E}\cdot\boldsymbol{B})^2], \tag{1.2}$$

where a coefficient A_e is

$$A_e = \frac{2\alpha^2\hbar^3}{45\mu_0 m_e^4 c^5} = 1.32 \times 10^{-24}\ [\mathrm{T}^{-2}]. \tag{1.3}$$

The electromagnetic field should satisfy the weak field condition which is defined as follows,

$$E \ll E_{\mathrm{cr}} = \frac{m_{\mathrm{e}}^2 c^3}{e\hbar} = 4.4 \times 10^9\ [\mathrm{V/m}], \tag{1.4}$$

$$B \ll B_{\mathrm{cr}} = \frac{m_{\mathrm{e}}^2 c^2}{e\hbar} = 1.3 \times 10^{18}\ [\mathrm{T}]. \tag{1.5}$$

The first terms of Eq. (1.2) is identical to the classical electromagnetic Lagrangian which leads to classical Maxwell equation. The last term of Eq. (1.2) is understood as the correction to the classical electromagnetism. It contains the nonlinear term of electromagnetic field. This Lagrangian indicates even when the electromagnetic field are small and there is no medium, there exists nonlinear effect of the electromagnetism in the vacuum.

This Lagrangian predicts a lot of unique properties of the vacuum at macro scale including birefringence of the vacuum which is discussed later, dichroism of vacuum [2], diffraction of the light in the vacuum [3] and four wave-mixing in the vacuum [4]. However, so far, no one of them have been observed.

1.2 Vacuum Magnetic Birefringence (VMB)

The refractive index of the vacuum taking into account the quantum effect can be derived by using Eular-Heisenberg Lagrangian. The electric flux density and magnetic field can be calculated as follows,

$$\boldsymbol{D} = \frac{\partial \mathcal{L}_{\mathrm{EH}}}{\partial \boldsymbol{E}}, \tag{1.6}$$

$$\boldsymbol{H} = -\frac{\partial \mathcal{L}_{\mathrm{EH}}}{\partial \boldsymbol{B}}. \tag{1.7}$$

The permittivity tensor ϵ and permeability μ of the medium is defined as follows,

$$\begin{aligned} \epsilon &= \frac{\partial \boldsymbol{D}}{\partial \boldsymbol{E}}, \\ \mu &= \frac{\partial \boldsymbol{B}}{\partial \boldsymbol{H}}. \end{aligned} \tag{1.8}$$

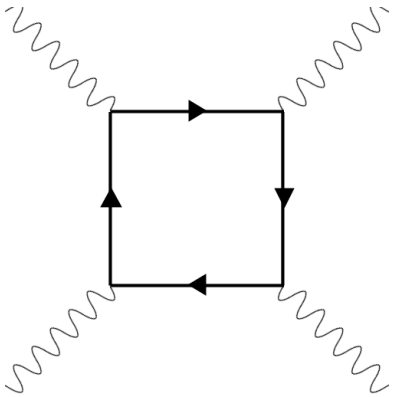

Figure 1.1: Box diagram of QED. The virtual electron-positron pair mediates the interaction between four external photons.

The refractive index tensor is calculated from these values as

$$n = \frac{\sqrt{\epsilon\mu}}{\sqrt{\epsilon_0\mu_0}}, \tag{1.9}$$

where ϵ_0 and μ_0 is the permittivity and permeability of classical vacuum. Refractive index is the dimensionless number which describe the effective speed of the light in the medium.

In 1960s, the refractive index of the vacuum under a slowly varying external magnetic field was calculated [5]. The refractive index of the vacuum is not only shifted from 1, but also have an anisotropy. This is called Vacuum Magnetic Birefringence (VMB). The refractive index parallel to the external magnetic field ($n_\parallel$) and the refractive index perpendicular to the external magnetic field ($n_\perp$) become as follows,

$$n_\parallel = 1 + 7A_eB^2, \tag{1.10}$$
$$n_\perp = 1 + 4A_eB^2. \tag{1.11}$$

The amount of the anisotropy (Δn) is expressed as

$$\begin{aligned} \Delta n = n_\parallel - n_\perp &= 3A_eB^2 \\ &= 4.0 \times 10^{-24} \times (B\ [\mathrm{T}])^2 \\ &\equiv k_{\mathrm{CM}} \times (B\ [\mathrm{T}])^2, \end{aligned} \tag{1.12}$$

where B is the magnetic flux density of eternal magnetic field which is perpendicular to the light pass.

This effect is understood as the magnetization of the vacuum. VMB is originally predicted in 1960s. Since then a lot of experiment including the laboratory experiments and astronomical observations were performed to observe VMB, but it is not observed yet. In Section 1.4, the summary of the previous laboratory experiments is described.

1.3 VMB mediated by new physics beyond the standard model

In addition to the birefringence induced by the virtual electron-positron loop, particles which could couple to 2 photos could also induce VMB as they could intermediate the interaction between light and magnetic field. Their contribution could change the value of VMB from QED calculation. Therefore, measurement of VMB is also sensitive to new physics predicted beyond the standard model.

1.3.1 Axion and ALPs

Axion is the pseudo scalar particle which is introduced to solve the strong CP problem in QCD. The CP violating terms of QCD appears as following. One is originated from the quark mass matrix, and the other is originated from the vacuum structure of QCD. Thus it is natural that the CP of QCD is violated, but so far it is measured that the CP of QCD is not violated at least with the precision of 10^{-10} [6, 7]. This fine-tuning problem is called as a strong CP problem. To solve this problem, it is proposed to introduce an additional global U(1) symmetry called $\mathrm{U_{PQ}}(1)$ to the standard model [8]. This additional symmetry acts to choose preferred vacuum where CP of QCD is not violated. The Axion is a pseudo Nambu-Gold Stone boson generated by the spontaneous breaking of the additional U(1) symmetry [9, 10]. The Axion acquires mass m_{A} by the mixing with π^0.

$$m_{\mathrm{A}} = \frac{m_\pi f_\pi}{f_{\mathrm{A}}} \frac{\sqrt{z}}{1+z} \sim 0.6 \text{ meV} \times \left(\frac{10^{10} \text{ [GeV]}}{f_{\mathrm{A}}} \right), \tag{1.13}$$

where f_{A} is the symmetry breaking scale of the $U_{\mathrm{PQ}}(1)$, m_π is the pion mass, f_π is pion's decay constant, and $z \equiv \frac{m_u}{m_d}$ is the quark mass ratio between u and d [11]. This π^0-mixing introduce the coupling to 2 photons,

$$L_{A\gamma\gamma} = -\frac{1}{4} g_{A\gamma\gamma} F_{\mu\nu} \tilde{F}_{\mu\nu} A, \tag{1.14}$$

where $g_{\mathrm{A}\gamma\gamma}$ is the coupling constant between the axion and photon. It is written as follows,

$$g_{A\gamma\gamma} = \frac{\alpha}{2\pi f_{\mathrm{A}}} C_\gamma \sim 10^{-13} \times \left(\frac{10^{10} \text{ [GeV]}}{f_{\mathrm{A}}} \right), \tag{1.15}$$

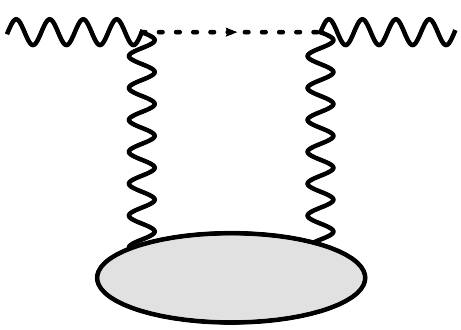

Figure 1.2: Feynman diagram which expresses the contribution of the ALPs to VMB. The ALPs mediated the interaction between light and magnetic field.

where α is fine structure constant. C_γ is the model dependent constant which is written as

$$C_\gamma = \left| \frac{E}{N} - \frac{2}{3}\frac{4+z}{1+z} \right|, \tag{1.16}$$

where E is the electromagnetic anomaly and N is the color anomaly. Depending on the model, C_γ changes between 0.07 and 7. This interaction mediates a mixing of axions and photons in external electromagnetic fields. It is referred to as the Primakoff effect [12].

Axion-Like-Particles (ALPs) are pseudo Nambu-Goldstone bosons. ALPs are predicted by a lot of theories beyond the standard model [13]. In addition to the original QCD axion, they generally arise from the spontaneous breaking of additional global symmetries. ALPs are predicted in many models including supersymmetric theories, string theories, and conformal standard models [14–16].

Generally, ALPs could couple to 2 photons. The interaction can be expressed as

$$L_{a\gamma\gamma} = -\frac{1}{4} g_{a\gamma\gamma} F_{\mu\nu} \tilde{F}_{\mu\nu} a \tag{1.17}$$

where a is ALPs whose mass is m_a and $g_{a\gamma\gamma}$ is coupling constant between ALPs and photon. There is no specified relation between ALPs's mass and their coupling between photons. Therefore, ALPs search are conducted to cover whole $m_a - g_{a\gamma\gamma}$ plane.

As ALPs couple to 2 photons, they could contribute to VMB via a process expressed in Fig. 1.2 [17]. From the diagram, the birefringence induced by ALPs is calculated as follows,

$$\Delta n_{\mathrm{ALPs}} = \frac{g^2_{\mathrm{ALPs}} B^2}{2m^2_{\mathrm{ALPs}}} \left(1 - \frac{\sin 2x}{2x} \right), \tag{1.18}$$

where x is defined as $x = \frac{L_{\mathrm{B}} m^2_{\mathrm{ALPs}}}{4\omega}$. L_B is the length of the magnetic field, and ω is the angular frequency of the electric field. Fig. 1.3 shows the summary of the previous ALPs search by various terrestrial experiments around $10^{-4} < m_a < 1$ eV.

Around these mass region, the other popular method of ALPs search is Light-Shinning through the Wall (LSW) method [18]. LSW method measures the number of photons which pass through the photon-shielding wall. The photons produced by the external light source are injected to the photon shielding wall and they are converted to a real ALPs by the magnetic field. ALPs can pass though the wall as they could interact with matters very weakly. After ALPs pass through the wall, they are re-converted to photon by magnetic field and then detected by the photon detector after the wall. The major difference between LSW and VMB as ALPs search is that LSW has the sensitivity to real ALPs where the birefringence could be induced by real and virtual ALPs. This difference results in the different mass dependence of the ALPs sensitivity. Because of this difference, VMB search has the better sensitivity to ALPs at around $10^{-2} < m_a < 1^{-1}$ eV.
Another terrestrial experiment searching for the ALPs around these mass regions is search for the four-wave mixing in the vacuum [19]. In this experiment, the photon-photon scattering of the pulse laser mediated by the ALPs is searched. The resonance of the cross section of the photon-photon scattering via s-channel exchange of ALPs is the signal. The signal is also enhanced by injecting another stimulated laser to the collision point of the laser. This experiment has the sensitivity in the narrow region around 0.1 eV which is determined by the energy of the lasers. The advantage of ALPS search with the VMB experiment against this method is that VMB has sensitivity against ALPs in the larger mass range.

The stringest limits at around $10^{-2} < m_a < 1^{-1}$ eV so far is mainly obtained by PVLAS experiment which is one of the VMB search experiments [18]. The red line in Fig. 1.3 is the obtained limit when VMB sensitivity reaches the QED expectation value which is the benchmark sensitivity of VMB experiment.

1.3.2 Milli-Charged Particles

Milli-Charged particles are non-quantized small charged particle. A lot of models beyond the standard model have additional U(1) symmetry. The charge of this new symmetry is referred to as paracharge. In general, it is assumed that the SM particles don't have paracharge, thus the particles under additional U(1) symmetry don't interact directly with ordinary SM particles. From this reason, it is called "hidden sector" where such particles assumed to be resided, whereas our world is called "visible sector" [24]. The only interaction between hidden sector and visible sector is realised by a mixing of U(1) gauge boson of each sector with mixing angle χ. Particles which has paracharge g in hidden sector can be seen as a particle which have an electric charge $\beta = \chi g$ from visible sector [25]. These particles in the hidden sector are called Milli-Charged Particles (MCPs).

MCPs are searched in the parameter space spanned by the mass and charge [26]. They are constrained by a lot of experiment including direct searches [27–29], indirect observations [30], the CMB observation [31]. As MCPs could also interact with photons, they contribute to VMB [32]. The contribution depends on whether they are fermion or boson. In each case, VMB induced by MCPs are calculated as

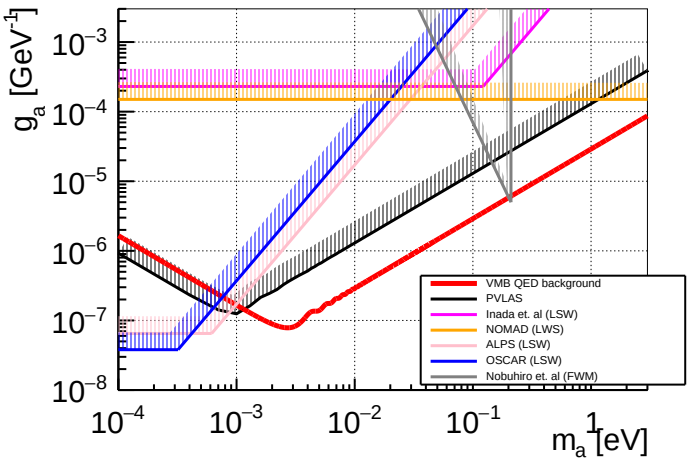

Figure 1.3: Summary of the excluded region of ALPs by terrestrial experiments. The red line is the QED background of VMB method. Black: exclusion region by PVLAS experiment [18]. Exclusion regions by various LSW method (NOMAD experiment [20], ALPS experiment [21], OSCAR experiment [22], Inada et. al [23]), and the exclusion regions by four wave mixing (Nobuhiro et. al [19]) are also shown.

follows,

$$\Delta n^{\mathrm{B}} = \begin{cases} -\dfrac{3}{2} A_\beta B^2 & \text{for } \chi \ll 1 \qquad (1.19) \\ \dfrac{135}{28} \dfrac{\pi^{1/2} 2^{1/3} \left(\Gamma\left(\frac{2}{3}\right)\right)^2}{\Gamma\left(\frac{1}{6}\right)} \chi^{-\frac{4}{3}} A_\beta B^2 & \text{for } \chi \gg 1 \qquad (1.20) \end{cases}$$

$$\Delta n^{\mathrm{F}} = \begin{cases} 3 A_\beta B^2 & \text{for } \chi \ll 1 \qquad (1.21) \\ -\dfrac{135}{14} \dfrac{\pi^{1/2} 2^{1/3} \left(\Gamma\left(\frac{2}{3}\right)\right)^2}{\Gamma\left(\frac{1}{6}\right)} \chi^{-\frac{4}{3}} A_\beta B^2 & \text{for } \chi \gg 1. \qquad (1.22) \end{cases}$$

χ and A_β are expressed as

$$\chi = \frac{3\hbar\omega\beta eB\hbar}{2\left(m_\beta^{\mathrm{B,\,F}}\right)^3 c^4}, \quad A_\beta = \frac{2\beta^4\alpha^2\hbar^3}{45\mu_0\left(m_\beta^{\mathrm{B,\,F}}\right)^4 c^5}, \qquad (1.23)$$

where B denotes boson and F denotes fermion.

1.4 Previous experiments

1.4.1 Laboratory experiments

So far, a lot of experiments to observe VMB have been performed. They are categorized by the type of magnets to induce VMB. As discussed in Section 2, the sensitivity of VMB search depends on square of the transverse magnetic field and field length. Thus, requirements for the magnet are long field length and strong transverse magnetic field. It is also required to modulate the magnetic field to separate VMB signal from static birefringence of materials. In this section, the previous experiments are summarized. The obtained limit of k_{CM} in the previous experiment is shown in Fig. 1.7 , and the experimental parameters are summarized in Table. 1.1.

VMB searches with a superconducting magnet ($\sim$ 2007)

VMB search with superconducting magnet had performed by PVLAS experiment [33, 34]. Figure 1.4 shows a schematic view of the experimental setup [35]. They use 5.5 T and 1.0 m superconducting magnet. To modulate the magnetic field, the cryostat for the superconducting magnet was rotated at 0.3 Hz. This experiment ended up with the observation of systematic signals appeared at the signal frequency and limited measurement time by availability of liquid helium for the magnet. So far, the origin of the systematic signal has not been understood [35].

VMB searches with a permanent magnet (2009 $\sim$ 2016)

VMB search with permanent magnet has also been performed by PVLAS experiment [36]. Figure 1.5 shows the schematic view of the experimental setup [35]. They use 2.5 T and 1.6 m permanent dipole magnet. Magnets are rotated mechanically around 5 Hz and signal appears at the second harmonics of the rotation frequency. The advantage of their method is they do not need any cooling apparatus to operate the magnet. High duty rate and less noise from the magnetic system can be expected.

From 2014 to 2016, they performed VMB search with total live time of 3 months. The obtained limit is about 10 times above the QED calculation [35]. This experiment has achieved the best sensitivity for VMB. The sensitivity is limited by the unexpected wide band noise excess. They concluded the birefringence noise is induced by the optical system. [37].

VMB searches with a pulsed magnet (2007 $\sim$)

A VMB search with pulsed magnet has been performed by BMV experiment [38]. Figure 1.6 shows the schematic view of the experimental [38]. The filed length is 0.13 m and the peak magnetic field is 6 T. The repetition rate of their magnet is 6 pulse/hour. The advantage of this method is that stronger magnetic field compared to other method can be used and the signal would appear at higher frequency where less birefringence noise can be expected.

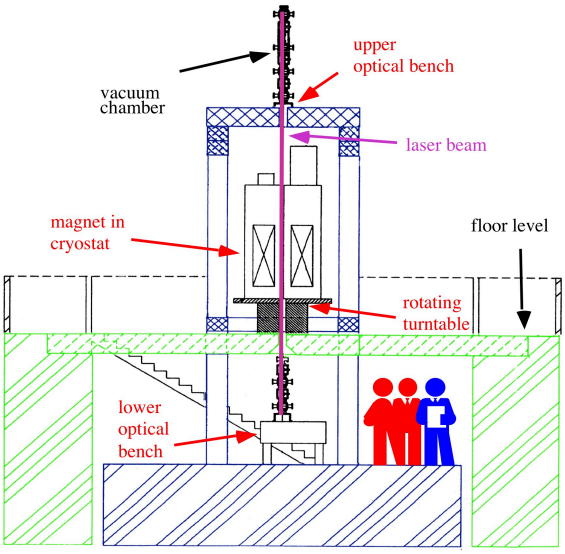

Figure 1.4: Experimental setup of PVLAS experiment with the superconducting magnet [35]. The filed length is 1.0 m and the peak magnetic field is 5.5 T. The magnet is rotated around 0.3 Hz.

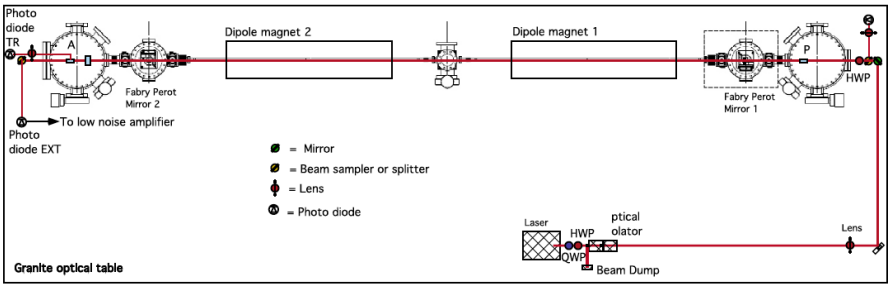

Figure 1.5: Experimental setup of PVLAS experiment with permanent magnet [35]. The filed length is 1.6 m and the peak magnetic field is 2.5 T. The magnet is rotated around 10 Hz.

The disadvantage is that the pulsed magnet generates large acoustic and mechanical noise. They observed the birefringence noise due to the acoustic noise induced by the pulsed magnetic field.

1.4.2 Astrophysical observations

The strongest magnetic field in the universe known so far is the magnetor whose magnetic field is typically 10^8 T. As magnetors also radiate X-ray or γ-ray, the

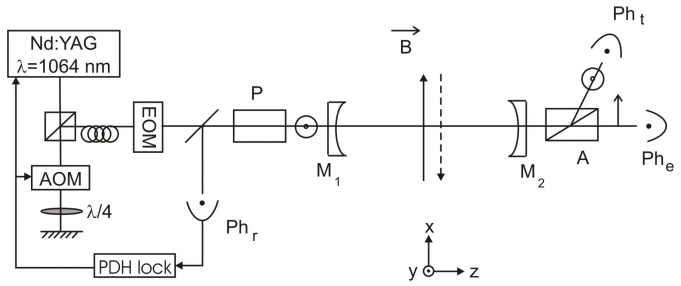

Figure 1.6: Experimental setup of BMV experiment [38]. The filed length is 0.13 m and the peak magnetic field is 6 T. The repetition rate is 6 pulse/hour.

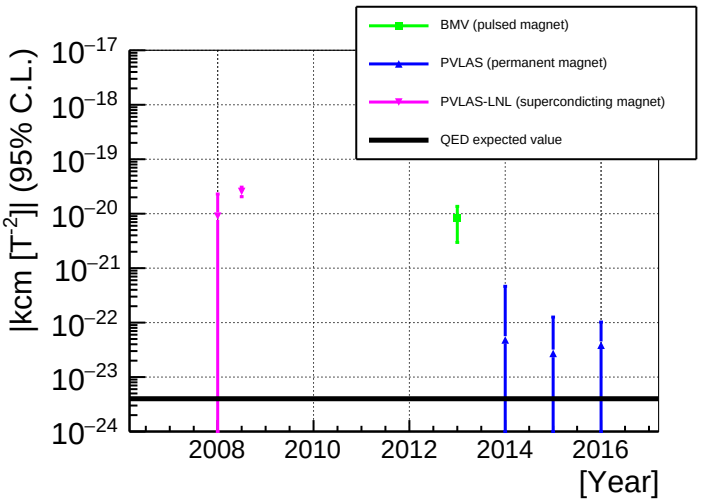

Figure 1.7: Limit on k_{CM} obtained by the previous experiments. 95% confidence level of k_{CM} obtained by the previous experiments is shown chronologically. The detail of each experiment are explained in Chapter 1.4.

measurement of the polarization of the radiation from the magnetors can also be used to search for VMB. In 2016, it is reported that from the measurement of the polarization from a magnetor called RX-J1856.5-3754, the evidence for VMB has observed [39]. They measured the polarization of the radiation whose wavelength is 555 nm and calculate its polarization degree averaged by the phase. The measured polarization degree is $16.43\% \pm 5.26\%$. They compered the result with the theoretical models. It is concluded that the observed polarization degree favours the model including VMB. However, other group pointed out that depending on the

Table 1.1: Summary the experimental parameters of the previous experiment

Type of the magnet	Superconducting	Permanent	Pulse
Group	PVLAS	PVLAS	BMV
B^2_{eff} [T^2]	30, 5.3	6.5	20
Field length [m]	1.0	1.6	0.137
Signal frequency	0.6 Hz	$\sim$ 10 Hz	$\sim$ 100 Hz
Statistics	63500 s	60 days	0.3 s (100 pulses)

model of the radiation from the magnetor, the observed result can be reproduced even when the effect of VMB is not included [40].

1.5 Aim of this work

The science target of this experiment is the first observation of VMB with high repetitive strong pulsed magnet. As the demonstration of the principal of the experimental method, the aims of this work are summarized as following.

Establishment of the VMB search with high repetitive pulsed magnet

From the result of the previous experiment and the magnetic field dependence of dependence of VMB, it is clear that stronger magnetic field is necessary to observe to the VMB induced by QED. One of the solutions is the pulsed magnet. The world record of the peak magnetic field of the pulsed magnet is more than 80 T [41].

The previous experiment reported the effect of the disturbance to the optical cavity due to the pulsed magnet. The development of the optical system dedicated to the vibration reduction and suppression of the disturbance to the optical system, and establishment of the stable operation of the pulsed magnet with the optical system is a purpose of this work.

Another merit of this experiment is the application of the high repetitive pulsed magnet to the VMB search. The disadvantage of the pulsed magnet is its slow repetition rate due to the joule heating. To overcomes this disadvantage, a compact and short pulse magnet is selected to reduce the joule heating. The target repetition rate is 0.05 Hz which is 30 times faster than the previous experiment. As the sensitivity scales with square root of the numbers of generated pulses, this repetition rate gives 5 times better sensitivity than the previous experiment even when the magnetic field and field length are the same.

Investigation of the birefringence noise at higher frequency

PVLAS experiment observes unexpected birefringence noise [37] which is not correlated with the magnetic field. The origin of the noise is not understood.

So far, the study of the birefringence noise is mainly performed low frequency typically up to 25 Hz, which is important for the experiment with permanent magnet. Above the frequency, only limited study has been reported [42]. In the experiment with pulsed magnet, the noise level around several hundreds hertz becomes important for the sensitivity. In this experiment, the dedicated study of the evaluation of the birefringence noise up to ~ 1 kHz is performed. The frequency response of the possible noise source in the homodyne detection scheme are derived theoretically taking the birefringence of the mirrors, and its contribution is evaluated experimentally. To obtain the new knowledge of the birefringence noise at higher frequency is another aim of this work.

Chapter 2

VMB search with pulsed magnet

This section describes the experimental method of VMB search with pulsed magnets. First, the basic idea of polarimetry to measure the birefringence is introduced. After that, a Fabry-Pérot cavity is introduced as optical pass multiplier and the basic ideas of a pulsed magnet is introduced. Finally, the possible noise source and the target sensitivity for the observation of VMB effect predicted by QED is discussed.

2.1 Overview of the experimental method

Figure 2.1 shows the schematic view of the VMB search with a pulsed magnet. A pulsed magnet is used to induce VMB by a strong magnetic field. The anisotropy of the refractive index is measured as a polarization change (ellipticity) of the light traveling through the magnetic field region. A polarizer and an analyzer are placed with cross-nicol configuration to measure the polarization change. The light which pass through the analyzer is called as the extraordinary light (I_e) and which do not pass is called the ordinary light (I_t). Ellipticity is defined as the ratio between I_e and I_t. The polarization angle of the polarizer is fixed to 45° against the direction of the magnetic field. A Fabry-Pérot cavity which made with 2 high reflective mirrors is placed outside the magnetic field region. It is used as an optical pass length multiplier to enhance the interaction region. The enhancement is proportional to the factor called as finesse F. It is also used to generate a static ellipticity Γ. The ellipticity is written as follows,

$$I_e/I_t = \Gamma^2 + 2\Gamma\frac{2FL_BB^2(t)}{\lambda}k_{\mathrm{CM}}, \tag{2.1}$$

where k_{CM} expresses the coefficient of VMB which is defined in Eq. 1.12. In the following section, the detailed discussion of the experimental method is described.

2.2 Polarimetry in this measurement

The basic idea of birefringence measurement in this experiment is to measure the polarization change of the laser with homodyne detection. The basic setup of this method is shown in Figure 2.2. One pair of a polarizer and an analyzer are placed with Cross-Nicol configuration. Between the polarizer and the analyzer, the target birefringence material where birefringence has time dependent and a wave plate whose properties is already known is placed. The angle between polarization axis of the polarizer and the fast axis of the birefringence material is fixed to 45° and the angle between the polarization axis of the polarizer and the fast axis of the wave plate is fixed to θ.

To calculate the change of the polarization, Jones calculus is used. A Jones vector expresses the phase and amplitude of the electric field in 2-dimensional space. The each component of the Jones vector expresses the electric field of two orthogonal polarization states. The Jones matrices are the operators which acts on the Jones vectors. The Jones matrices express the operation of the optical elements against the electric field. X-axis is defined parallel to the polarization axis of the polarizer and input laser travels along z-axis.

The Jones vector of the input laser after the polarizer $\boldsymbol{E}_{\rm in}$ is

$$\boldsymbol{E}_{\mathbf{in}} = \begin{pmatrix} 1 \\ 0 \end{pmatrix}. \tag{2.2}$$

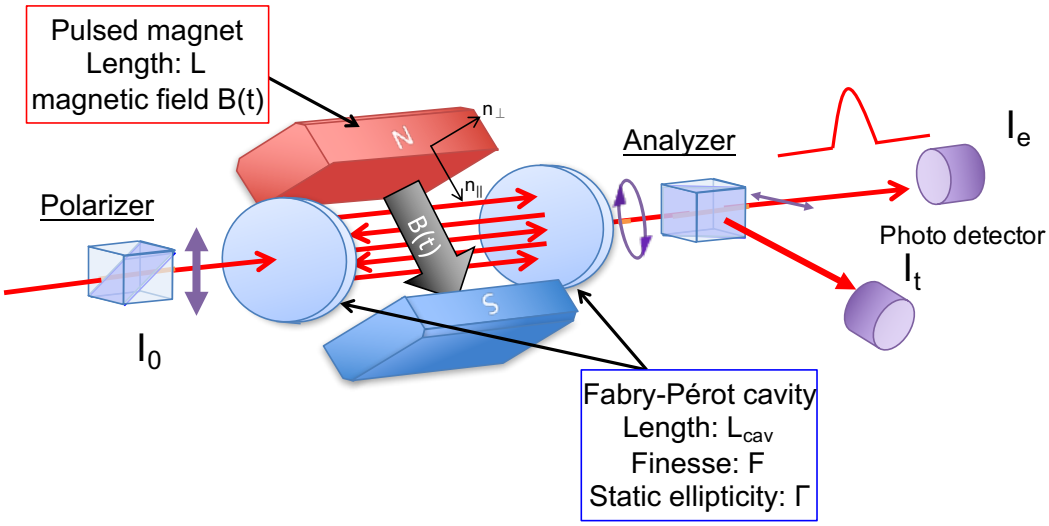

Figure 2.1: Overview of the experimental setup to measure VMB. A strong pulsed magnet is used to induce large Δn. A Fabry-Pérot cavity is used to enhance the effective interaction length and to induce the static birefringence. From the output power of the analyser, the ellipticity is measured.

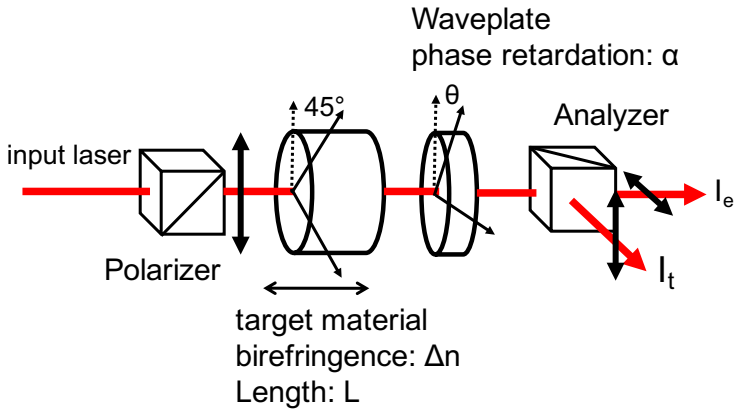

Figure 2.2: Basic setup of the polarimetry for this experiment. The target material whose birefringence is Δn, and length is L is placed between polarizers. A waveplate is used to induce the static birefringence. The power ratio of the output of the analyser is used to measure the ellipticity.

By assuming the phase retardation of the waveplate is α, the Jones matrix of the wave plate $W_{\rm wp}$ is

$$W_{\rm wp} = \begin{pmatrix} e^{-i\alpha/2}\cos^2(\theta) + e^{i\alpha/2}\sin^2(\theta) & -i\sin(\alpha/2)\sin(2\theta) \\ -i\sin(\alpha/2)\sin(2\theta) & e^{-i\alpha/2}\sin^2(\theta) + e^{i\alpha/2}\cos^2(\theta) \end{pmatrix}. \quad (2.3)$$

Assuming the length of the target material is L and its birefringence is $\Delta n(t)$, the phase retardation $\Psi(t)$ can be written as

$$\Psi(t) = \pi\frac{\Delta n(t) L}{\lambda}, \quad (2.4)$$

where λ is a wavelength of input laser. Then the Jones Matrix of the birefringence material X is

$$X = \begin{pmatrix} 1 & -i\Psi(t) \\ -i\Psi(t) & 1 \end{pmatrix}. \quad (2.5)$$

The analyser can separate the light whose polarization is perpendicular to the polarization angle of analyser, called extraordinary light $\boldsymbol{E_e}$, and whose polarization angle is parallel to the polarization angle, called ordinary light $\boldsymbol{E_t}$.

The Jones matrix from the input port of the Analyser to output port for the extraordinary light is

$$A_e = \begin{pmatrix} 0 & 0 \\ 0 & 1 \end{pmatrix}. \quad (2.6)$$

The Jones matrix from the input port of the Analyser to output port for the ordinary light is

$$A_t = \begin{pmatrix} 1 & 0 \\ 0 & 0 \end{pmatrix}. \quad (2.7)$$

By using these matrices, the amplitude of ordinary and extraordinary light can be calculated. Hereafter, it is also assumed that $1 \gg \alpha \gg \frac{\alpha}{2}\sin(2\theta) \gg \Psi$. The Jones vector of the ordinary light is

$$\begin{aligned} \boldsymbol{E}_t &= A_t W_{\mathrm{wp}} X \boldsymbol{E}_{in} \\ &\sim \begin{pmatrix} 1 - i\frac{\alpha}{2}\cos(2\theta) \\ 0 \end{pmatrix}. \end{aligned} \tag{2.8}$$

The amplitude of the extraordinary light is

$$\begin{aligned} \boldsymbol{E}_e &= A_e W_{\mathrm{wp}} X \boldsymbol{E}_{in} \\ &= \begin{pmatrix} 0 \\ i\Psi(e^{-i\alpha/2}\cos^2(\theta) + e^{i\alpha/2}\sin^2(\theta)) + i\sin(\alpha/2)\sin(2\theta) \end{pmatrix} \\ &\sim \begin{pmatrix} 0 \\ i\Psi + i\frac{\alpha}{2}\sin(2\theta) \end{pmatrix}. \end{aligned} \tag{2.9}$$

The ellipticity is defined as the ratio of the power of extraordinary light I_e and ordinary light I_t

$$\begin{aligned} \frac{I_e}{I_t}(t) &= [\frac{\alpha}{2}\sin(2\theta) + \Psi(t)]^2 \\ &\sim \Gamma^2 + 2\Gamma\Psi(t) \\ &= \Gamma^2 + 2\Gamma\pi\frac{L}{\lambda}\Delta n(t). \end{aligned} \tag{2.10}$$

In the second line of the above expression, the static ellipticity is defined as $\Gamma^2 = \left(\frac{\alpha}{2}\sin(2\theta)\right)^2$. This expression shows that the linear term of the birefringence appears as a time-dependent term of the measured ellipticity. In the case of VMB measurement, from the measured ellipticity during applying magnetic field, k_{CM} can be calculated as

$$k_{\mathrm{CM}} = \frac{\lambda}{2\pi\Gamma L B^2(t)}\frac{I_e}{I_t}(t). \tag{2.11}$$

2.3 Signal enhancement with a Fabry-Pérot Cavity

In this section, it is shown that a Fabry-Pérot cavity can enhance the polarization change. The basic properties and the definition of term about a Fabry-Pérot cavity is explained in appendix A.
The difference from the previous section is that 2 high reflective mirrors are placed before and after the target material.

Again, by using Jones matrix, ellipticity can be calculated. The amplitude transmittance and reflectivity of 2 mirrors are t and r respectively, and the length

between 2 mirrors is $L_{\rm cav}$. The Jones matrix to express the trip from one mirror to the other is expressed as

$$\begin{aligned} R &= re^{i2\pi\nu\frac{L}{c}}\boldsymbol{I} \\ &\equiv re^{i\phi}\boldsymbol{I}, \end{aligned} \tag{2.12}$$

where ϕ is an acquired phase for each trip between 2 mirrors and ν is a frequency of the input laser. The Jones matrix which represent the input to the first mirror to the second mirror is expressed as

$$T_{\rm in} = te^{i\phi}\boldsymbol{I}. \tag{2.13}$$

The Jones matrix which represents the output from the second mirror is expressed as

$$T_{\rm out} = t\boldsymbol{I}. \tag{2.14}$$

The Jones matrix of the light transmitted from the second mirror after n-th round trip between 2 mirrors is $T_{\rm out}(RX)^{2n}XT_{\rm in}$. The output amplitude from the second mirror is a sum of all n-th round tripped light. Therefore, the amplitude of the ordinary light is

$$\begin{aligned} \boldsymbol{E}_t &= A_t W_{\rm wp} T_{\rm in} T_{\rm out} \sum_n^{\infty} (RX)^{2n} X \boldsymbol{E}_{in} \\ &= A_t W_{\rm wp} t^2 e^{i\phi} (\boldsymbol{I} - (RX)^2)^{-1} X \boldsymbol{E}_{in} \\ &\sim A_t W_{\rm wp} \frac{t^2 e^{i\phi}}{1 - r^2 e^{i2\phi}} \begin{pmatrix} 1 & \frac{-ir^2 2\Psi}{1-r^2e^{i2\phi}} \\ \frac{-ir^2 2\Psi}{1-r^2e^{i2\phi}} & 1 \end{pmatrix} \boldsymbol{E}_{in} \\ &= \begin{pmatrix} \frac{t^2 e^{i\phi}}{1-r^2e^{i2\phi}}(1 - \frac{\alpha}{2}\sin(2\theta)) \\ 0 \end{pmatrix}. \end{aligned} \tag{2.15}$$

When a Fabry-Pérot cavity is on the resonance, ϕ should fulfill the condition of $\phi = m\pi$ ($m \in \mathbb{Z}$). Thus the amplitude of the ordinary light during the resonance is

$$\boldsymbol{E}_t = \begin{pmatrix} \frac{t^2}{1-r^2}(1 - \frac{\alpha}{2}\sin(2\theta)) \\ 0 \end{pmatrix}. \tag{2.16}$$

The amplitude of the extraordinary light when cavity is on the resonance is

$$\begin{aligned} \boldsymbol{E}_e &= A_e W_{\rm wp} T_{\rm in} T_{\rm out} \sum_n^{\infty} (RX)^{2n} X \boldsymbol{E}_{in} \\ &= \begin{pmatrix} 0 \\ \frac{t^2}{1-r^2}\left(i\frac{2r^2\Psi}{1-r^2} + i2\sin(2\theta)\right) \end{pmatrix}. \end{aligned} \tag{2.17}$$

The acquired ellipticity is

$$\frac{I_e}{I_t}(t) = [\frac{\alpha}{2}\sin(2\theta) + \frac{2r^2\Psi(t)}{1-r^2}]^2. \tag{2.18}$$

As discussed in Appendix A, Finesse is defined as

$$F \sim \frac{\pi r^2}{1-r^2}. \tag{2.19}$$

By substituting this expression and Γ to Eq. (2.18), the ellipticity with a Fabry-Pérot cavity is derived as follows,

$$\begin{aligned}\frac{I_e}{I_t}(t) &= [\Gamma + \frac{2F}{\pi}\Psi(t)]^2 \\ &\sim \Gamma^2 + 2\Gamma\frac{2F}{\pi}\Psi(t) \\ &= \Gamma^2 + 2\Gamma\frac{2FL}{\pi\lambda}\Delta n(t).\end{aligned} \tag{2.20}$$

Compared this result with the ellipticity without a Fabry-Pérot cavity, the ellipticity becomes $\frac{2F}{\pi}$ times larger. This can be understood as the incident light travels effectively $\frac{F}{\pi}$ roundtrips between 2 mirrors before it comes out from the second mirror. The effective length of the target material becomes $\frac{2F}{\pi}$ times longer.

With the manufactured mirror, the finesse more than 300,000 is established, thus the expected enhancement of the ellipticity signal is more than 200,000.
It should be noted that the real mirrors have a small birefringence [43] and it is used to generate the static birefringence Γ. Due to the birefringence of the mirrors, the discussion about polarimetry with a Fabry-Pérot cavity is needed to be modified. The detailed discussion is shown in Appendix B.

2.4 Frequency response of the Fabry-Pérot cavity

In this section, the response of VMB signal against the time-dependent magnetic field is discussed.

The output of the extraordinary electric field of Fabry-Pérot cavity at the given time t is the sum of the extraordinary electric field generated before t.

$$E_e^{out}(t) = it_m \sum_j \left((r_m^2 e^{i\omega\frac{2L}{c}})^j \times 2\Psi(t - \frac{2L}{c}j) E_t(t - \frac{2L}{c}j) \right). \tag{2.21}$$

where $E_t(t)$ is electric field of ordinary light inside the cavity at t, and $2\psi(t - j\frac{2L}{c})E^t(t - \frac{2L}{c}j)$ is the amplitude of the extraordinary light generated at $t - j\frac{2L}{c}$. r_m and t_m is the reflectivity and transmittance of the mirror.

When cavity is on a resonance, $e^{i\omega\frac{2L}{c}j} = 1$ and $E_t(t) = E_t(t - \frac{2L}{c}j)$. By performing Fourier transformation to $\Psi(t)$, the above equation is re-written as

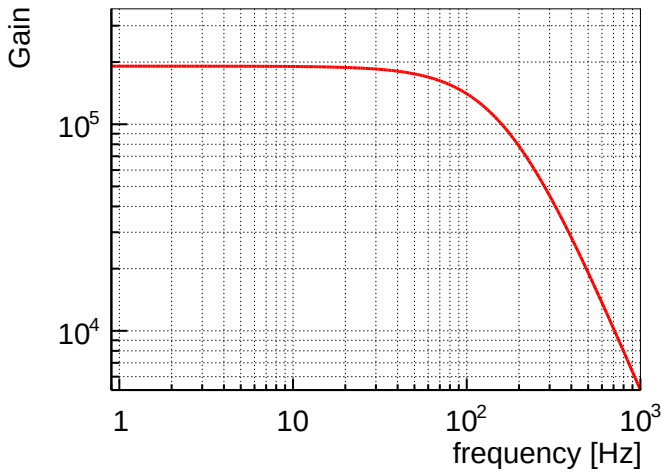

Figure 2.3: Example of the transfer function of Fabry-Pérot cavity against VMB signal when finesse is 300,000 and cavity length is 1.5 m.

$$\begin{aligned} E_e^{out}(t) &= iE_t t_m \Sigma (r_m^2)^j \times \int d\Omega 2\Psi(\Omega) e^{-i(t-j\frac{2L}{c})\Omega} \\ &= iE_t t_m \times \int d\Omega 2\Psi(\Omega) e^{-it\Omega} \times \frac{1}{1-r_m^2 e^{-i\frac{2L}{c}\Omega}} \\ &\sim iE_t \frac{t_m}{1-r_m^2} \times \int d\Omega 2\Psi(\Omega) e^{-it\Omega} \times \frac{1}{1+\frac{r_m^2}{1-r_m^2} i\frac{2L}{c}\Omega} \\ &\propto \int d\Omega \frac{1}{1+i\frac{\Omega}{\frac{\pi c}{2LF}}} \Psi(\Omega) e^{-it\Omega}. \end{aligned} \tag{2.22}$$

The last line can be interpreted that Fabry-Pérot cavity acts as a 1st order low-pass filter to the VMB signal and its cutoff frequency is $f_c = \frac{c}{4FL}$. As an example, the transfer function of Fabry-Pérot cavity to the generated birefringence inside the cavity is shown in Fig. 2.3 when F = 300,000 and L = 1.5 m.

This calculation should be modified to take into account the mirror birefringence of the mirrors. The detailed discussion is shown in Appendix B.

2.5 Noise Budget

In this section, possible noise sources are discussed quantitatively. Hereafter, we discuss the sensitivity about optical pass difference between 2 polarization which

is the unit of the length. The optical pass length difference is defined as

$$\Delta L_\psi \equiv L \times \Delta n = \frac{\lambda}{2F}\frac{I_e}{2\Gamma I_t} \tag{2.23}$$

As the relative optical pass difference between 2 polarization is concerned, fluctuations of the absolute length of the optical cavity does not become the noise source. This is an advantage of this method, as cavity length fluctuation by thermal noise would not appears as noises in this experiment unlike other optical experiment.

The main noise sources come from the shot noise, the frequency noise, the intensity noise and the detector noise.

Shot noise

The fluctuation of the current on a photodiode for the signal detector obeys Poisson distribution depending on the DC current on the photo diode. This is called shot noise. When laser intensity to the photodiode is I, electric current on the photodiode is $i = qI$ where q [A/W] is the efficiency of the photodiode. In this situation, the fluctuation of the current Δi is

$$\Delta i = \sqrt{2eqI}\ [A/\sqrt{\mathrm{Hz}}], \tag{2.24}$$

where e is elementary charge.
By inserting this expression to L_ψ, the optical pass length difference noise due to the shot noise can be calculated as,

$$\begin{aligned}\Delta L_\psi &= \frac{\lambda}{2F} \times \frac{\Delta I_e}{2\Gamma I_t} \\ &= \frac{\lambda}{2F} \times \frac{\frac{\Delta i_e}{q}}{2\Gamma I_t} \\ &= \frac{\lambda}{2F} \times \frac{\sqrt{2e\Gamma^2 I_t/q}}{2\Gamma I_t} \\ &= \frac{\lambda}{2F} \times \sqrt{\frac{e}{2qI_t}}\ [\mathrm{m}/\sqrt{\mathrm{Hz}}].\end{aligned} \tag{2.25}$$

Intensity noise

The fluctuation of intensity inside the Fabry-Pérot cavity could also become a noise source. When we denote the relative intensity noise of the ordinary light as RIN_{I_t}, the contribution of the intensity noise to the optical pass length difference is written as follows when the interested frequency region is below the cut-off frequency of the Fabry-Pérot cavity,

$$\begin{aligned}\Delta L_\psi &= \frac{\lambda}{2F} \times \frac{I_e}{2\Gamma I_t} \times \frac{\Delta I_t}{I_t} \\ &= \frac{\lambda}{2F} \times \frac{RIN_{I_t} \times I_e}{2\Gamma I_t} \\ &= \frac{\lambda}{2F} \times \Gamma \times \frac{RIN_{I_t}}{2}.\end{aligned} \tag{2.26}$$

Frequency noise

As discussed in Appendix B.2, the frequency noise ν Hz/$[\sqrt{\text{Hz}}]$ appears as the intensity noise of the extraordinary light when the Fabry-Pérot cavity has birefringence. Below the cut-off frequency of the Fabry-Pérot cavity, it can be written as

$$\Delta I_e/I_e = \frac{4\frac{F}{\pi}\alpha}{1-(\frac{F}{\pi}\alpha)^2} \times \frac{\nu}{\nu_{\text{FWHM}}}, \tag{2.27}$$

where α [rad] is the phase delay during the one round trip inside the cavity due to the birefringence of the mirrors, and ν_{FWHM} is the FWHM of the resonance curve of a Fabry-Pérot cavity.

The contribution of the frequency noise to the birefringence noise can be written as follows,

$$\begin{aligned}\Delta L_\psi &= \frac{\lambda}{2F} \times \frac{I_e}{2\Gamma I_t} \times \frac{\Delta I_e}{I_e} \\ &= \frac{\lambda}{2F} \times \frac{\Gamma}{2} \times \frac{4\frac{F}{\pi}\alpha}{1-(\frac{F}{\pi}\alpha)^2} \times \frac{\nu}{\nu_{\text{FWHM}}}\end{aligned} \tag{2.28}$$

Detector noise

When the signal of the photodetector has the current noise Δi_{PD} A/$[\sqrt{\text{Hz}}]$, this could also become the noise source. Below the cut-off frequency, its contribution can be written as follows,

$$\Delta L_\psi = \frac{\lambda}{2F} \times \frac{\Delta i_{\text{PD}}}{2q\Gamma I_t} \tag{2.29}$$

The design sensitivity of this experiment is calculated and discussed in Section 2.8.

2.6 Pulsed magnet

In this section, the principle of the pulsed magnet [44] and its advantages for the VMB experiment is discussed.

2.6.1 Basic properties and pulse shape

Figure 2.4 shows the equivalent circuit of the pulsed magnet system. A pulsed magnet is consisted with the resistance and the inductance. The magnet is connected to the capacitor through a switch. When switch is closed, the electric charge stored in the capacitor flows to the pulsed magnet. By solving the circuit equation, the current flows in the magnet becomes

$$I_{\text{coil}} = V_0\sqrt{\frac{C}{L}}e^{-\frac{R}{2L}t}\sin\frac{t}{\sqrt{LC}}. \tag{2.30}$$

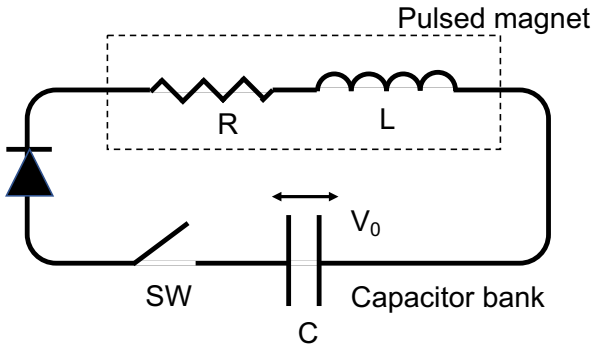

Figure 2.4: Schematic view of the magnet system. It is consisted of a pulsed magnet and a capacitor bank.

At the coil, the magnetic field proportional to the $I_{\rm coil}$ is generated.

$$B_{\rm coil} = g_{\rm eff} I_{\rm coil}, \tag{2.31}$$

where $g_{\rm eff}$ [T/A] is the field efficiency. Field efficiency depends on the detailed structure of the coil. Typically, the circuit is designed so that the current flows in one direction. Thus, the magnetic field becomes pulsed shape rather than damped oscillation. The signal shape is proportional to the square of the pulsed magnetic field when ignoring the cutoff of a Fabry-Pérot cavity. A typical shape and spectrum of the square of the magnetic field are shown in Fig. 2.5. The assumed parameters are $C = 6$ mF and $L = 80$ μH. In the previous experiment with rotating magnets, the VMB signal appears at around 10 Hz. Compared with that, the VMB signal with the pulsed magnet has higher frequency components. Thus, the sensitivity is less affected by the optical pass length difference noise at the lower frequency components where the observed unexpected noise becomes larger in the previous experiment. This is first advantage of the pulsed magnet.

The maximum magnetic field of the pulsed magnet are limited by the destruction of the coil by the Maxwell stress. For a single Cu-wire coil, the maximum magnetic field is roughly calculated to be 20 T. This magnetic field cannot be obtained by other DC magnets. Stronger magnetic field can be obtained by using other wire materials. This is the second advantage of the pulsed magnet.

2.6.2 Repetition rate

As the pulsed magnet has the non-zero resistance, the joule heat is generated at the same time with the magnetic field. This heat generation ends up with the increase of the temperature of the coil and the increase of the resistance. Too high temperature leads to the destruction of the coil. Magnets are needed to be cooled down during the pulse intervals. This time scale limits the repetition rate. Typical repetition rate of the pulsed magnet is 1 mHz.

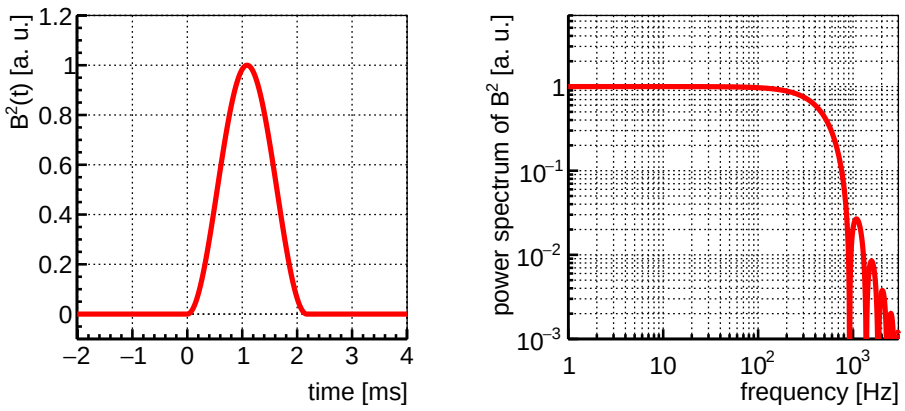

Figure 2.5: Example of square of the magnetic field with pulsed magnet. Assumed parameter is $C = 6$ mF and $L = 80$ μH. Left: Signal shape in time domain. Right: Signal spectrum in frequency domain.

2.7 Candidates of background

In Section. 2.5, the intrinsic noise of the optical system is discussed. In addition to that, the candidates of background induced by the magnetic field is also exist. As they occurred at the same time with the magnetic field, they could be fake VMB signals. These background sources give other requirements to the design of the experimental setup.

2.7.1 Cotton-Mouton effect of residual gas

It is known that under magnetic field, gases become birefringence materials. This is called Cotton-Mouton effect [45]. The birefringence induced by Cotton-Mouton effect of gas under magnetic field B is expressed as follows,

$$\Delta n_{\mathrm{CM}}^{\mathrm{gas}} = k_{\mathrm{CM}}^{\mathrm{gas}} B^2 \times P. \tag{2.32}$$

where P [Pa] is the partial pressure of the gas and $k_{\mathrm{CM}}^{\mathrm{gas}}$ [$\mathrm{T}^{-2}\mathrm{Pa}^{-1}$] is the coefficient of Cotton-Mouton effect. As this effect has the same magnetic dependence with VMB, it is difficult to distinguish Cotton-Mouton effect of gas from VMB. Therefore, the pressure around the magnetic field region is important to suppress these effects low enough.

In Table 2.1, $k_{\mathrm{CM}}^{\mathrm{gas}}$ of each gas and required partial pressures to suppress its Cotton-Mouton effect measured by 1064 nm laser is shown [36, 46–48]. Cotton-Mouton effect is used for calibration of the apparatus for every VMB experiment [36, 48–50].

Table 2.1: Coefficient of Cotton-Mouton effect of each gas and partial pressure where $\Delta n_{\rm gas} = \Delta n_{\rm vac}$

name of gas	k_{CM}^{gas} [$\mathrm{T}^{-2}Pa^{-1}$]	partial pressure where $\Delta n_{\rm gas} = \Delta n_{\rm vac}$
N_2	-2.0×10^{-18} [46]	1.6×10^{-6}
O_2	1.8×10^{-17} [46]	1.6×10^{-7}
H_2O	6.7×10^{-20} [47]	6.7×10^{-5}
He	2.1×10^{-21} [48]	1.9×10^{-3}
Ar	7.0×10^{-20} [36]	5.7×10^{-5}

2.7.2 Cotton-Mouton effect of mirrors

It is known the mirror itself shows Cotton-Mouton effect and its value is 10^{-9} rad [51]. To suppress the Cotton-Mouton effect of the mirrors, the magnetic field at the mirror should be small enough. This gives the requirement of the of leakage field at the mirror should satisfies the following relation,

$$B(\text{mirror}) < \sqrt{\frac{B^2 \times L_B}{10^8}}, \tag{2.33}$$

where L_B is the length of the magnetic field.

2.7.3 Faraday effect of the residual gas and mirrors

It is known that the longitudinal magnetic field also interacts with gases or mirrors, and it results the rotation of the polarization of the incident light. This effect is called Faraday rotation. The induced rotation can be expressed in the case of gases as

$$\Theta = k_{\rm F}^{\rm gas} B_{\parallel} \times P. \tag{2.34}$$

where $k_{\rm F}^{\rm gas}$ $\mathrm{T}^{-1}\mathrm{Pa}^{-1}$ is called the Verdet constant. It is known that the mirrors of a Fabry-Pérot cavity also shows the faraday rotation. As Faraday rotation is proportional to the longitudinal magnetic field, by applying magnetic field of opposite signs, its effect can be canceled. Because the square term of the faraday rotation has the same magnetic field dependence, it is difficult to distinguish its effect from VMB. Therefore, sufficiently small longitudinal magnetic field and low pressure is required.

2.8 Target specification

From the previous discussions, the target specification of this experiment is calculated. The first physics target of this experiment is the observation of the VMB induced by QED, thus the target specification is designed to observe the effect of

QED with reasonable data acquisition time. The design specification of the optical system is summarized in Table 2.2. The target specification of the magnet system is summarized in Table 2.3. Fig. 2.6 shows the design sensitivity of optical pass length difference. The power spectrum of the signal shape is superimposed with arbitrary unit for comparison. The frequency response of each noise source is discussed in Appendix B. From these spectrums, the sensitivity of VMB per one pulse can be calculated. The target sensitivity is

$$\Delta k_{\mathrm{CM}} = 1.3 \times 10^{-21} [\mathrm{T}^{-2}/\mathrm{pulse}]. \tag{2.35}$$

Assuming repetition rate of 0.05 Hz, the sensitivity reaches QED prediction with 20 days' run.

Table 2.2: Summary of the design parameters of optical system. From these parameters, the noise budget is calculated.

parameter name	size [unit]
wavelength λ	1064 [nm]
finesse F	500,000
FWHM ν_{FWHM}	100 [Hz]
Output power I_t	10 [mW]
Static birefringence Γ	0.003
phase delay of the cavity α	2 [μrad]
Frequency noise ν	1 [mHz/$\sqrt{\mathrm{Hz}}$]
Relative Intensity noise RIN	10^{-6} [1/$\sqrt{\mathrm{Hz}}$]
detector noise Δi_{PD}	10 [fA/$\sqrt{\mathrm{Hz}}$]
efficiency of photo diode q	0.5

Table 2.3: Summary of the design parameters of magnet.

parameter name	size [unit]
Peak magnetic field	20 [T]
field length	1 [m]
pulse width	2 [msec]
repetition rate	0.05 [Hz]

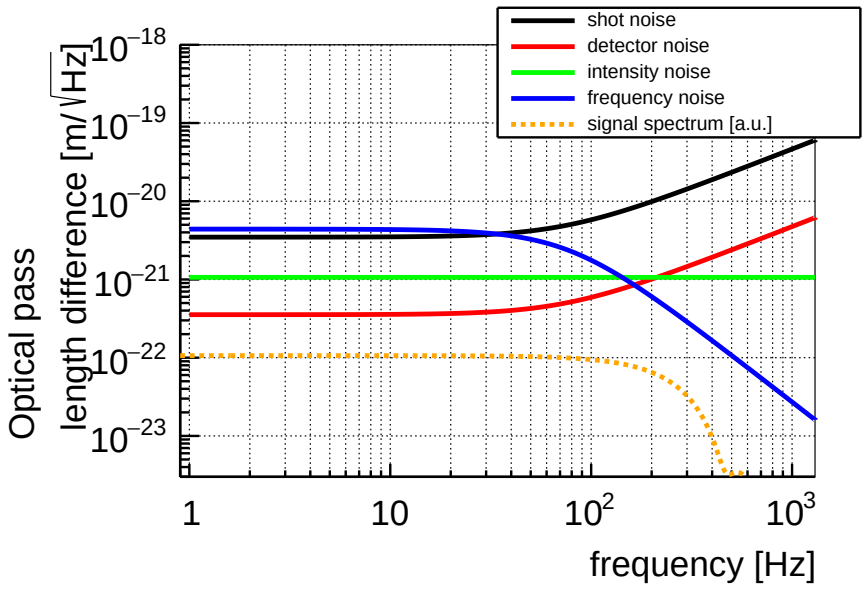

Figure 2.6: Power spectrum density of the designed sensitivity. The parameters are summarized in Table 2.2. The signal spectrum is drawn for comparison.

Chapter 3

Experimental setup

The development of the optical system, the magnet and the establishment of the stable operation of the magnet with the optical system are the key technologies of this experiment. This section describes the detail of the developed experimental setup.
First, the optical system including the Fabry-Pérot cavity and the polarizers are described. The intrinsic noise level of the optical system is evaluated. After that the specification of the pulsed magnet and the detail of the magnet operation system are shown. The rest of this chapter explains the other component of the experimental setup.

3.1 Overview

Figure 3.1 shows a schematic view of the experimental setup. On the 1.2 m× 2.4 m optical bench, optical system including a Fabry-Pérot cavity and polarizers are installed. The optical bench is placed inside the clean room which is surrounded by shading sheets for the safety operation of the laser and to eliminate the stray light from outside of the optical bench. The pulsed magnet is installed on the magnet bench. The magnet is connected to the charging unit outside the laser clean booth via coaxial cable. Figure 3.2 shows a picture of the experimental room.

3.2 Optical system

3.2.1 Overview of optical system

Figure 3.3 and Fig. 3.4 show the overall setup of optical system. A Non-Planar Ring Oscillator laser which is called Mephisto is used as a master laser. An AOM is used for intensity stabilization for input laser. An EOM is used to generate side-bands to lock the frequency of the laser to the resonance frequency of the cavity. A polarizar is placed just before the input mirror to align the polarization of the input laser.

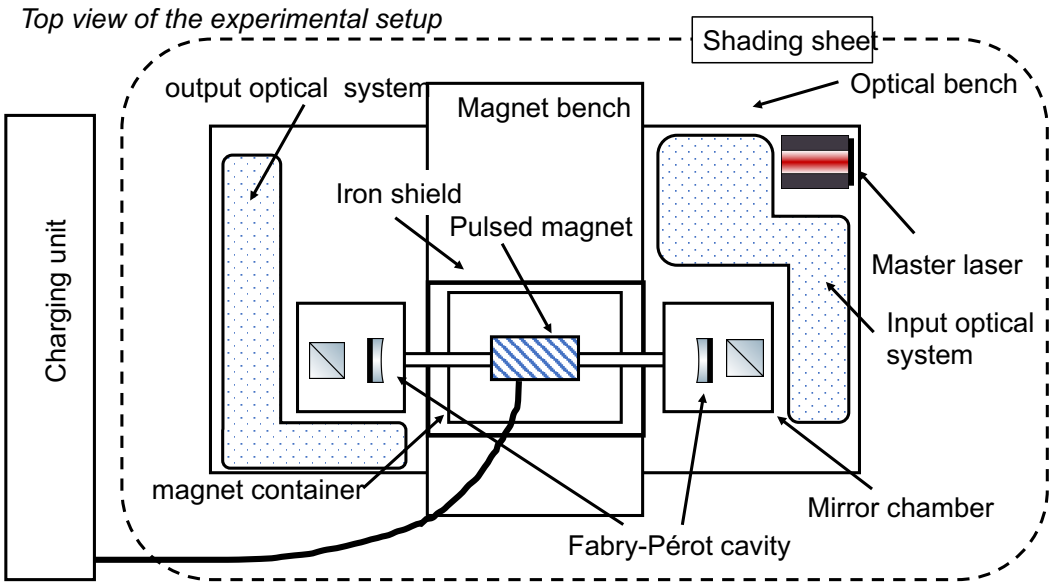

Figure 3.1: Schematic view of the experimental setup. On the 1.2 m× 2.4 m optical bench, optical system is installed. A Pulsed magnet are installed on the magnet bench. The magnet is connected to the charging unit via coaxial cable outside the laser booth.

Total 4 photodiodes are used in this setup. PD_{in} is used to monitor the intensity of the input laser. PD_r is used to monitor the intensity of the reflected beam by M1. This information is used to lock the laser with PDH method. PD_t is used to monitor the ordinary beam transmitted through the analyser. PD_e is used to monitor the extraordinary beam after the analyser which signal could appears.

The mirrors of the Fabry-Pérot cavity and the polarizer and the analyzer is placed inside the vacuum chamber to avoid the polarization change by the air and to decrease the absorption by the air. Figure 3.5 show the picture of the input optics.

3.2.2 Master laser

The finesse of a Fabry-Pérot cavity depends on the reflectivity of the mirrors. The highest reflectivity is established at 1064 nm among the manufactured mirrors. In this work, Nd:YAG laser Mephisto is used as a master laser. The wavelength of the Mephisto is 1064 nm. The maximum output power is 500 mW. Mephsito has 2 port to tune its wavelength. They are used as the actuator of PDH method. One is the PZT actuator to tune the cavity length of the cavity inside Mephisto. Its bandwidth is $\sim$ 50 kHz and its tuning range is $\sim$ 200 MHz. The other is the temperature controller of the crystal in the Mephisto. Its tuning bandwidth is $\sim$ 1 Hz and its tuning range is $\sim$ 1 GHz.

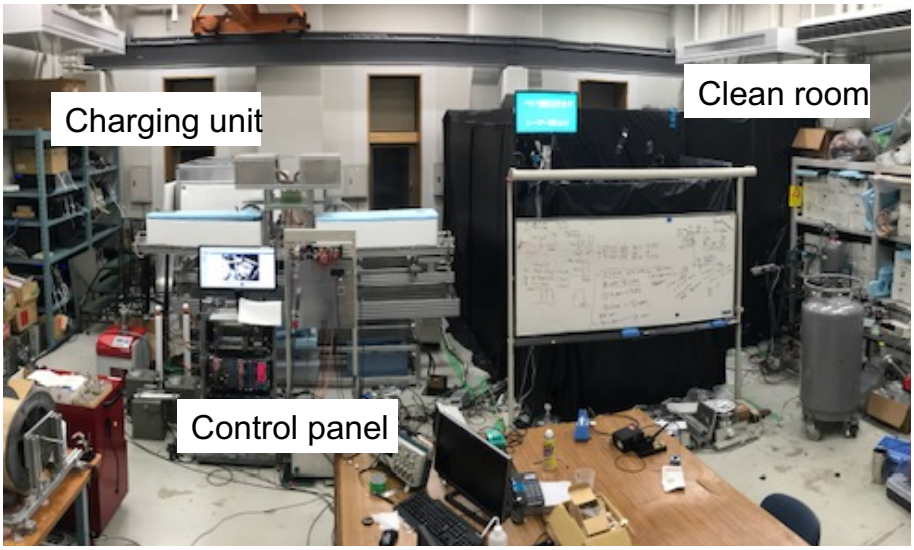

Figure 3.2: Picture of the experimental room. A clean room where laser and the magnet are operated, a charging unit of the magnet and control panel of the magnet and a data acquisition system are placed.

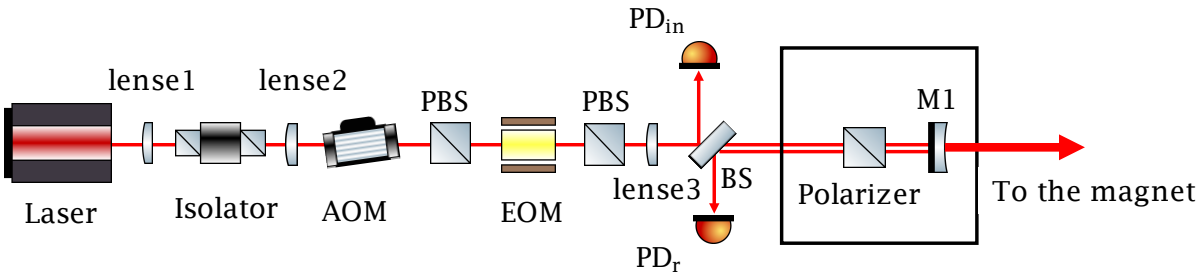

Figure 3.3: Schematic view of the input optics.

3.2.3 Fabry-Pérot cavity

We use super mirrors manufactured by Advanced Thin Film company. The designed reflectivity R is $R > 99.999\%$ and the radius curvature is 2 m. The cavity length is 1.4 m. Figure 3.8 show the picture of the mirror mount. The mirrors are aligned by 3 axes, pitch, yaw and rotation. The first 2 degrees of the freedom are used for the spatial alignment of the cavity, and the last one is used to align the fast (or slow) axis of the mirror to the input polarization angle. All axes can be controlled from outside the vacuum chamber by the pico-motor.

The finesse is evaluated by a cavity ring down method. The output power from the Fabry-Pérot cavity obeys an exponential decay after turning off the input laser. The finesse F is related to the lifetime of the decay τ as $F = \frac{\tau\pi c}{L}$. Fig. 3.7 shows

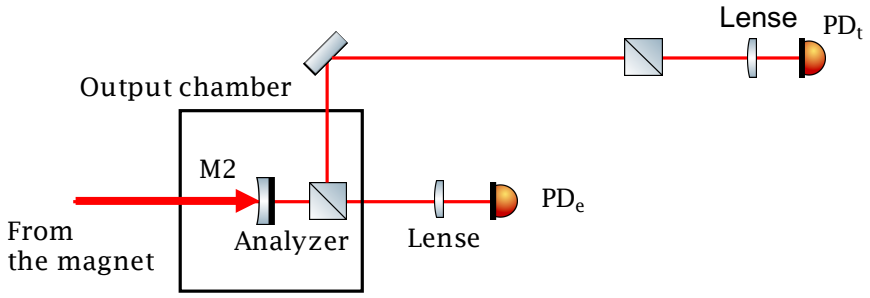

Figure 3.4: Schematic view of the output optics.

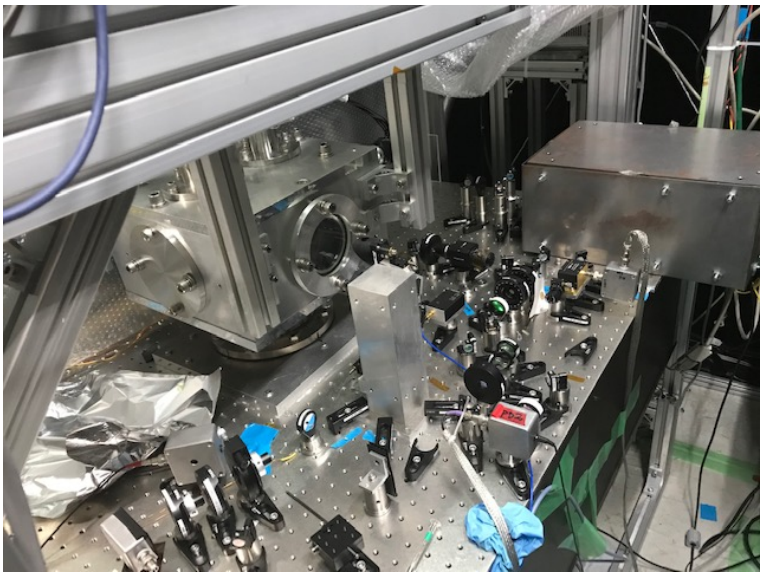

Figure 3.5: Picture of the input optics.

an example of a cavity ring down measurement result. The measured finesse is 490,000 which is consistent with the expected finesse calculated from the designed reflectivity of mirror.

3.2.4 Frequency feedback system

As a high finesse cavity has a severe resonance condition, it is necessary to lock the frequency of the laser to the resonance frequency of the cavity. Pound-Drever-Hall (PDH) method is used [52] to extract an error signal between them. The theoretical background about PDH method is described in Appendix A.

The schematics of the frequency feedback system is described in Fig. 3.9. An EOM is driven with 4.5 MHz RF signal to generate sidebands. The reflected light is detected by fast photo detector (PD2) and demodulated by 4.5 MHz RF to extract error signal. The error signal is sent to the PZT actuator and temperature

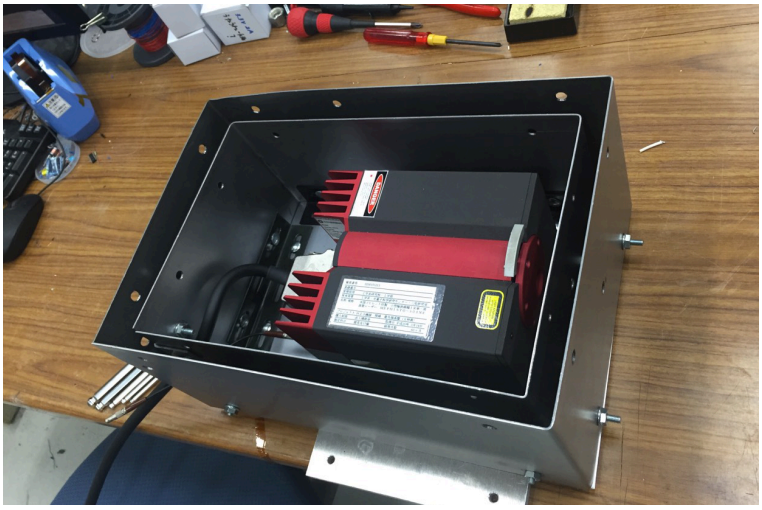

Figure 3.6: Picture of Mephisto.

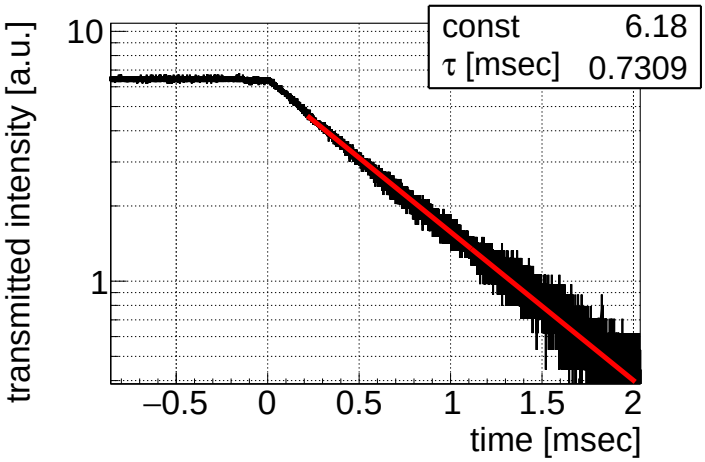

Figure 3.7: Measurement of the finesse.

controller of the Mephisto after the servo circuits and drivers.

Fig. 3.10 shows the residual frequency noise spectrum evaluated from the in-loop error signal and gain of PDH method. The rough requirement of frequency noise is also shown in red line assuming $F = 500,000$, $I_0 = 3$ mW, and the phase retardation per each round trip is 2 μrad. The transfer function to calculate the requirement is shown in Appendix. B. Above 50 Hz, the estimated frequency noise is below the requirement.

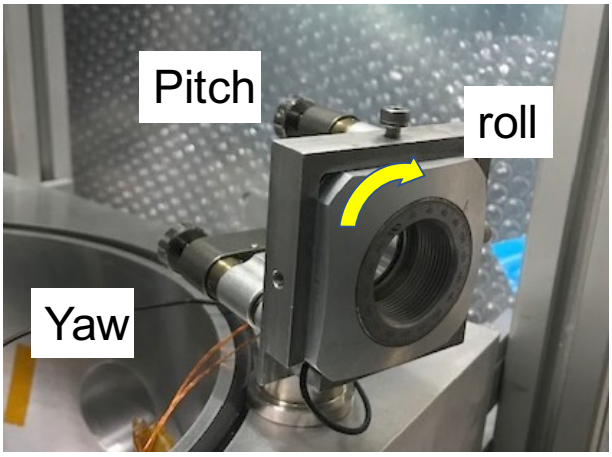

Figure 3.8: Picture of the mirror mount. Pitch, yaw and rotation angle can be controlled via pico-motor.

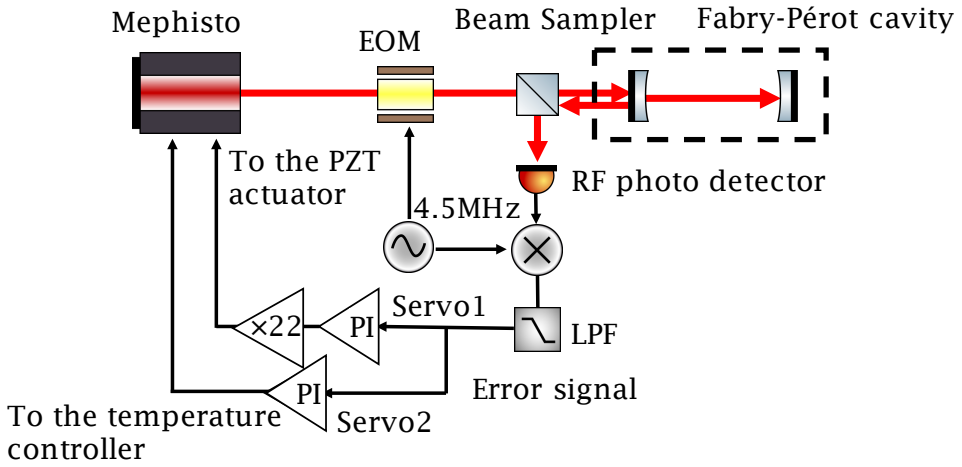

Figure 3.9: Schematic view of the frequency feedback system for a Fabry-Pérot cavity.

3.2.5 Auto locking system

Due to the unexpected large disturbance to the cavity or long term-drift of the cavity length, the cavity sometimes loses its resonance. As the PDH signal is nonzero only near the resonance frequency, the laser frequency should be tuned to near the resonance frequency manually to lock the laser to the cavity again. For the seamless data acquisition, this locking procedure is automatized. The auto-locking procedure is divided to 3 steps as follows.

Scanning phase

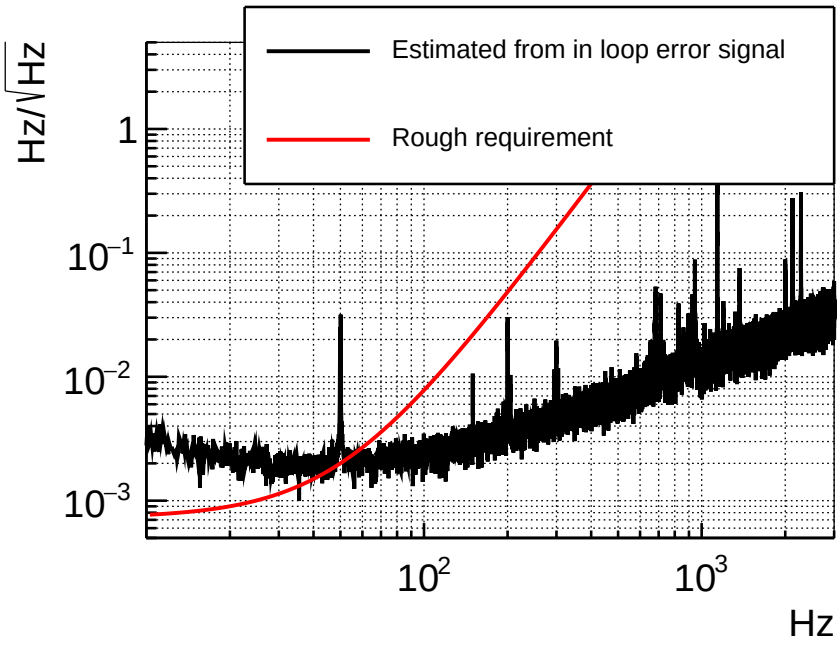

Figure 3.10: Spectrum of the residual frequency noise estimated from in loop error signal.

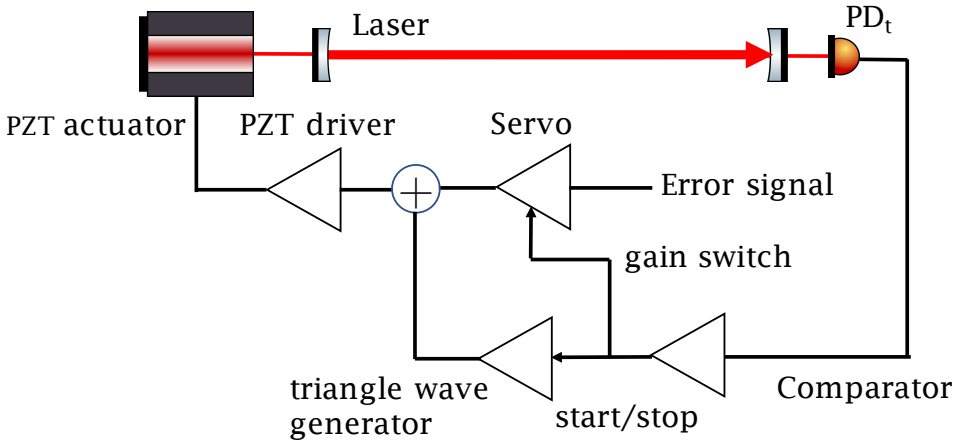

Figure 3.11: A schematic view of an auto locking system.

When the cavity loses its lock, a triangle wave generator is switched on. It can modulate the input laser frequency more than 1 FSR to find the resonance frequency. During this phase, the temperature feedback is turned off. The period of the triangle wave is about 1 s.

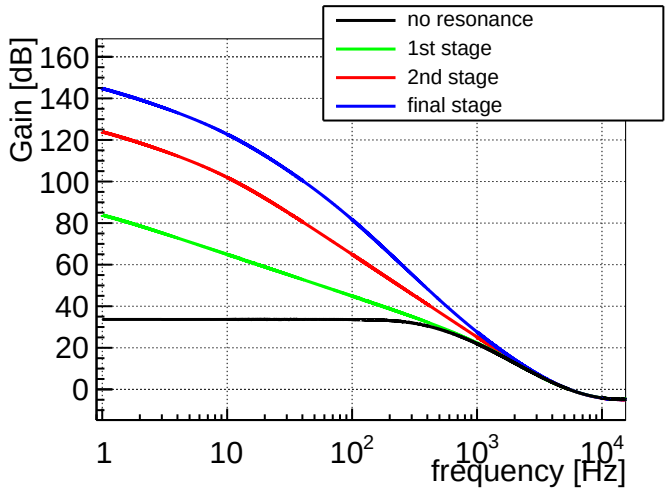

Figure 3.12: Designed gain of the locking circuit at different locking state.

Locking phase

when the frequency of the input laser comes closes to the resonance frequency, some part of the input light transmits the cavity and monitored by PD_t. When the output of the PD_t exceeds threshold predefined in the comparator circuit, a TTL signal is send to the triangle wave generator to stop the modulation. Frequency of the laser is fixed to near the resonance frequency. This helps the initial locking of Fabry-Pérot cavity to start.

Gain boost phase

After the cavity is locked, the gain of the servo circuit is increased step by step to suppress the frequency noise further. Fig. 3.12 shows the designed gain of the servo circuit. When the cavity is not locked, the gain of the circuit is black line in Fig. 3.12. After the locking, the gain is increased from the 1st stage to final stage in Fig. 3.12. After the gain of the feedback circuit reaches final stage, the feedback to the temperature controller switches on.

3.2.6 Polarizer and Analyser

The gran laser prisms (GLPB2-10-25.9SN-7/30) are used as a polarizer and an analyzer. The extinction ratio is 3×10^{-7}, which is small enough for this experiment.

3.2.7 Mirror chambers

Figure 3.13 and 3.14 show the pictures of the input mirror chamber and the output mirror chamber. To avoid the loss due to the air, the mirrors of a Fabry-Pérot cavity

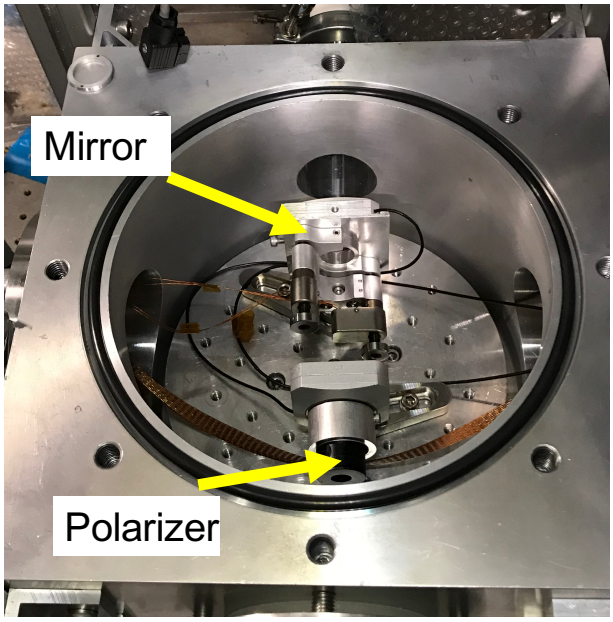

Figure 3.13: Picture inside the input chamber. One high reflective mirror and the polarizer is placed. The rotation angle and the alignment of the mirror and the rotation angle of the polarizer can be controlled by the pico-motor from outside of the chamber

is placed inside the chamber. The polarizers are also placed inside the chambers to avoid the polarization change due to the air. Each chamber has two windows whose transmittance is 90%.

The chambers are connected only with flexible bellows to the optical bench and the pulsed magnet and supported by another suspension frame to avoid the propagation of the mechanical disturbances caused by the pulsed magnet to the optical bench through the mirror chambers.

3.2.8 Signal detector

The power of the extraordinary light is monitored by PD_e. S11499-01 (HAMAMATSU) is used as a photodiode. To detect the small DC power of extraordinary light, the gain of signal detector is designed to 6×10^7 V/W. To suppress the stray light from other component, an iris and a band-pass filter are also placed before the detector. The whole detector is covered with iron shield to suppress the noise induced by the electromagnetic induction when the pulse field is applied. The picture of the signal detector is shown in Fig. 3.15. The specification of the signal detector is summarized in Table 3.1.

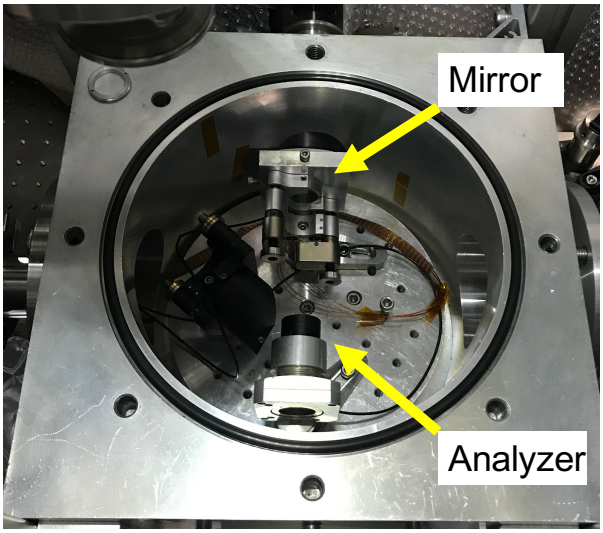

Figure 3.14: Picture inside the output chamber. One high reflective mirror and the analyzer is placed. The output light from each 2 ports of the analyzer is led to the photo-detectors.

Table 3.1: Specification of the signal photo detector

parameter	specification
wavelength	$300 \sim 1100$ [nm]
efficiency	0.6 [A/V]
Gain	1×10^8 [V/A]
bandwidth	3 [kHz]
sensor area	5 [mm^2]

3.2.9 Input intensity stabilization

The input power is stabilized with an AOM to suppress the effect of the intensity noise inside the cavity. The requirement for the intensity stability can be roughly estimated assuming that the output intensity from the Fabry-Pérot cavity is 15 mW, the static birefringence is 1×10^{-5} and its frequency response.

The red line in Fig. 3.16 shows the achieved intensity noise after the stabilization of the input laser evaluated out of loop. The blue line in Fig. 3.16 is the calculated requirement. Above 50 Hz, the intensity noise is smaller than the requirement except for some peaks.

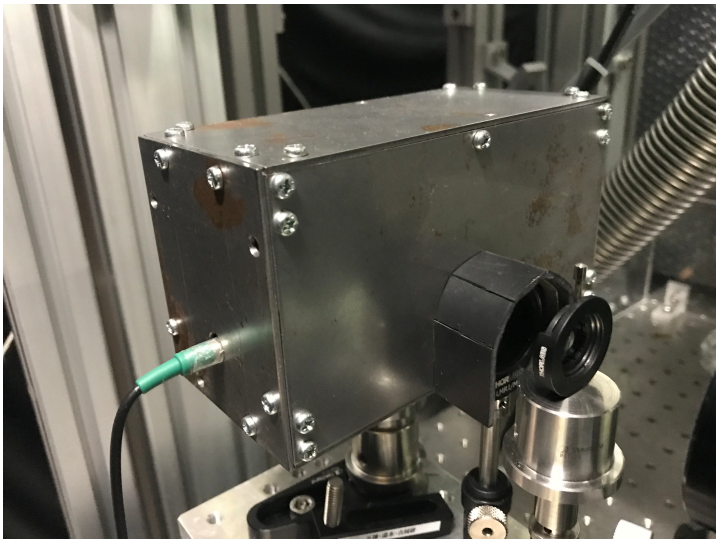

Figure 3.15: Picture of the signal photo detector.

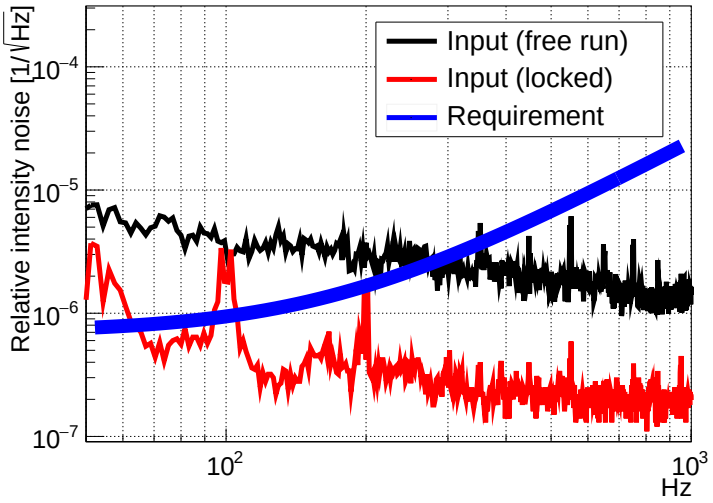

Figure 3.16: Result of the evaluation of input intensity stabilization. The black line is the relative intensity noise of input laser during free run. The red line is relative intensity noise during intensity locking is activated. The blue line is an estimated requirement of noise level.

3.3 Evaluation of the sensitivity to the optical pass length difference

In this section, the sensitivity of the optical pass length difference without the magnet is evaluated. The study of the birefringence noise has been mainly performed

at low frequency up to 25 Hz which is important for the VMB search with the permanent magnet. In contrast, the frequency region which is important for the VMB search with pulsed magnet is around 100 $\sim$ 1 kHz. Only limited study has been reported about the study of the birefringence noise at this frequency region [42]. In this chapter, the systematic investigation of the evaluation of the birefringence noise in wide frequency region is reported. The noise evaluation method in the homodyne detection system has been established taking into the account the phase retardation of the mirrors.

This sensitivity determines the ideal sensitivity of this experiment, and it is useful to compare this sensitivity with the sensitivity during the magnet operation to discuss the noise induced by the magnet.

3.3.1 Measurement of the phase retardation of the mirror

As discussed in Appendix B, the transmittance of the extraordinary light is attenuated by $\kappa^2(\alpha) \equiv \frac{1}{1+(\frac{2F}{\pi})^2\times(\frac{\alpha}{2})^2}$ due to the birefringence of the mirror where α [rad] is the phase delay of the mirror per round trip. To measure α, α dependence of the transfer function of the extraordinary light against the input power modulation is used. As discussed in Appendix B, the transfer function from the input power modulation to the extraordinary light can be written as follows,

$$\Delta I_e = T_{\mathrm{FP}} \times I_0(f), \tag{3.1}$$

where T_{FP} is defined as follows,

$$\begin{aligned} T_{\mathrm{FP}}(f) = &\frac{\Gamma^2}{2(1+i\frac{F}{\pi}\alpha_{\mathrm{eq}})(1-i\frac{F}{\pi}\alpha_{\mathrm{eq}}-i\frac{f}{f_c})(1-i\frac{f}{f_c})} \\ &+ \frac{\Gamma^2}{2(1-i\frac{F}{\pi}\alpha_{\mathrm{eq}})(1+i\frac{F}{\pi}\alpha_{\mathrm{eq}}-i\frac{f}{f_c})(1-i\frac{f}{f_c})}, \end{aligned} \tag{3.2}$$

where F is the finesse of the Fabry-Pérot cavity and f_c is the cutoff frequency of the Fabry-Pérot cavity.

AOM is used to modulate the input power and its modulation is evaluated by PD_0. The modulated intensity of the extraordinary light is evaluated by PD_e. The frequency response analyzer is used to calculate the transfer function from the measured voltage of the PD_0 to PD_e.

$$T^V_{\mathrm{FP}} = V_e(f)/V_0(f) \propto T_{\mathrm{FP}}(f) \equiv p0 \times T_{\mathrm{FP}}(f). \tag{3.3}$$

Figure 3.17 shows the measured gain spectrum of T^V_{FP}. The measured curve is fitted by $T^V_{\mathrm{FP}}(f)$. From the fitting result, the phase retardation per each round trip is obtained as

$$\alpha_{\mathrm{eq}} = 1.5 \pm 0.1[\mu\mathrm{rad}]. \tag{3.4}$$

The evaluation of the sensitivity is performed with this alignment.

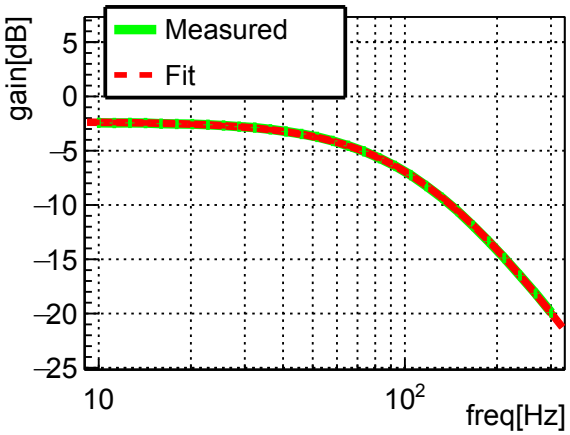

Figure 3.17: Gain curve of the transfer function from the input power modulation to the extraordinary power modulation. The measured curve with fitted by T_{FP}^{V}. From the fitting, the phase retardation of the Fabry-Pérot cavity is obtained

To confirm that the measured value depends on the relative angle of the mirror as discussed in Appendix B, the same measurement is performed after rotating the azimuth angle of the input mirror ~ 90 degree. The result is shown in Fig. 3.18. In this case the alpha is measured to be

$$\alpha_{\mathrm{eq}} = 5.5 \pm 0.1 \ [\mu\mathrm{rad}]. \tag{3.5}$$

Small α is preferred to enhance the signal and the suppress the contribution of frequency noise, thus the sensitivity evaluation during this chapter is performed by re-rotating the mirror angle. These measured α are consistent with the previous experiment [53].

3.3.2 Sensitivity measurement

Fig. 3.20 shows the measured sensitivity spectrum of the optical pass length difference. The spectrum is the average of 20 sets of the measurement. For each measurement, waveform of I_e and I_t is acquired. All data are acquired by ADC (PCI-6229, National Instrument). The measurement time is 10 sec and the sampling rate is 10 kHz. The interval of each time series is 2 second. Figure 3.19 shows the example of the measured voltage signal of the I_{e} and I_{t}. The optical pass length difference is calculated as follows,

$$\begin{aligned} \Delta L(f) &= \frac{\lambda}{2F}\frac{1}{2\kappa^2(\alpha)\Gamma}\frac{I_e}{I_t}(f) \\ &= \frac{\lambda}{2F}\frac{1}{2\kappa(\alpha)\Gamma'}\frac{I_e}{I_t}(f) \end{aligned} \tag{3.6}$$

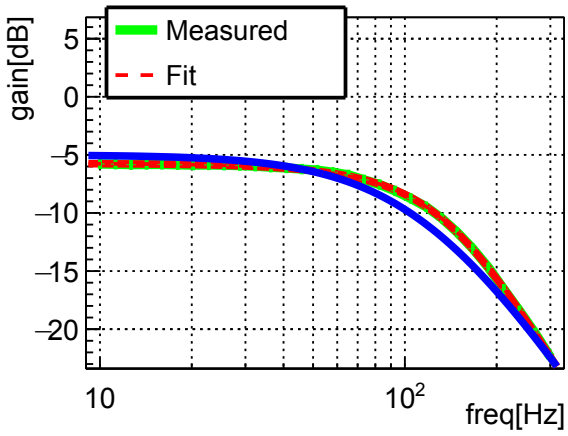

Figure 3.18: Gain curve of the transfer function from the input power modulation to the extraordinary power modulation after rotating the mirror. The measured curve is slightly difference from the previous measurement. This is because the transfer function should dependes on the relative angle of the 2 mirrors. For comparison, the transfer function assuming no phase retardation is also shown in blue line.

where Γ' is the static birefringence of mirrors after the attenuation, which can be calculated as

$$\Gamma' \equiv \left(\sqrt{\frac{I_e}{I_t}} \right)_{\mathrm{DC}} \tag{3.7}$$

and $\kappa(\alpha)$ is the attenuation factor discussed above. From the power spectrum of the optical pass length difference without magnetic field, the ideal sensitivity of the optical system is obtained. The possible noise source of the measured sensitivity is discussed later.

3.3.3 Evaluation of known noise source

In this section, the expected birefringence noise level is estimated from all the known noise source. The considered noise source are

- intensity noise
- frequency noise
- shot noise
- detection noise
- noise independent of the Fabry-Pérot cavity
- magnetic field noise

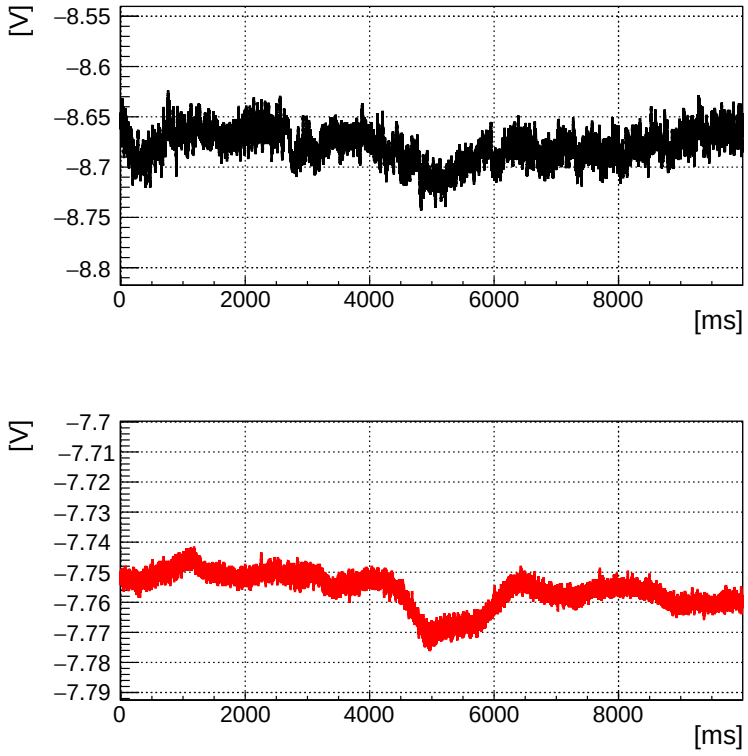

Figure 3.19: Time series of I_e (upper) and I_t (lower). The measurement time is 10 sec and the sampling rate is 10 kHz.

Among them, the frequency noise possibly has 3 difference origin. They are

- frequency noise due to the residual frequency noise of the PDH feedback system.
- frequency noise due to the detection noise of the PDH method
- frequency noise due to fluctuation of the phase retardation of the mirror

Finally, the contribution of total 8 types of the noises is evaluated. Figure 3.21 shows the power spectrum of the noise budget. The detail of the noise sources and their estimation methods are discussed below.

Intensity noise

The fluctuation of the internal power of a Fabry-Pérot cavity could become the noise source. Its contribution is

$$\Delta L(f) = \frac{\lambda}{2F} \times \frac{\Gamma'}{2\kappa} \frac{G_p I_t(f)}{(I_e)_{\mathrm{DC}}}, \tag{3.8}$$

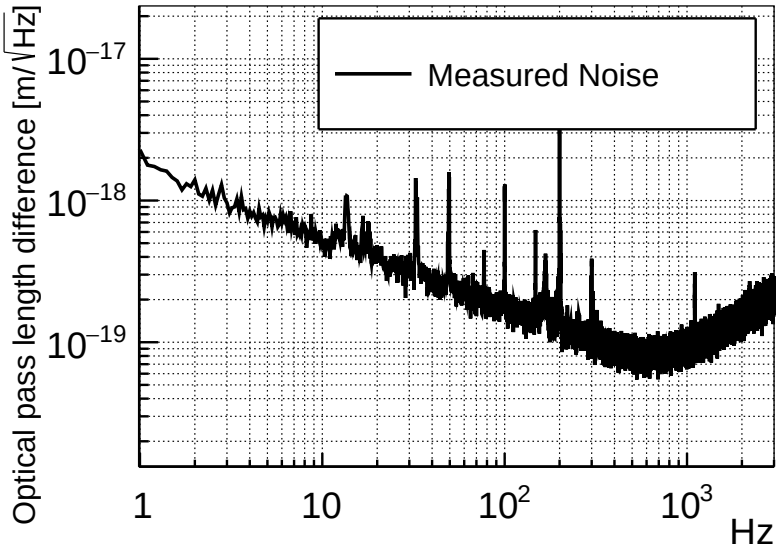

Figure 3.20: Power spectrum of the measured birefringence noise in the unit of optical pass length difference.

where G_p is a transfer function from I_t to I_e. The theoretical expression of G_p is derived in Appendix.B.2, whose behavior is similar to the first order low pass filter whose cutoff frequency is the cavity pole. G_p can be written as follows,

$$G_p = T_{\mathrm{FP}}/T_0, \tag{3.9}$$

where T_{FP} is a transfer function from I_0 to I_{e}, which is used in Chapter. 3.3.1. T_0 is a transfer function from I_0 to I_t, and can be obtained by the measurement of the frequency response by modulating the input intensity by AOM. The intensity noise of the internal power is evaluated by the $\mathrm{PD_t}$. Its contribution is shown with orange line in Figure 3.21.

Frequency noise

The contribution of the frequency noise to the optical pass length sensitivity can be calculated from the following equation.

$$\Delta L(f)^{\mathrm{freq}} = \frac{\lambda}{2F} \times \frac{1}{2\kappa\Gamma' I_t} \times G_1 \times \Delta\nu_{\mathrm{noise}}(f), \tag{3.10}$$

where $\Delta\nu_{\mathrm{noise}}$ is the spectrum of frequency noise and G_1 is the transfer function from frequency noise to the intensity noise of I_e.

Fig. 3.22 shows the block diagram of feedback system. From this diagram,

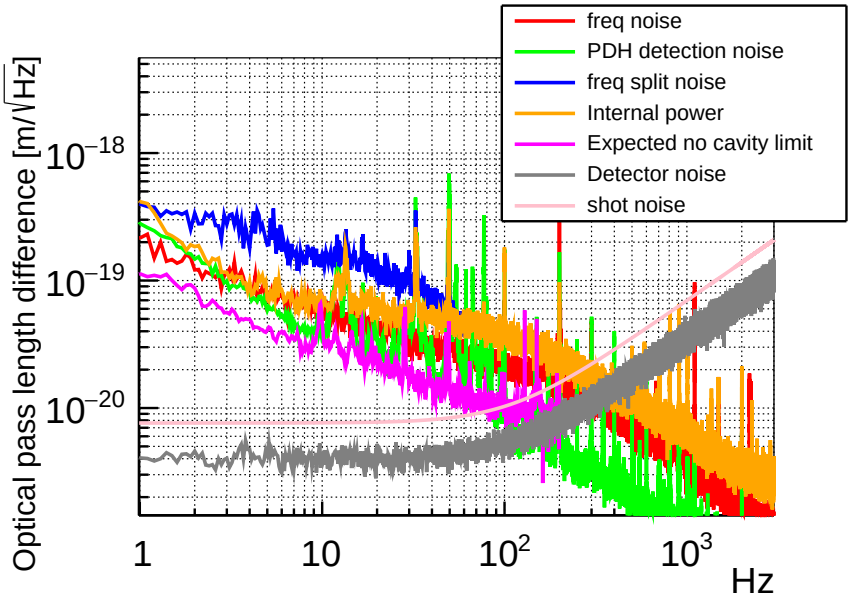

Figure 3.21: Power spectrum of the possible contribution of the all known noise source.

the frequency noise can be written as

$$\Delta\nu_{\rm noise} = V_{\rm err}/G_{\rm PDH}, \tag{3.11}$$

where $G_{\rm PDH}$ is the gain of PDH method and $V_{\rm err}$ is the spectrum of the error signal. From these equations, $\Delta L(f)^{\rm freq}$ can be written as

$$\Delta L(f)^{\rm freq} = \frac{\lambda}{2F} \times \frac{1}{2\kappa\Gamma' I_t} \times \frac{G_1}{G_{\rm PDH}} \times V_{\rm err}(f) \tag{3.12}$$

From the box diagram, it is also shown the transfer function from the external input port ($V_{\rm ex}$) to intensity noise of I_e is also $\frac{G_1}{G_{\rm PDH}}$. This transfer function is measured by using frequency response analyser. Fig. 3.23 shows the measured transfer function from $V_{\rm ex}$ to the voltage signal of PD_e. From this measurement and the spectrum of the error signal, the contribution of the frequency noise to the optical pass difference noise can be calculated. The result is shown by a red line in Fig. 3.21.

Frequency noise due to the PDH detection noise

Since the detection noises of PDH method is also feedbacked to the laser frequency, it also generates the frequency noise. The general origin of detection noises are known as the residual amplitude modulation (RAM) of EOM, shot noise of the reflected light, and electrical noise of the detector of the reflected

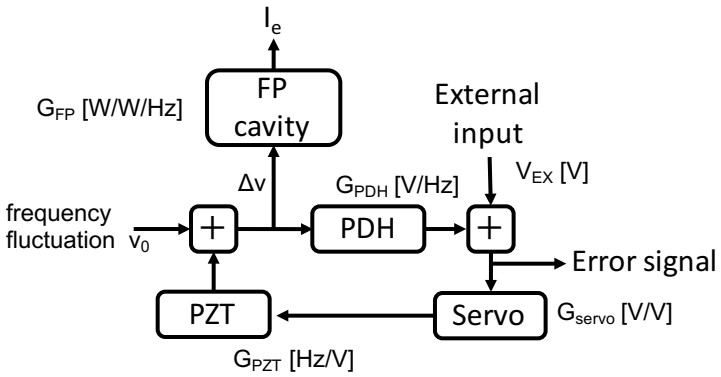

Figure 3.22: Block diagram of feedback system.

light. The transfer function of the detection noise to the intensity noise of the extraordinary light is also G_{freq}. The detection noise of the PDH method is evaluated from the error signal of PDH signal when the input laser frequency is far from the resonance frequency. The contribution of the PDH detection noise is shown in green line in Fig. 3.21.

Frequency noise due to the phase retardation of the mirrors

The frequency noise discussed above is that against the resonance frequency of the ordinary light. There is another possibility of the frequency fluctuation. It is the fluctuation of the phase retardation of the mirrors ($\Delta\alpha$). Below the cut off frequency, the contribution of $\Delta\alpha$ to the optical pass length difference

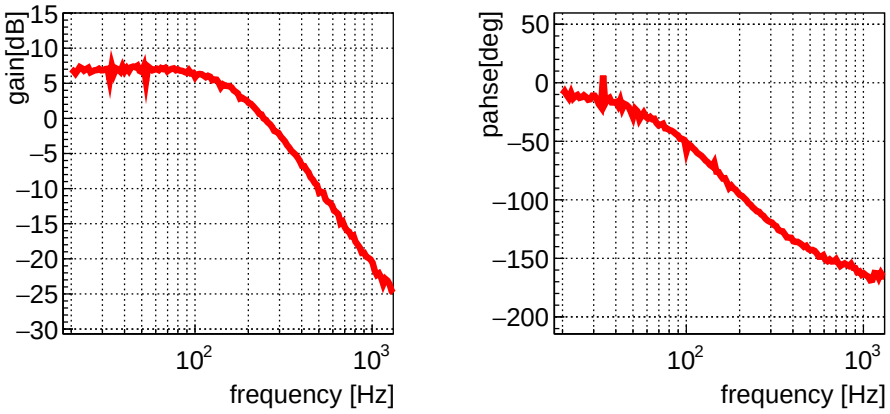

Figure 3.23: Example of the measured transfer function from V_{ext} [V] to V_e [V]. This function is used to estimate the contribution of frequency noise to the optical pass length noise spectrum.

can be written as

$$\Delta L(f)^{\alpha} = \frac{\lambda}{2F} \times \frac{\Gamma'}{\kappa} \times \left(\frac{F}{\pi}\right)^2 \times \alpha \times \Delta\alpha(f). \tag{3.13}$$

Though it is difficult to measure the fluctuation of the α directly, its upper effect is estimated as follows.

To evaluate the stability of α, the property that the transfer function $\frac{G_1}{G_{\mathrm{PDH}}}$ is proportional to α is used. The stability of α appears at the stability of the gain of $\frac{G_1}{G_{\mathrm{PDH}}}$.

When the input laser frequency is modulated at f Hz by injecting the voltage signal to the external input port of the feedback system, this modulation induces the intensity noise of the extraordinary light and it can be written as,

$$\Delta I_{\mathrm{e}}(t) \propto I_0 \times \alpha(t) \times \sin(2\pi f t). \tag{3.14}$$

By using a lock-in-amplifier, one can extract the voltage signal proportional to the amplitude of intensity fluctuation at frequency f, which becomes

$$V_{\mathrm{lockin}}(t) \propto I_0 \times \alpha(t). \tag{3.15}$$

When it is assumed that fluctuation of α is small compared to the mean value of α, $\Delta\alpha(t)$ can be estimated as follows,

$$\Delta\alpha(t) = V_{\mathrm{lockin}}(t) / \left(V_{\mathrm{lockin}}\right)_{\mathrm{DC}} \times \alpha_{\mathrm{DC}}, \tag{3.16}$$

where $\left(V_{\mathrm{lockin}}\right)_{\mathrm{DC}}$ and α_{DC} are the mean values of output voltage of lock-in-amplifier, and α measured in Section 3.3.1.

Figure 3.24 shows the spectrum of estimated $\Delta\alpha$. The laser frequency is modulated at 550 [Hz] by the internal oscillator of the lock-in-amplifier. The output voltage of $\mathrm{PD_e}$ is sent to the lock-in-amplifier. The black line is detection limit. It can be seen that above 50 Hz, the spectrum is limited by the detection noise. This spectrum is used as the upper limit of the fluctuation of α.

The possible contribution of the frequency noise against the resonance frequency of the extraordinary light is shown in blue line in Fig. 3.21 below 50 Hz.

Shot noise

From the DC power at the detector, the contribution of the shot noise is calculated theoretically by using Eq. (2.25). It is shown with pink line in Fig. 3.21.

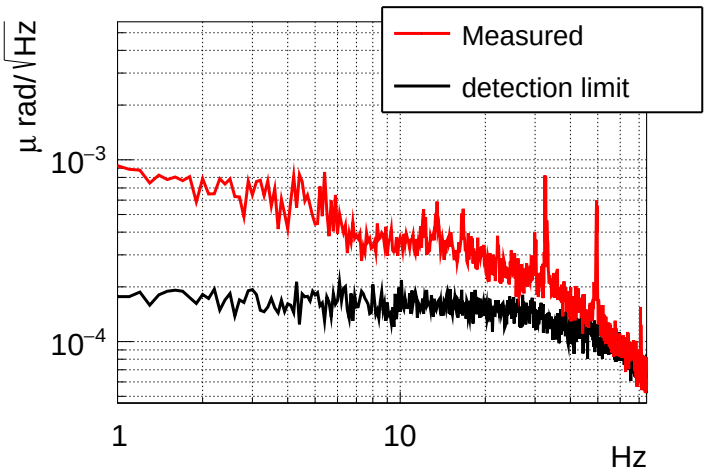

Figure 3.24: Power spectrum of the estimated α noise in the unit of radian. The black line is the detection limit when no modulation is applied.

Detector noise

The noise of the photodetector is also become the noise source of the optical pass difference. The noise of the detector is evaluated when no light is irradiated to the photodiode. Its contribution to the total noise is shown in gray line in Fig. 3.21.

Intrinsic noise without the Fabry-Pérot cavity

There are some noise sources which could appear even without the Fabry-Pérot cavity. The candidates of the noise source could be

- The birefringence induced before the Fabry-Pérot cavity
- The instability of the gain of the photo detector.
- The scattering or the turbulence after the analyzer.

To study the contribution of these noise source, the evaluation of the sensitivity without the Fabry-Pérot cavity is performed. The setup is shown in Fig. 3.25. In this measurement, a quarter wave plate is used to generate the static birefringence instead of the Fabry-Pérot cavity. All the other set up is the same with the measurement with the Fabry-Pérot cavity. When the slow axis of the quarter wave plate is slightly tilted θ ($\theta \ll 1$) against the input polarization axis, the measured signal becomes as follows.

$$\frac{I_e}{I_t} \sim 2\theta^2 + 2\theta\Psi(t) \tag{3.17}$$

Although it is impossible to distinguish the rotation and the ellipticity, the sensitivity of the optical pass difference without a Fabry-Pérot cavity can be roughly estimated as

$$\Delta L_{\mathrm{nocav}} \sim \frac{\lambda}{2\pi}\frac{I_e}{I_t} \tag{3.18}$$

.

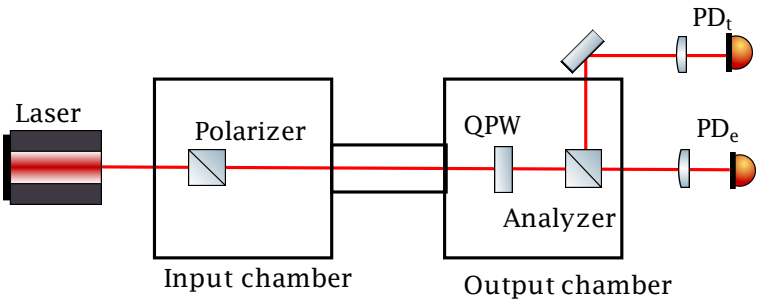

Figure 3.25: Schematic view of the set up for a birefringence measurement without a Fabry-Pérot cavity. Instead of the mirrors for a Fabry-Pérot cavity, a quarter wave plate is mounted in the output vacuum chamber. All other set up is the same with the measurement with a Fabry-Pérot cavity.

The result of the measurement is shown in the black line in Fig. 3.26. The known noise source is the shot noise and input power noise. The sum of the estimated noise is drawn with gray line in the same figure. Even without the Fabry-Pérot cavity, there are some discrepancy between the measured noise and the estimated noise especially below 100 Hz. When there are the Fabry-Pérot cavity, assuming these noises are generated outside the polarizers, they could appear $\frac{\pi}{2F}$ times smaller in the optical pass length sensitivity. With this assumption, the contribution of the noise without the Fabry-Pérot cavity can be estimated. The result is drawn with cyan line in Fig. 3.21 below 100 Hz.

Magnetic noise

Mirrors also show the Cotton-Mouton effect. Therefore, the fluctuation of the residual magnetic field at the center of the mirror could become the noise source. To estimate its contribution, the magnetic field at the center of the mirror mount is measured. The hole sensor is inserted to the mirror mount. Measured DC magnetic field is 1.6 [mT]. The measured spectrum density above 1 [Hz] is limited by the sensitivity of the hole sensor and it is less than 0.3 [$\mu\mathrm{T}/\sqrt{\mathrm{Hz}}$].

The coupling constant of the Cotton-Mouton effect of the mirror is measured to be $\sim 1 \times 10^{-9}$ [rad T^{-2}]. From these values, the expected polarization

noise induced by the fluctuation of residual magnetic field is

$$\begin{aligned}\Delta L &= 1 \times 10^{-9} \times \frac{\lambda}{\pi} \times B^2 \\ &\sim 1 \times 10^{-9} \times \frac{\lambda}{\pi} \times 2 \times B_{DC} \times B(f) \\ &< 3 \times 10^{-26}\ [\mathrm{m}/\sqrt{\mathrm{Hz}}].\end{aligned} \tag{3.19}$$

This is almost 7 order smaller than other noise source.

3.3.4 Mirror rotation dependence

As the static birefringence of the Fabry-Pérot cavity depends on the relative rotation angle between the two mirrors, the static birefringence can be tuned by rotating the mirrors. To identify the origin of the optical pass length difference noise, the noise spectra are measured at different rotational alignment of the mirror. Since the birefringence noise does not depend on the static birefringence of the mirrors, it can be distinguished from other types of noises by these measurements of the different mirror layouts.

Figure 3.27 shows the result of the measurement. The caption shows the static ellipticity at each alignment of the mirrors. The static ellipticity is chosen so as to be larger than the minimum value of the static ellipticity and smaller so that the contribution of known noise sources are not dominant. From Fig. 3.27, it can be seen that the noise floor of each measurement agrees with each other. It indicates that the observed noise is birefringence noise or at least its behavior can not be distinguished from the birefringence.

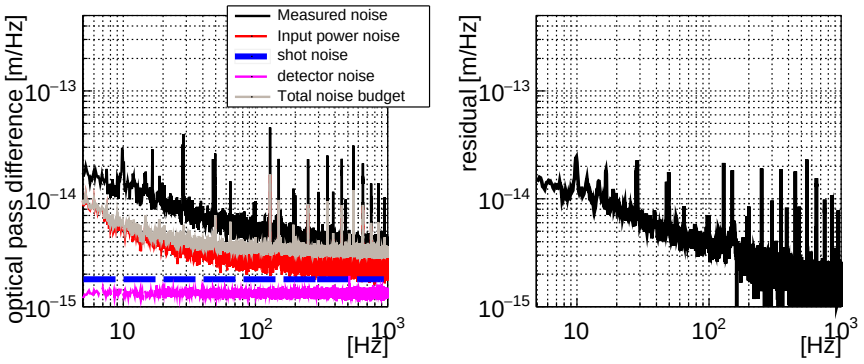

Figure 3.26: Left: noise spectrum of the optical pass difference without a Fabry-Pérot cavity. Black line: measured noise. Gray line: Estimated total noise budget from all known noise source. Right: The residual between measured noise and estimated noise budget.

3.3.5 Comparison of known noise source between the measured value and target specification

The noise budget of the target specification is discussed in Chapter 2.8. The comparison with the target specification and the measured noise of each known noise source is shown in Fig. 3.28 around 100 Hz to 1 kHz. The brown line is the sum of the known noise sources evaluated in the previous chapter. The blue line is the design sensitivity discussed in Chapter 2.8.

Above the 500 Hz, the difference between target specification and measured noise comes from the difference of the noise which is proportional to the square root of the output power of the Fabry-Pérot cavity. This is due to the less transmittance of the Fabry-Pérot cavity against the input power (typically $\sim$ 10%). This is assumed to be due to the loss of the mirror. When the loss of the mirrors is 4 ppm, the transmittance can be explained. The difference can be compensated by using low loss mirror or injecting 4 times larger input power into the Fabry-Pérot cavity.

Below 500 Hz, the difference comes from the intensity noise of the Fabry-Pérot cavity. The intensity noise should be reduced at most 10 times smaller to reach the designed sensitivity above 100 Hz. Currently, the origin of the intensity noise is not understood, however, it can be reduced by the stabilization of the output intensity by using AOM. Another source of the origin of the difference comes from the frequency noise. Although the frequency noise is almost limited by the detection

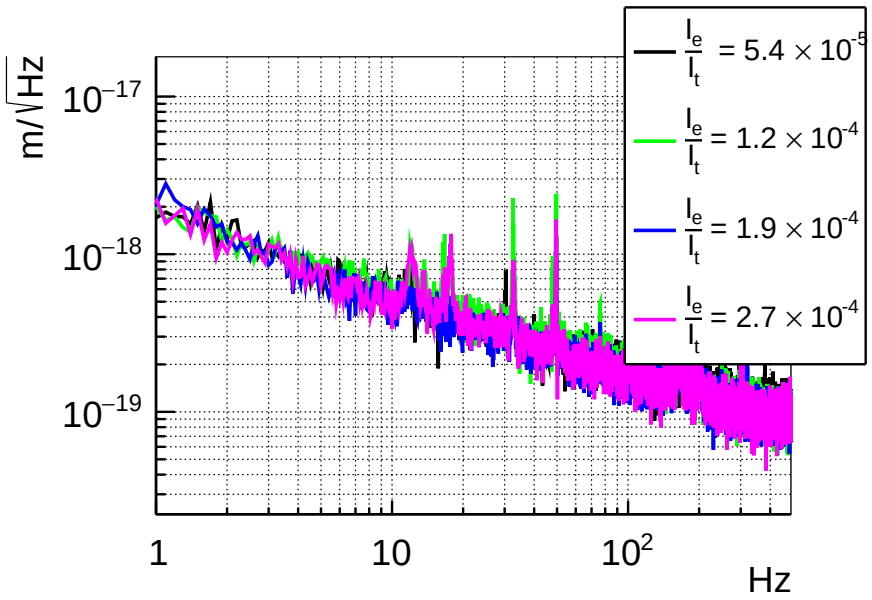

Figure 3.27: Noise spectrum of optical pass difference at difference rotational alignment of the mirror.

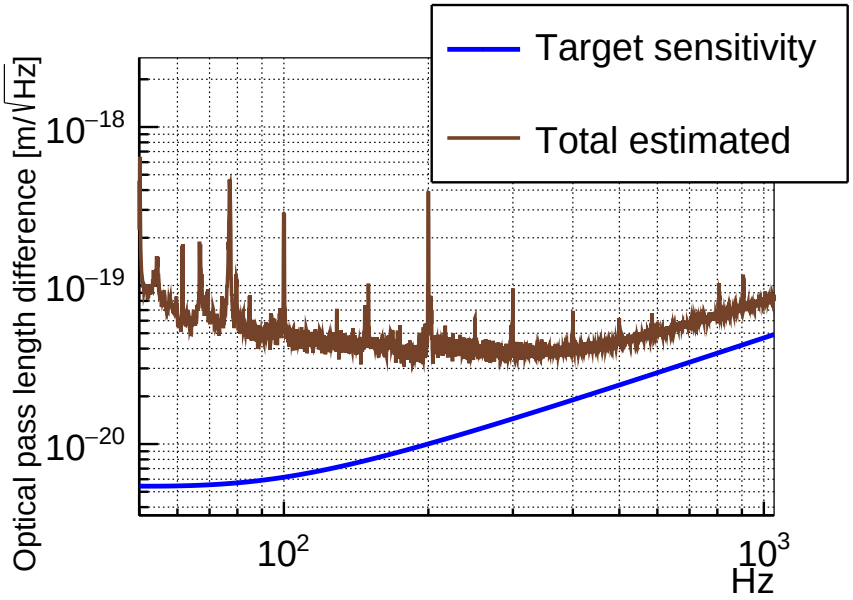

Figure 3.28: Comparison of the sensitivity between designed value and measure value of known noise source. The brown line is the sum of the known noise sources evaluated in the previous chapter. The blue line is the design sensitivity discussed in Chapter 2.8.

noise below 100 Hz, at higher frequency, the effect can be reduced by strengthening the feedback gain of the PDH method.

3.3.6 Discussion of the measured sensitivity

Figure 3.29 shows the measured sensitivity and the expected noise which is the sum of all estimated noise. In this experiment, the frequency region from 100 Hz to 1 kHz is important for the sensitivity considering the timing profile of the pulsed magnet. As shown in Fig. 3.29, above 700 Hz, the sensitivity can be explained by the estimated noise and its limiting noise source is shot noise as expected. Below 700 Hz, the clear discrepancy between the measured and the expected sensitivity can be observed. Its mirror rotation dependence is measured for the first time, and it is observed that the noise behaves as birefringence. The situation and size below 100 Hz are the similar to the previous experiment [37]. It seems to indicate that the unknown noise source not depending on the detail of the experimental setup exists and its effect exists even at higher frequency. In the previous experiment, it is observed the birefringence noise depends on the modulation depth of PEM, which is used to modulate the in polarization for heterodyne detection. It becomes clear that the unexpected noise exists even without PEM. As the noise disappears

without the Fabry-Pérot cavity, the Fabry-Pérot cavity itself is noise source. As the investigation of the observed noise excess, the following studies are performed.

- measurement of the correlation between the displacement noise
- calculation and comparison with the thermal noise
- measurement with the lower finesse cavity

However, they do not lead to the explanation of the origin of the noise excess. The detailed discussion about these studies and the comparison with other experiment is summarized in appendix D.

Though the sensitivity is limited by the unexpected noise source, by suppressing the contribution from the known noise source, the sensitivity around from 200 Hz to 900 Hz is $\sim 1 \times 10^{-19}$ [m/$\sqrt{\text{Hz}}$]. The sensitivity is 5 times better than the sensitivity at around 10 Hz, which is used in the experiment with permanent magnet. The estimated sensitivity from obtained noise spectrum is 3 times worse than the designed sensitivity. The sensitivity is less affected by the noise excess compared to the previous experiment, but the identification of the origin of this noise is important for future work.

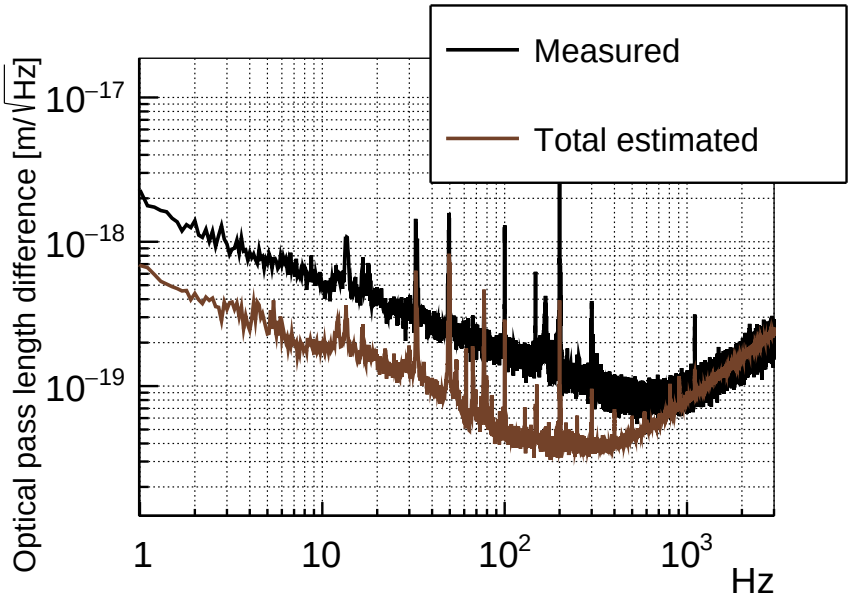

Figure 3.29: Comparison between measured noise and the estimated noise spectrum. Above 700 Hz, the measured noise agrees with the expected noise, and the limiting noise source is shot noise. Below 700 Hz, the discrepancy between the measured noise and expected noise is observed. This noise is found to be behaves as the birefringence.

3.4 Pulsed magnet

2 types of pulsed magnet are developed for this experiment. In this section, the basic specification of the magnet are described. One is a magnet with a single racetrack coil, the other is a magnet with the dipole racetrack coil. Former magnet is used for VMB measurement with strong magnetic field. The latter is developed for validation run with gases. This is because the dipole magnet has small longitudinal magnetic field compared with the single racetrack magnet which induces faraday rotation of gases.

3.4.1 Single race-track magnet

Design and specification

Figure 3.30 shows the schematic view of the single racetrack pulsed magnet. The coil is wound by a 1 mm×3 mm copper wire with 15 turn and its length is 200 mm. A beam pipe whose diameter is 6.3 mm diagonally passes through the center of the magnet. The laser runs through the center of the beam pipe. The coil is reinforced by the stainless steel 304 backup to suppress the deformation due to Maxwell stress. The total length including the reinforcement is 330 mm.

This magnet has non-zero longitudinal magnetic field as the beam pipe runs through the coil diagonally. This longitudinal field induces faraday rotation of gases during the gas measurement. Table 3.2 summarizes the specification of this magnet.

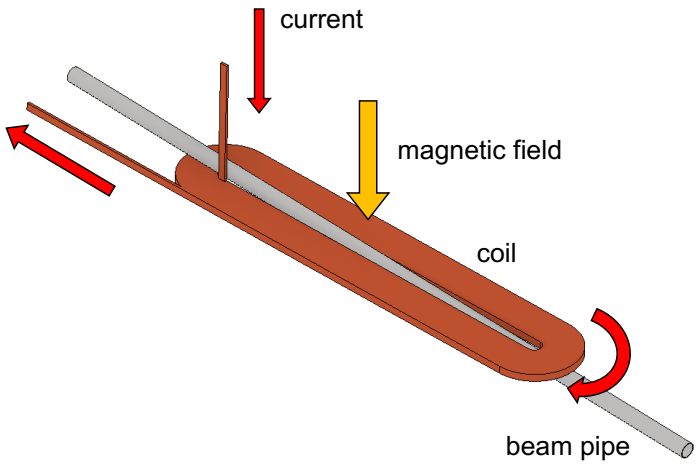

Figure 3.30: Schematic view of the single racetrack magnet. The magnet is consisted with a racetrack shaped coils whose length is 200 mm. At the center of the coils, a beam pipe whose diameter is 6.3 mm is located. A beam pipe whose diameter is 6.3 mm diagonally passes through the center of the magnet.

Table 3.2: Specification of the single coil magnet

Parameter	value
Wound wire	Cu (1 [mm]×3 [mm])
Coil shape	single racetrack
Field length	165 [mm]
Operation field	8.3 T
Aperture size	ϕ1/4 inch (=6.35 [mm]), thickness 0.5 [mm]
Destruction field	12 [T]
Total length	330 [mm]
Weight	16 [kg]
Resistance	9 [mΩ] @ DC
	23 [mΩ] @ 750 Hz
Inductance	40 [μH] @ 750 Hz

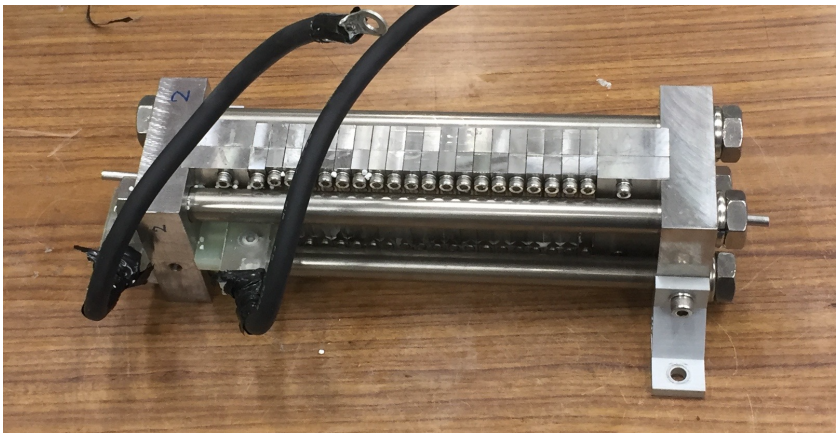

Figure 3.31: Picture of the single racetrack pulsed magnet. The total length after the reinforcement is 330 mm. A beam pipe whose diameter is 5.3 mm passed thorough the magnet.

Pulse shape and Field efficiency and field length

The measured time profile of the magnet is shown in Fig. 3.32. The width is 1.2 ms. Field efficiency is the ratio between the generated magnetic field at the center of the magnet and current flowing the coil. The current is measured by a current transformer, and the magnetic field is measured by the calibrated pick-up coil inserted to the center of the beam pipe. The field

efficiency g is measured as

$$g \equiv B(t)/I(t) = 0.6 \text{ [T/kA]}. \tag{3.20}$$

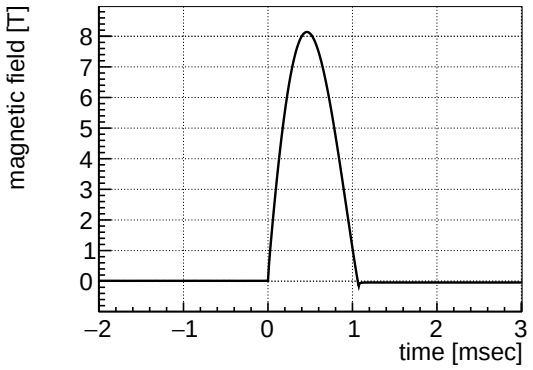

Figure 3.32: Measured timing profile of the magnetic field. The charging voltage is 2 kV. The peak magnetic field is 8.2 T. The pulse width is 1.2 ms.

The effective field length is defined as follows,

$$L_{\text{eff}} = \frac{\int B^2(z)dz}{B^2(0)}, \tag{3.21}$$

where z axis lies along the beam pipe and the origin of the z-axis is the center of the magnet. The field map is measured by inserting calibrated pick up coil into the beam pipe along the beam path. Figure 3.33 shows the square of the magnetic field as a function of the position normalized by that at the center of the magnet. From this map, the effective field length $L_{\text{B}}^{\text{eff}}$ is calculated to be

$$L_{\text{eff}} = 165 \text{ [mm]}. \tag{3.22}$$

The field map of the longitudinal magnetic field is calculated by using ANSYS. Fig. 3.34 shows the calculated field map. As the field efficiency becomes larger near of the coil, the map has 2 peaks due at the corner of the coil.

Heating and repetition rate

As the wire of the coil has nonzero resistivity, the temperature of the coil increases when a current flows, and the magnetic field is generated. Since too high temperature leads to the destruction of the coil, the repetition rate of the pulse operation should be slow enough to maintain the temperature of the coil under the thermal equilibrium.

To determine the repetition rate, the time evolution of the resistivity is used. The joule heating is proportional to the resistivity of the coil. The total

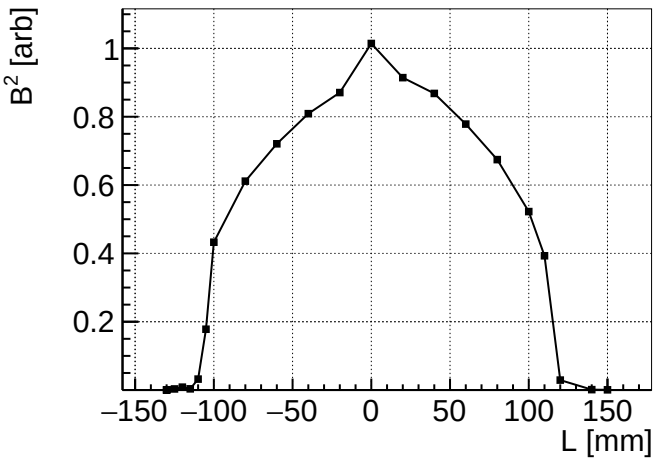

Figure 3.33: The distribution of the squared magnetic field along the beam pipe. The value are normalized by that at the center ($z = 0$).

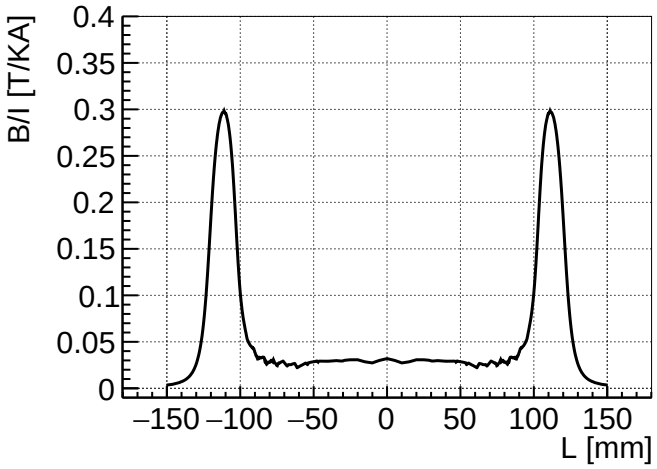

Figure 3.34: Distribution of the field efficiency of the longitudinal magnetic field calculated by ANSYS.

energy loss due to the joule heating can be obtained from the charged voltage of the capacitance before and after generating the pulse by $C\frac{V_0^2}{2} - C\frac{V_1^2}{2}$. When the temperature of the coil is under the thermal equilibrium, this energy loss becomes constant. By monitoring the energy loss during the operation of the magnet, the repetition rate is set at least longer than ~ 18 s/pulse.

Stray field

As discussed in chapter 2, the mirrors also show the cotton-mouton effect. The stray field at the mirror should be taken into account to discuss the systematic effect. The stray field 50 cm away from the magnet is less than 1 mT. The Cotton-Mouton effect of the mirror is calculated to be at most 6 times larger than the signal of VMB effect. However, this effect is negligible considering the current sensitivity.

3.4.2 Dipole magnet

Design and specification

Figure 3.35 shows the schematic view of the pulsed magnet. This magnet is a dipole magnet which is consisted with two racetrack shaped coils. The coil is wound by a 1 mm×3 mm copper wire with 10 turn and its length is 170 mm. At the center of the coils, a beam pipe whose diameter is 6.3 mm is located. The laser is at the center of the beam pipe. The total length after the reinforcement is 260 mm.

Comparing with the single racetrack magnet, the advantage of the dipole magnet is small longitudinal magnetic field. Therefore, this magnet is mainly used for the validation run with gases. Table 3.3 summarizes the specification of the dipole magnet.

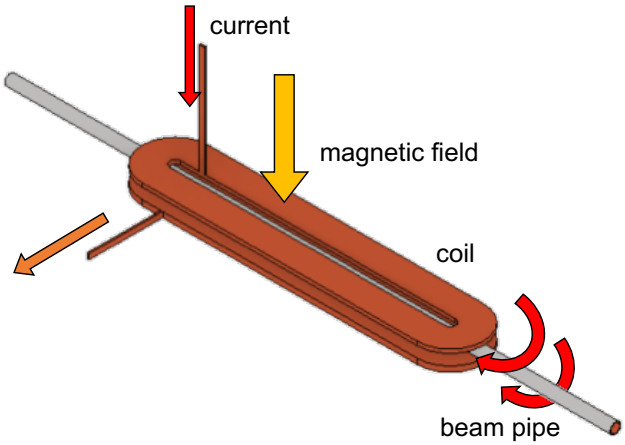

Figure 3.35: Schematic view of the dipole magnet. The magnet is consisted with 2 racetrack shaped coils whose length is 170 mm. At the center of the coils, a beam pipe whose diameter is 6.3 mm is located.

Pulse shape, Field efficiency and field length

The timing profile of this magnet is shown in Fig. 3.37. The pulse width is 1.2 ms. The field efficiency is evaluated in the same way with the single

Table 3.3: Specification of the dipole magnet

Parameter	value
Wound wire	Cu (1 [mm]×3 [mm])
Coil shape	dipole racetrack
Field length	150 [mm]
operation field	1 T
Aperture size	ϕ1/4 inch (=6.35 [mm]), thickness 0.5 [mm]
Destruction field	Not measured
Total length	∼260 [mm]
Weight	16 [kg]
Resistance	8.5 [mΩ] @ DC
	28 [mΩ] @ 750 Hz
Inductance	43 [μH] @ 750 Hz

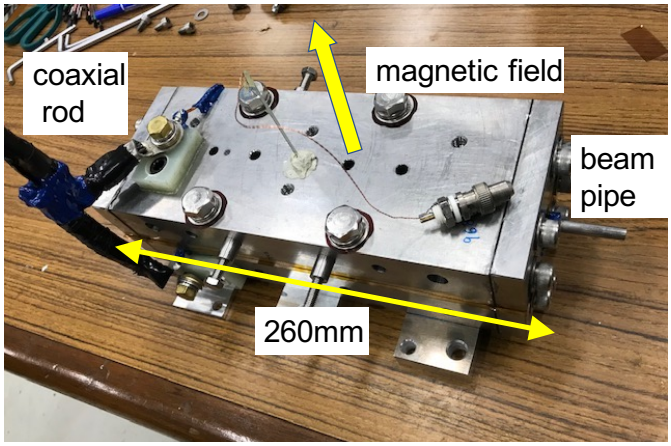

Figure 3.36: Picture of the dipole pulsed magnet. The total length after the reinforcement is 260 mm. Beam pipe whose diameter is 5.3 mm passed thorough the magnet.

race-track magnet. The measured efficiency is

$$g = B(t)/I(t) = 1.0 \text{ [T/kA]}. \tag{3.23}$$

The position map of the dipole magnet is also measured in the same way with the racetrack magnet. Figure 3.38 shows the square of the magnetic field normalized by that at the center of the magnet as a function of the position . From this map, the effective field length $L_{\mathrm{B}}^{\mathrm{eff}}$ is calculated to be

$$L_{\mathrm{eff}} = 150 \text{ [mm]}. \tag{3.24}$$

As the beam pipe is parallel to the coil, the longitudinal component of the magnetic field is 0 by design.

3.5 Magnet operation system

3.5.1 Overview of the magnet operation system

Figure 3.39 shows the schematic view of the magnet system. The magnet is put in the liquid nitrogen container box which is fixed to the magnet bench. The magnet is connected to the mirror chamber. The magnet is surrounded by double iron plates. They act as both magnetic shield and soundproof. The current is supplied from the capacitor bank. The level of the liquid nitrogen is monitored by the level indicator.

3.5.2 Magnet bench and liquid nitrogen container

To reduce the joule heating, pulsed magnets are operated at the liquid nitrogen temperature. The pulsed magnet and inner iron shield and beam pipe are contained in the liquid nitrogen container box. Figure 3.40 shows the setup inside the liquid nitrogen box. The liquid nitrogen container is fixed to the magnet bench. The magnet bench is made with stainless steel 304 and mechanically isolated from the optical bench.

3.5.3 Charging unit and the capacitor bank

The charging unit for the pulsed magnet is originally developed for ALPs search experiment at SPring8, the detail of this system is discussed in Appendix C. The magnet is connected to the 3 mF capacitor via a coaxial cable. The charging unit

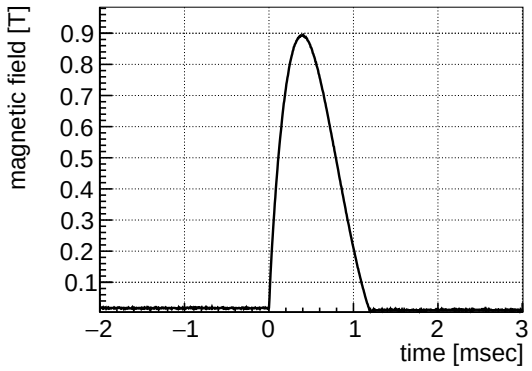

Figure 3.37: Measured magnetic field shape. The charging voltage is 200 V. The peak magnetic field is 0.9 T.

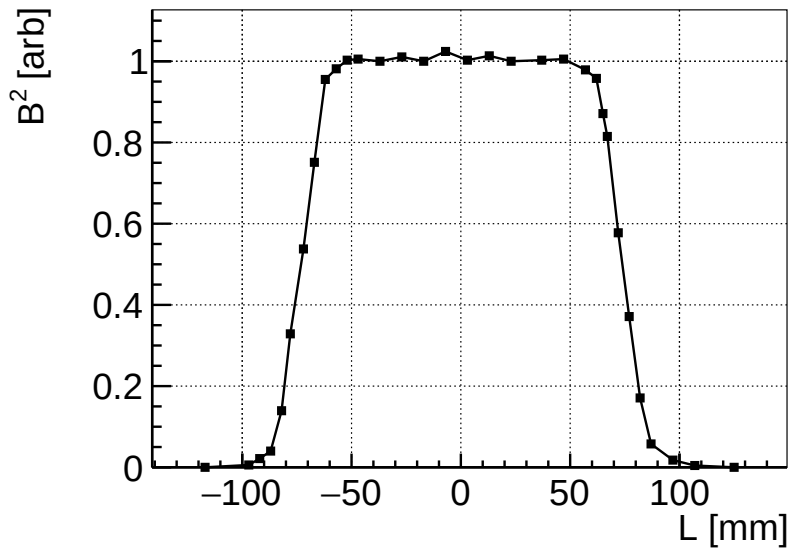

Figure 3.38: Measured square of the magnetic field as a function of the position along the beam pipe normalized by the square of the magnetic field at the center of the coil ($z = 0$).

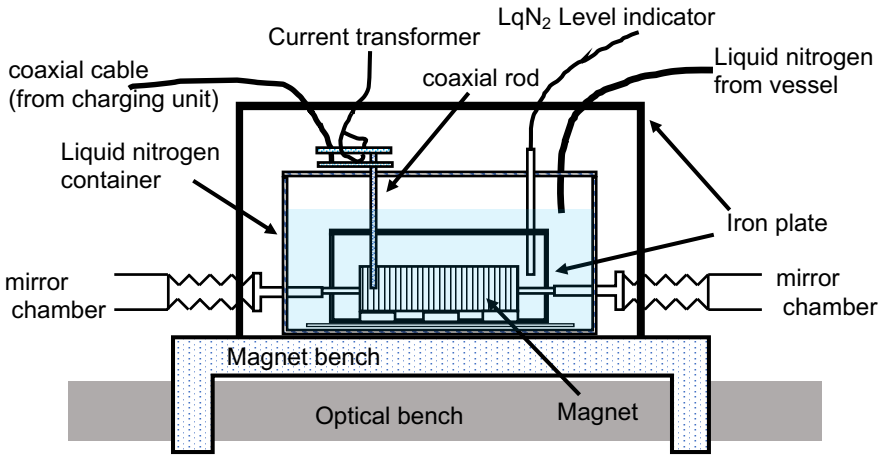

Figure 3.39: Schematic of the magnet system. On the magnet bench, the liquid container is placed. A magnet is inside the container. The magnet is surrounded by the double iron plate. A coaxial cable, a liquid nitrogen level indicator, and a current transformer are also installed.

is developed to charge the capacitor to specified voltage automatically. During the

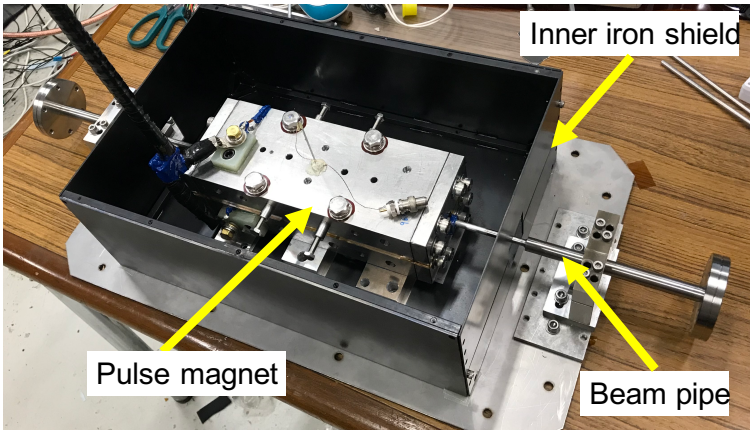

Figure 3.40: Setup inside the liquid nitrogen container. The pulsed magnet is fixed to the stainless steel 304 base plate with the inner iron shield and a beam pipe.

Table 3.4: Specification of the current transformer

parameter	specification
Sensitivity	0.2 [mV/A]
Low frequency cutoff	1 [Hz]
High frequency cutoff	14 [MHz]
Peak current	30 [kA]
Peak isolation voltage	5 [kV]

operation of the magnet, the capacitor is charged to ± 4.5 kV maximally depending on the sign of and the size of the magnetic field.

3.5.4 Current transformer

The pulse shape and the current flow is measured by a current transformer (CWT-MiniHF400) during the data acquisition, and it is shown in Fig. 3.41. Its specification is shown in Table 3.4. From the measured current shape and field efficiency, the generated magnetic field is calculated for each pulse.

3.5.5 Liquid nitrogen serving system

During the operation of the magnet, Joule heating and natural evaporation consume the liquid nitrogen. For every $2 \sim 3$ hours, the liquid nitrogen container should be filled. The height of the liquid nitrogen is monitored by a level indicator made of Pt-100. When the level of liquid nitrogen become lower than the operation level, the solenoid valve attached to a liquid nitrogen vessel is opened, and liquid nitrogen

is supplied from the vessel until the level reaches the stable operation level. During the solenoid valve is opening, an exhaust fan is also activated. It exhausts cold gas from the clean room to outside. Each vessel can contain 100 L liquid nitrogen. For $2 \sim 3$ times a day, the vessel should be exchanged to another vessel.

3.5.6 Control board

Figure 3.43 shows the control board of the magnet system. It has following functions.

- initial setting
- charged voltage indicator (DMR)
- pulser

Figure 3.41: Current transformer. The current flowing inside the loop at the right side of the picture is converted to voltage signal.

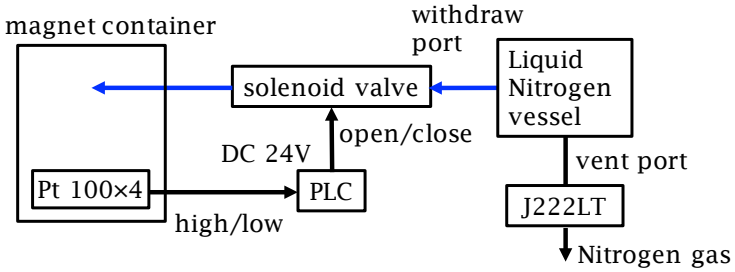

Figure 3.42: Schematic view of liquid Nitrogen serving system

- current shape error check

Before the operation of the magnet, the setting is initialized by hand. The charging voltage for positive charging and negative charging is pre-setted and operation mode (single pulse or repetition mode) are selected. A digital meter relay (DMR) reads out the charged voltage of the capacitor. When the readout voltage of DMR exceeds the preset charging voltage, the signal is sent to the charging unit to stop the charging. The pulser is used to send the trigger signal for discharging the charged voltage to the charging unit via optical fiber. To prevent from an accident caused by a damaged coil operation, the shape of the pulse current is checked pulse by pulse. A Mask function of an oscilloscope (LeCroy wave runner 6050A) is used for this check. Once a pulse shape difference from a pre-recorded waveform is found by the oscilloscope, a stop TTL signal is sent to the capacitor bank.

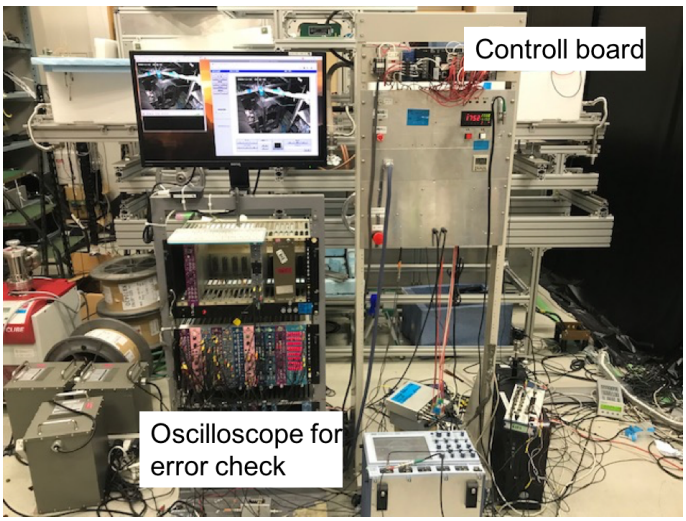

Figure 3.43: Picture of control board. The capacitor bank is operated via this control board.

3.5.7 Evaluation of the effect of the disturbance

Stability of the cavity

The main challenge of this work is to establish the stable operation of a Fabry-Pérot cavity with a pulsed magnet. In the previous experiment, the resonance of a Fabry-Pérot cavity is lost 10 ms after the magnetic field generation, and its peak field is 6.5 T [54].

To study the stability of the setup, test operation of the pulsed magnet is performed. Fig 3.44 shows the result of the test operation. The top figure shows generated magnetic field, and its peak field is 8.2 T. The middle figure is frequency fluctuation estimated from the error signal. The bottom figure

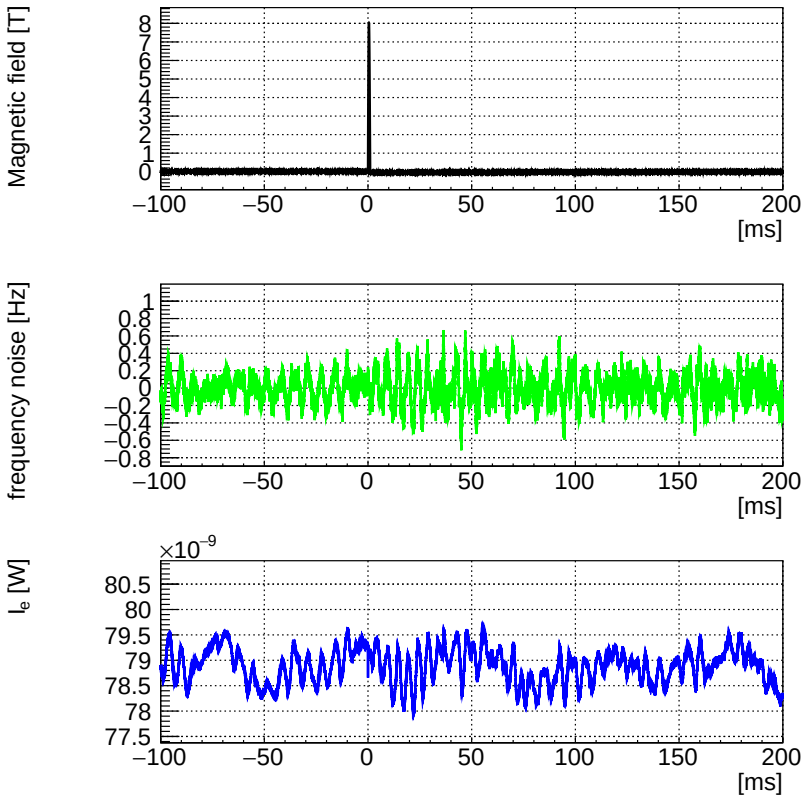

Figure 3.44: Evaluation of the stability of the Fabry-Pérot cavity against the operation of the pulsed magnet. Top: magnetic field. Middle: Estimated frequency noise. Bottom: output intensity of I_e.

shows the intensity fluctuation of $|_e$. No signs of the lost of the resonance is observed in I_e, and the estimated frequency fluctuation is sufficiently smaller than the FWHM of the resonance, which is 220 Hz. Compared to the previous experiment, even though the peak field is larger, the highly stable operation of a Fabry-Pérot cavity is established. This stability enables the fast repetitive operation of the pulsed magnet.

Adjustment of the position of the beam pipe

Although the resonance of the cavity is robust against the disturbance from the magnet, the fluctuation of the I_e is observed at the same time with the pulsed magnet depending on the relative position between the beam pipe and the laser.

The distance of the magnet from the optical bench can be tuned along the vertical direction by the adjuster attached to the bottom of the magnet bench, thus the relative position between the beam path and beam pipe can be

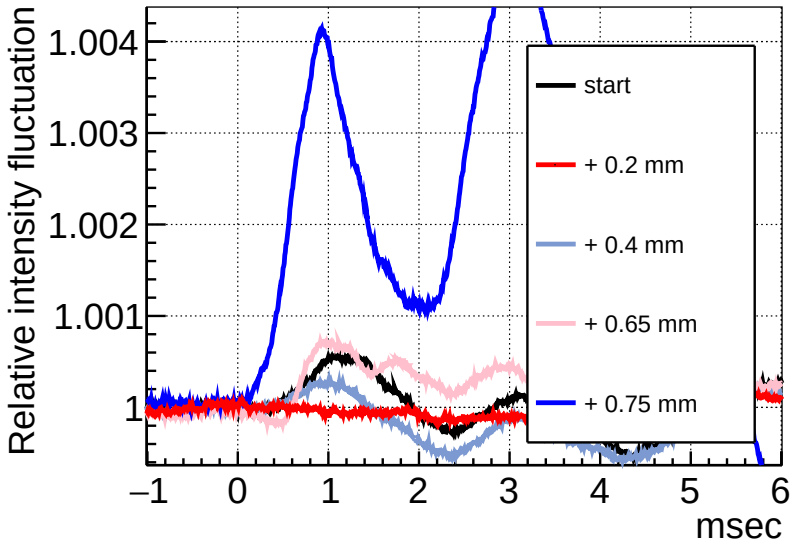

Figure 3.45: Alignment dependence of the intensity noise of I_e. The distance of the beam pipe from the optical bench is changed along the vertical direction. At each position, the intensity noise of I_e induced by the magnet is measured. Every waveform is the average of 50 pulses. The pulse field is generated at $t = 0$, and its peak is 8.3 T. The vertical position of the magnet is changed from initial position (black line) to 750 μm higher (blue line). The different size of the intensity fluctuation can be seen, and it becomes smallest at the specific position (red line).

changed. Figure 3.45 shows the relative intensity noise of I_e during the operation of the magnet measured at the difference distance of the magnet from the optical bench. Every waveform is the average of 50 pulses. The pulse field is generated at $t = 0$, and its peak is 8.3 T. The vertical position of the magnet is changed from initial position (black line) to 750 μm higher (blue line). The different size of the intensity fluctuation can be seen depending on the position of the magnet, and the intensity noise disappears at the specific position of the magnet bench (red line).

As the intensity noise depends on the relative position between beam path and beam pipe, it is not VMB signal, and not also the effect of the cavity instability. Currently, it is assumed that these intensity fluctuation is due to the scatter of I_e by the inner surface of the beam pipe. The position of the magnet bench is adjusted by scanning the level of the magnet bench at the intervals of 200 μm before the measurement.

Table 3.5: Specification of the absolute pressure gauge

parameter	specification
Full scale	1.333 [kPa]
Lower limit	0.1 [Pa]
Accuracy	0.2%
Resolution	0.06 [Pa]
Bandwidth	33 [Hz]

3.6 Other components

3.6.1 Electromagnetic noise reduction

The strong magnetic field and current could induce the electromagnetic noise. As these noise appears at the same time with magnetic field, the reduction of the electromagnetic noise is necessary. For the reduction of the noise, the master laser, every photo detector is shield by the 1.6 mm iron plate.

3.6.2 Laser displacement sensor

The laser displacement sensor HG-C1100 (Panasonic) is used to measure the vertical distance between the optical bench and magnet bench. The measurement range is ± 35 mm, and measurement center distance is 100 mm. The resolution is 10 μm. Total four sensor is used. These sensors are used when adjusting the vertical distance between the optical bench and magnet bench.

3.6.3 Vacuum system

Figure 3.46 shows the schematic view of the vacuum system. Each mirror chamber is connected to a turbomolecular pump. A scroll pump is used as a roughing vacuum pump for the two turbomolecular pumps. The chambers are also connected to the gas cylinder for calibration measurement by gas. All of these components are connected with bellows hoses to isolate the vacuum chamber from the vibration of the pumps.

Three pressure gauge are used for this system. One is the absolute capacitance pressure gauge (M-342DC-11) whose range is 1 Pa $\sim$ 1000 Pa. This gauge is used for gas measurement to monitor the gas pressure precisely. The specification of the absolute pressure gauge in summarized in Table 3.5. The other 2 are Cold Cathode Gauge whose range is $10^{-9} - 10^{-2}$ hPa. They are connected to each mirror chamber. They are used to monitor the pressure during the vacuum measurement.

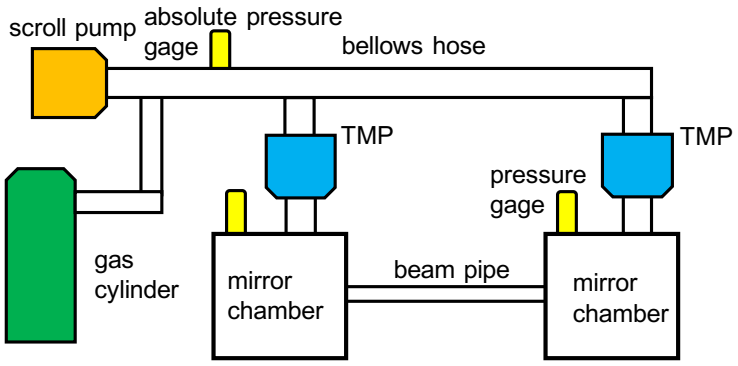

Figure 3.46: Schematic view of vacuum system

3.6.4 Data logger

PCI-6229 and PCI-6225 (National Instrument) are used as data logger throughout this experiment. The sampling rate is 160 kHz. The full scale is ±10 V and the resolution is 16 bits. The quantization noise V_{ADC} is calculated to be

$$\begin{aligned} V_{\mathrm{ADC}} &= 2 \times V_{\mathrm{full}}/\sqrt{6 \times f_{\mathrm{samp}}} \\ &= 2 \times 10/\sqrt{6 \times 160 \times 10^3} \\ &\sim 3 \times 10^{-7}\ [\mathrm{V}/\sqrt{\mathrm{Hz}}]. \end{aligned} \tag{3.25}$$

This is small enough compared to the intrinsic noise of all photo detectors.

Chapter 4

Run and analysis

In this chapter, the data acquisition and its analysis are described. First, the summary of the data acquisition is described. Then the basic analysis procedure is introduced. After that, the measurement and analysis of the Cotton-Mouton effect of the nitrogen gas is described as the analysis validation. Finally, the measurement and the analysis of VMB is described. The systematic uncertainty is also described.

4.1 Summary of data acquisition

4.1.1 Run time

Table 4.1 summarize the data sets. The validation run was performed with the dipole magnet at the room temperature on Sep. 30. The charging voltage are 200 V and -200 V, respectively. Total 800 pulses are generated during this measurement. The measurement of VMB was performed with single racetrack magnet from Nov. 13 to Dec. 10. The charging voltage are 2 kV and -1 kV respectively. Total 26000 pulses are generated during this measurement. The data sets of vacuum measurement are divided to 2 groups (B-1, B-2 and C-1, C-2). The sign of the static birefringence of the mirrors is reversed for each data set groups. These information is used to cancel the systematic effect.

Table 4.1: Summary of the data set

run ID	data	target medium	magnet	charging voltage	pulse
A-1	30/9/20	N_2	dipole	200 V, -200 V	800
B-1	16/11/20-20/11/20	vacuum	single	2 kV, -1 kV	6500
C-1	23/11/23-26/11/20	vacuum	single	2 kV, -1 kV	8000
B-2	30/11/20-4/12/20	vacuum	single	2 kV, -1 kV	6200
C-2	7/12/20-10/12/20	vacuum	single	2 kV, -1 kV	5600

4.1.2 Run cycle

The basic run cycle and the operation procedure is described.

During the measurement, the electric light inside the clean room is turned off to avoid the stray light. Before stating the repetitive operation of the pulsed magnet, the charging voltage of the positive and negative magnetic field is set by using the control board of the charging unit. After that, the initial charging of the capacitor is started, then the capacitor bank is switched to the repetitive operation mode. The waveform of the magnetic field and the output intensity of I_t is monitored during the repetitive operation mode. When errors are detected in the waveform of the magnetic field or the output intensity of I_t becomes lower than the pre-defined threshold voltage, the operation of the charging unit is stopped automatically. The magnet container is filled with liquid nitrogen during the VMB measurement and the liquid nitrogen is served automatically for every 3 hours. The consumption of the liquid nitrogen is $\sim$ 200 L for each day.

During the repetitive operation, the charging unit repeats the following operations. The capacitor is charged to positive operation voltage, and when the trigger signal from the control board is inputted, the charge is released to the magnet. After that, the charging to the negative charging voltage is started. The charge is also released by the trigger from the control board, then the charging of the positive operation voltage is started again. The trigger is also sent to the ADC to record the waveforms.

4.1.3 Data acquisition cycle

The data acquisition cycle is consisted of the acquisition of the 3 types of data set which is described below. Figure 4.1 shows the time chart of the charged voltage, magnetic field and data type.

1st data The data contains the waveform of V_e, V_t, V_{err} and out put voltage of the current transformer. The capacitor is charged to positive operation voltage and the positive magnetic field is generated. The waveform includes time series -300 ms before and 300 ms after the magnetic field.

2nd data The capacitor is charged to negative charging voltage The data contains the waveform of V_e, V_t, V_{err} and magnetic field. The capacitor is charged to negative operation voltage and the negative magnetic field is generated. The waveform includes time series -300 ms before and 300 ms after the magnetic field.

3rd data This data set contains the waveform when magnetic field is not applied. This data is used to discuss the expected noise and stability of the cavity. The data contains the waveform of V_e, V_t, V_{err} during 600 ms. The interval between 2nd data and 3rd data is 2 [s].

4.2 Analysis method

In this section, the analysis procedure is described.

4.2.1 Calculation of the ellipticity

From the voltage output of the 2 photo detectors, the intensity of the ordinary light (I_t) and extraordinary light (I_e) is calculated as follows,

$$I_t = G_t V_t \tag{4.1}$$
$$I_e = G_e V_e, \tag{4.2}$$

where V_t and V_e are the voltage output of the PD_t and PD_e, and G_t and G_e are the gain of the each photo detector.

The ellipticity is calculated from the ration of these intensity as follows,

$$\text{Ellipticity} \equiv \left(\frac{I_e}{I_t}\right). \tag{4.3}$$

As discussed in Section 2 and section B, the function form of the ellipticity can be written as follows,

$$\frac{I_e}{I_t} = \Gamma^2 + \eta B^2 + \kappa B + \xi \frac{dB}{dt}. \tag{4.4}$$

The 1st term of the above equation comes from the static birefringence induced by the mirrors. The 2nd term is proportional to the square of the magnetic field

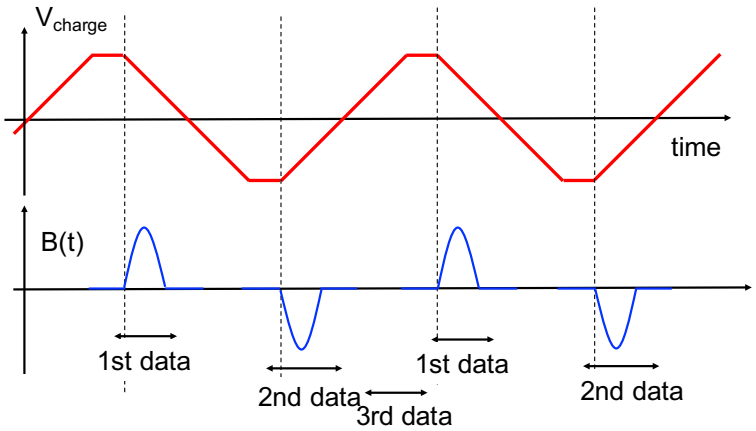

Figure 4.1: Time chart of the DAQ cycle. 3 types of the data are acquired during the run. first data and second data correspond to the data during the positive magnetic field and negative magnetic field respectively. Third data corresponds to the data without magnetic field

and VMB signal could appear in this term. The 3rd and the last terms include the effect of the Faraday rotation due to the residual gases and the effect of the electromagnetic noise which would not appear ideally. To get rid of the last 2 terms from the ellipticity, the sign averaged ellipticity $H(t)$ is defined as follows by averaging the ellipticity of the 1st data and 2nd data weighting by the ratio of the peak magnetic field to cancel the effect which depends on the sign of the magnetic field.

$$H(t) \equiv \frac{1}{2}\left(\left(\frac{I_e}{I_t}\right)_1 + \frac{B_+}{B_-}\left(\frac{I_e}{I_t}\right)_2\right), \tag{4.5}$$

where B_+ and B_- are the peak magnetic field of the 1st data and 2nd data respectively. $\left(\frac{I_e}{I_t}\right)_1$ and $\left(\frac{I_e}{I_t}\right)_2$ are the measured elliplicity in the 1st data and 2nd data respectively.

The effective magnetic field used for the fitting is defined as follow,

$$B^2_{\text{eff}} \equiv \frac{1}{2}\left(B(t)^2_+ + \frac{B_+}{B_-} \times B(t)^2_-\right), \tag{4.6}$$

where $B(t)^2_+$ and $B(t)^2_-$ are the timing profile of the square of the magnetic field of the 1st data and 2nd data, respectively.

4.2.2 Calculation of the signal shape

As discussed in chapter 2, the Fabry-Pérot cavity acts as frequency filter against the VMB. It is necessary to calculate the expected signal shape from the applied magnetic field shape. The cut-off frequency is calculated from the measured finesse. Figure 4.2 shows the expected signal shape. The signal shape without the cavity filtering is drawn for comparison.

4.2.3 Parameter estimation

As the noise spectrum is not a white noise, it is not suitable to perform a parameter estimation in time domain. Instead, the parameter estimation is performed in the frequency domain, assuming the noise spectrum is stationary.

The log likelihood function for parameter estimation is defined as follows,

$$\log L(\eta) = -\Delta f \sum_{k=1}^{n} \frac{(\tilde{H}(f_i) - \eta \times \tilde{B^2_{\text{eff}}}(f_i))^2}{S(f_i)}, \tag{4.7}$$

where Δf is the sampling frequency, $\tilde{H}(f_i)$ is the Fourier component of the measured ellipticity $H(t_i)$ whose frequency is f_i, $\tilde{B^2_{\text{eff}}}(f_i)$ is the Fourier component of signal shape which is calculated in the previous section, η is the free parameter to be estimated defined above and $S(f_i)$ is the power spectrum density of the ellipticity without the operation of the magnet. This expression can be understood

as the minimization of the residuals between measured ellipticity and signal shape weighted by the intrinsic noise level of ellipticity at each frequency bin. the The power spectrum of all 3rd data during each run are used to obtain $S(f)$. Figure 4.3 shows the example of $S(f)$ obtained during the validation run and $B^2(f)$.

From the discussion of the section 2 and section B, k_{cm} is acquired from the η

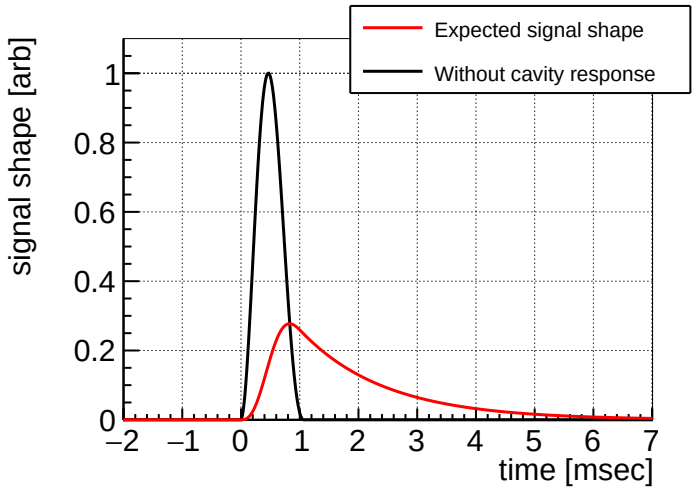

Figure 4.2: Waveform of the calculated expected signal shape. The signal shape without a cavity response is also drawn for comparison

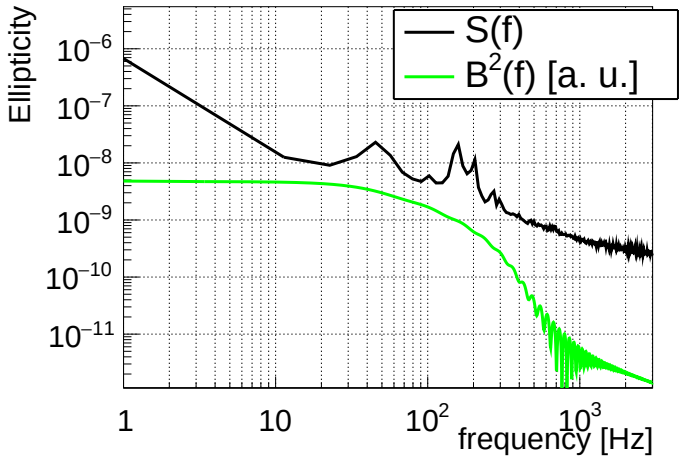

Figure 4.3: Example of PSD of $S(f)$ and $B^2(f)$.

as follows,

$$k_{\mathrm{CM}} = \frac{\lambda}{4FL_{\mathrm{B}}\Gamma\kappa^2}\eta. \tag{4.8}$$

Finesse and κ is measured before the measurement. Γ is the static ellipticity induced by the mirror and defined as the ellipticity just before applying the magnetic field.

The parameter estimation is performed for every cycle during the data acquisition. From the distribution of k_{CM} of all the cycles, the mean values of k_{CM} and its uncertainties is obtained.

4.2.4 Time and frequency windows

Time window

As shown in Section 3.5.7, the effect of the disturbance appears in the error signal. The time window used for the parameter estimation should be chosen not to include the effect of these disturbance to reduce the bias of the parameter estimation due to them. The information of the error signal is used to decide the time window.

Figure 4.4 shows the waveform of the error signal taking the low-pass behavior of the cavity response into the account. The waveform is the average of 200 pulses. The magnet field is generated at $t = 0$, and its peak field is 8.3 T. Though it is not obvious when the effect of the disturbance begins to appear, a large peak appears at $t = 9.3$ ms and it rises around $t = 6$ ms. The end of the time window is chosen at least not to include this peak, then decided to 5 ms after the pulse. The beginning of the time windows is chosen 35 ms before the beginning of the pulse. The total length of the timing window is 40 ms.

Frequency window

As the sampling rate of the ADC is 160 kHz, the Fourier spectrum spread from 0 Hz to 80 kHz. However, the higher frequency region where VMB signal would not appear is useless for parameter estimation. The frequency window is chosen to reduce the bias from these frequency regions and reduce the computing time.

The ideal sensitivity as a function of the end frequency of frequency window can be calculated from the pulse shape and the noise spectrum measured without the operation of the magnet. The left side of Fig. 4.5 shows the result of the calculation. X-axis is the highest frequency used for the parameter estimation and Y-axis is the relative sensitivity against that of using all frequency components. The right side of 4.5 shows the coherence spectrum between the magnetic field and the error signal from 0 to 300 ms after the generating magnetic field. A peak at around 1.25 kHz is observed. This frequency region has almost no contribution to the sensitivity, thus can be

removed without affecting the sensitivity. From these information, the upper frequency of the frequency window is chosen to 1 kHz. Before the VMB measurement, the large peak appears at 50 Hz at the frequency noise and intensity noise of I_e. Currently it is assumed due to the malfunction of Mephisto. To avoid the effect due to this peak, the lower frequency is chosen not to include this peak. The right side of Fig. 4.6 shows the relative intensity noise of the ellipticity signal during VMB measurement. The left side of Fig. 4.6 shows the relative sensitivity as a function of the lowest frequency using for the parameter estimation. The frequency region around 50 Hz does not contribute to the sensitivity. From this figure, the lowest frequency for the parameter estimation is chosen to be 100 Hz.

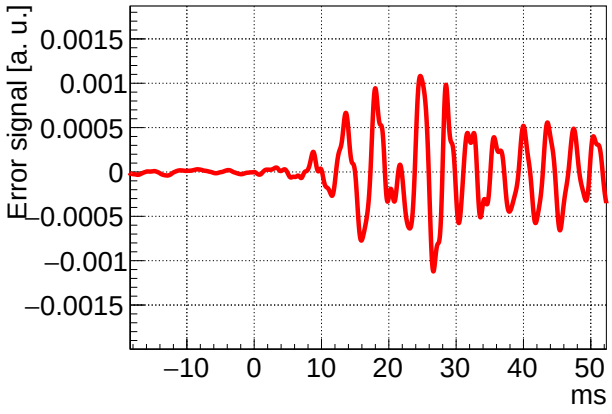

Figure 4.4: The average of the waveform of the error signal. The pulse is generated at t=0. The 200 pulsed are used for averaging. The waveform is filtered by the cavity response. From this figure, the end of the time windows is chosen to be 5 ms.

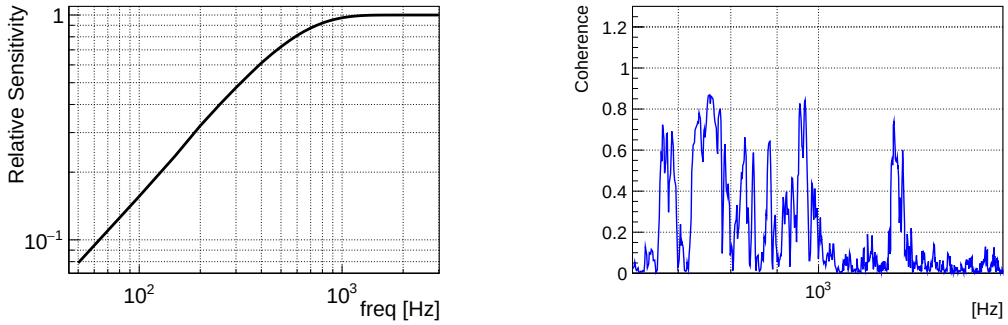

Figure 4.5: Left: Relative sensitivity as a function of the highest frequency of frequency window. X-axis is the highest frequency used for the parameter estimation and y-axis is the relative sensitivity against that of using all frequency components. Right: coherent spectrum between the magnetic field and error signal after the generating the magnetic field.

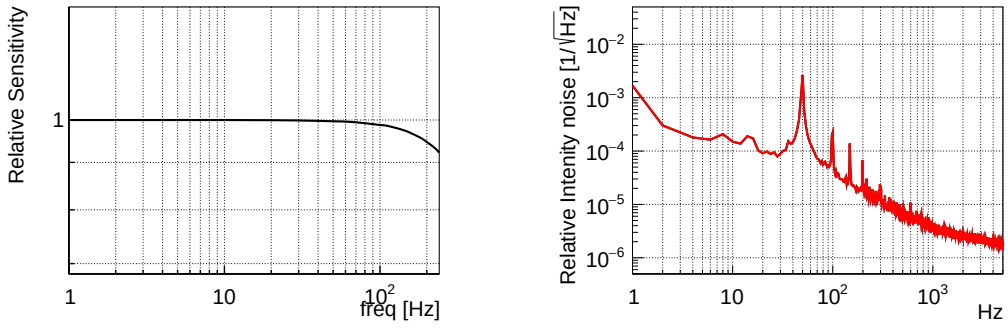

Figure 4.6: Left: Relative sensitivity as a function of the lowest frequency of the frequency window. X-axis is the lowest frequency used for the parameter estimation and y-axis is the relative sensitivity against that of using all frequency components. Right: Relative intensity noise of the ellipticity during the VMB measurement. A large peak at 50 Hz can be seen. Frequency windows is chosen not to include this peak.

4.3 Validation run

The analysis validation run is performed by measuring the Cotton-Mouton (CM) effect of gas. The CM effect has the same magnetic field dependence with VMB effect. Therefore, the measurement of the CM effect of the gas has been used as the validation of the experimental setup in all the previous experiment. In this work, the nitrogen gas, which is one of the most common gas as the validation, is used as the target gas. As the CM effect depends on the pressure of the gas, the pressure dependence is measured. The result is compared with the previous result to validate that the system and analysis works properly.

4.3.1 Summary of the measurement

The dipole magnet is used for analysis validation. The measurement is performed at the room temperature as CM effect depends on the temperature and all the previous measurement is performed at the room temperature. As the magnetic is not cooled, the charged voltage is set to be 200 V to avoid the destruction of the magnet due to the temperature increase.

The mirror chamber and the beam pipe is filled with nitrogen. The pressure is measured by the absolute pressure gauge whose range is from 10 Pa to 1.3 kPa. When gas pressure is more than 100 Pa, the output intensity of Fabry-Pérot cavity becomes unstable. This instability is avoided by decreasing the input power. The measurement is performed at 4 different pressure which are 600 Pa, 700 Pa, 850 Pa and 1000 Pa. For each pressure, total 100 cycles of data are acquired. The measurement time for each pressure is 1 hour.

Finesse and κ are measured before the measurement. No significant pressure dependence of the finesse is observed.

Figure 4.7 shows the example of 1st data when gas pressure is 1 kPa. At t=0, the magnetic field is applied. You can see the change of I_e after applying magnetic field whereas no change can be seen in I_t. Figure 4.8 shows the example of 2nd data when gas pressure is 1 kPa. The change of I_e can be also seen and its sign is the same with 1st data though the sign of magnetic field is the opposite.

The typical parameters used for the analysis is summarized in table 4.2

Table 4.2: Summary of the typical parameters during validation run

parameter	value
Finesse	4.1×10^5
I_t	6.1×10^{-4} [W]
I_e	55 [nW]
$\kappa(\alpha)$	0.86
Peak magnetic field	0.9 [T]
Field length	150 [mm]
Pressure	$600 - 1000$ [Pa]
Temperature	22 [°C]

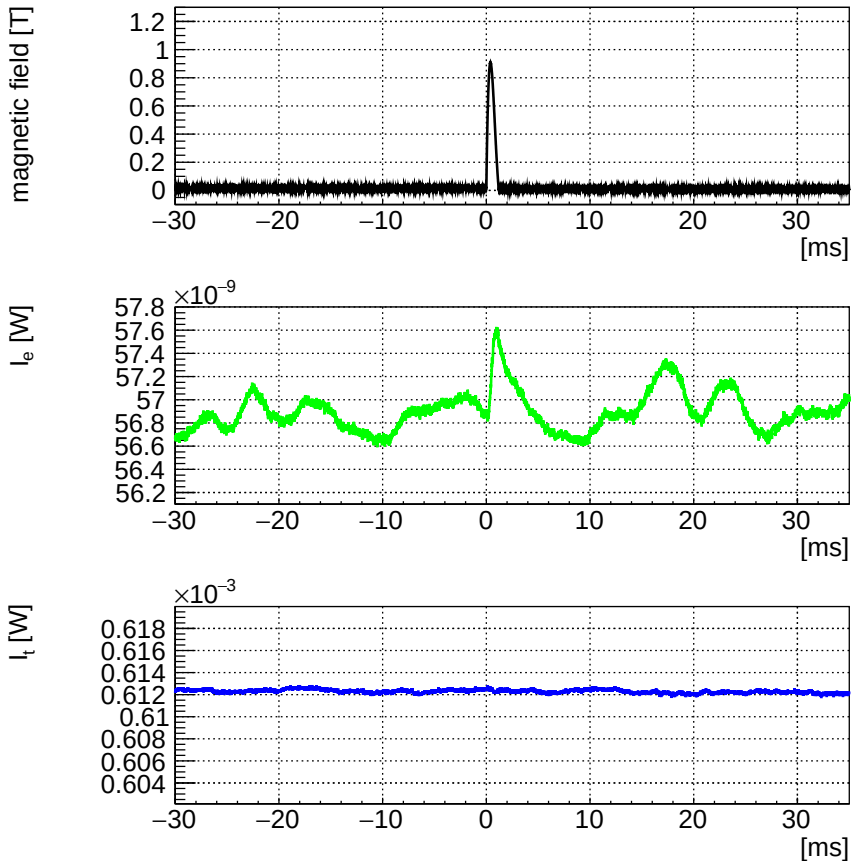

Figure 4.7: An example of the measured data of validation run. Top: magnetic field. middle: I_e. Bottom: I_t. The change of I_e after the magnetic field can be seen whereas no change can be seen in I_t. The range of the Y-axis of the middle and bottom figure is $\pm 1.5\%$ of their DC power.

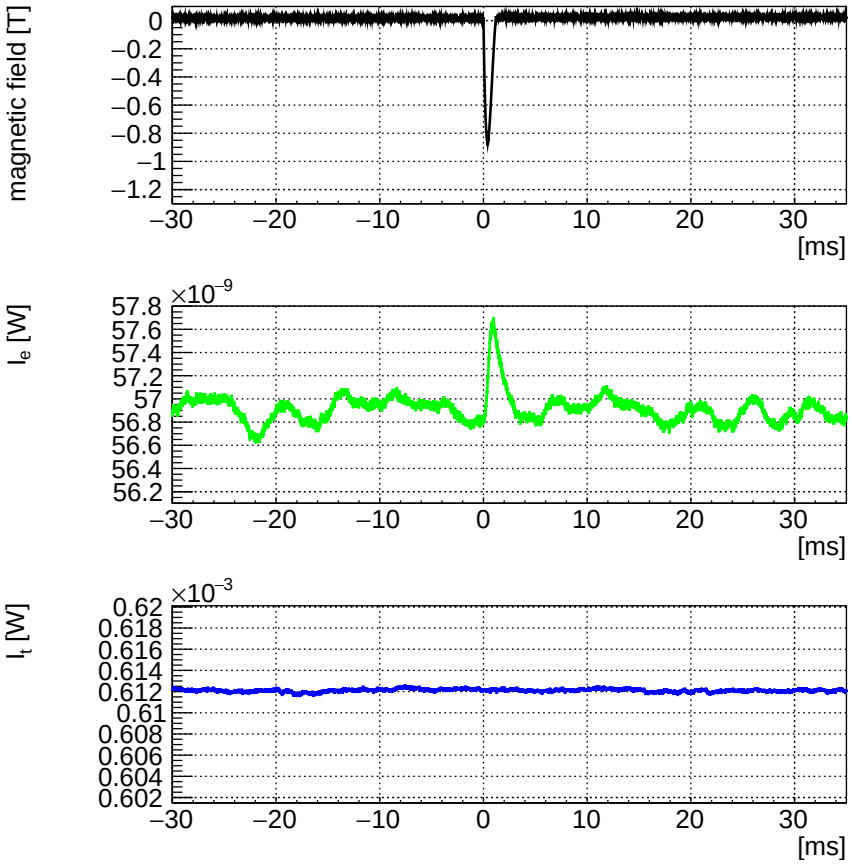

Figure 4.8: An example of the measured data of validation run. Top: magnetic field. middle: I_e. Bottom: I_t.

4.3.2 Parameter estimation

$k_{CM}^{N^2}$ is estimated from the acquired data as discussed in the previous section. Figure 4.9 show an examples of parameter estimation. The black line is the sign averaged ellipticity which is calculated from 1st and 2nd data. The red line is the estimated signal. The estimated signal can explain the measured ellipticity well. The DC level of the estimated signal is decided from the ellipticity just before applying the magnetic field. From this estimation, $k_{\mathrm{CM}}^{\mathrm{N_2}}$ is calculated from Eq. 4.8. It should be noted that as sign of Γ can not be decided, the obtained value is the absolute value of $k_{\mathrm{CM}}^{\mathrm{N_2}}$.

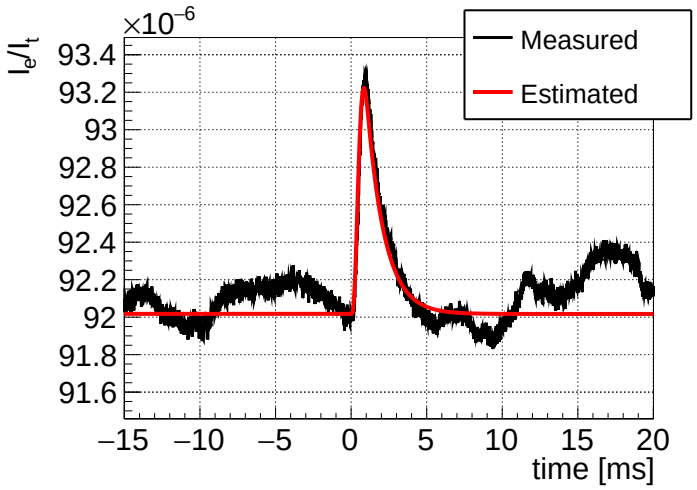

Figure 4.9: An example of the parameter estimation.Black line: Measured sign averaged ellipticity. Red line: Estimated signal.

Figure 4.10 show the distribution of 100 cycles $k_{CM}^{N^2}$ measured at 1 kPa. The distribution is fitted by Gaussian. From the fitting result, the mean value and its error of $k_{\mathrm{CM}}^{\mathrm{N_2}}$ is obtained. The measured $k_{CM}^{N^2}$ at 1 kPa is

$$|k_{\mathrm{CM}}^{\mathrm{N^2}}| = (2.241 \pm 0.007) \times 10^{-15}\ [\mathrm{T^2}]. \tag{4.9}$$

The systematic uncertainty is not included here.

4.3.3 Measurement of the pressure dependence

As the CM effect depends on the gas pressure, the pressure dependence is also measured. Figure 4.11 shows its result. For each point, the uncertainties of the x-axis is the accuracy of the absolute pressure gauge (0.2%) and drift of the measured pressure (1 Pa). The uncertainties of the y axis are the statistic uncertainty and

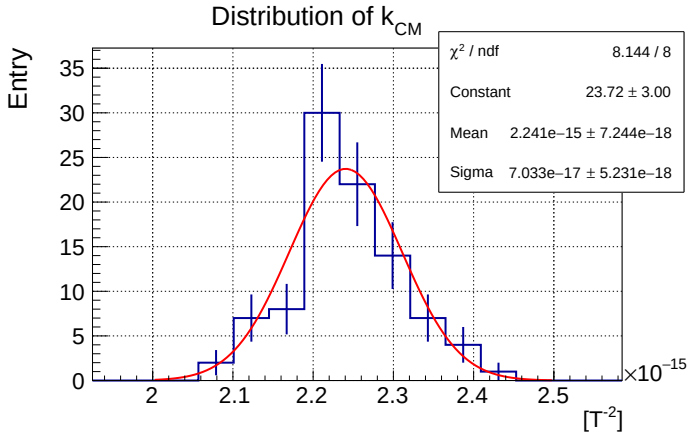

Figure 4.10: Distribution of $k_{\mathrm{CM}}^{\mathrm{N_2}}$ measured at 1 kPa. The distribution is fitted by Gaussian. From the fitting result, the mean value and its error of $k_{\mathrm{CM}}^{\mathrm{N_2}}$ is obtained.

uncertainty of the finesse (0.8%). By fitting measured pressure dependence with linear function and from its slope, $k_{\mathrm{CM}}^{N^2}$ of nitrogen at unit pressure is obtained as

$$|k_{\mathrm{CM}}^{\mathrm{N_2}}| = (2.16 \pm 0.05) \times 10^{-18}\ [\mathrm{T^{-2}Pa^{-1}}]. \tag{4.10}$$

The uncertainty is the statistic uncertainty. The systematic uncertainties are discussed in next section.

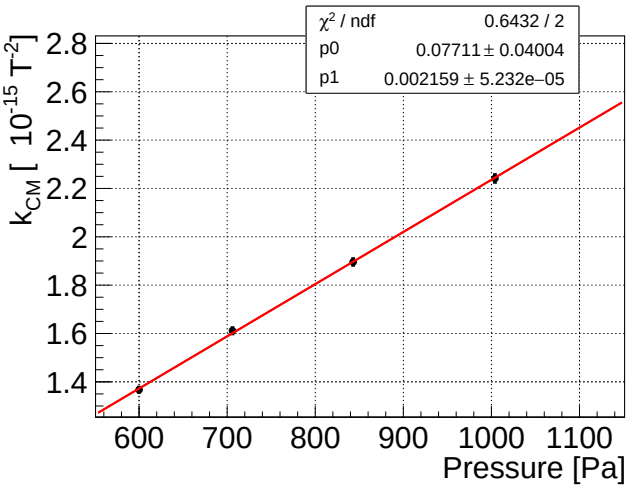

Figure 4.11: Pressure dependence of $k_{\mathrm{CM}}^{\mathrm{N_2}}$. The black dot: Measured $k_{\mathrm{CM}}^{\mathrm{N_2}}$ at each pressure. Red line: Result of the fitting.

4.3.4 Systematic uncertainties

Finesse

The systematic uncertainty of finesse comes from the uncertainty of the cavity length. Measured length between 2 mirrors is 1.35 ± 0.04 m. The systematic uncertainty of finesse is calculated to be 3%.

Attenuation factor

The attenuation factor is calculated from measurement of α. The uncertainty of the estimation of α is typically 2%. Thus, the systematic uncertainty of the attenuation factor is 2%.

Photo detector

The calibration of the photo diodes are performed by the power meter PM160. From its accuracy, the systematic uncertainty of gain of the photo diodes are 3 %.

Relative angle between polarizer and magnetic field

The misalignment of the polarization angle of the polarizer from 45° changes the ellipticity as follows,

$$\sin(2(\frac{\pi}{4} - \Delta\theta)) \sim \cos(2\Delta\theta) \tag{4.11}$$

The relative angle between input polarizer and magnetic field is adjusted by rotating the polarization angle of the polarizer. The angle of the polarizer is adjusted to be 45° against the optical bench. This adjustment is performed by using the scale on the polarizer mount whose interval is 2.5°. The magnet is fixed to the magnet bench and its parallelism against the optical bench is ±1.5° considering the adjustment range of the adjuster of the magnet bench. The accuracy of this adjustment is assumed to be 4°. From this assumption, the systematic uncertainty is calculated to be 1%.

Current transformer

The specified accuracy of the current transformer (CWT-MiniHF400) is 2 %. As the sensitivity is proportional to square of magnetic field, the uncertainties due to the current transformer is calculated to be 4 %.

Field efficiency

To estimate the accuracy of the field efficiency, the field efficiency is measured 10 times at the center of the magnet. From the variation of measured field efficiency, the uncertainties of the field efficiency is estimated to be 0.4 %. As the sensitivity is proportional to square of the magnetic field, the contribution to this uncertainty to the uncertainty of k_{CM} is 0.8 %.

Field length

From the definition of the field length, the uncertainty of the field length

comes from the uncertainty of field efficiency discussed above and the accuracy of the position of the pick-up coil in the beam pipe. The accuracy of the position measurement is assumed to be 1 mm. From this discussion, the uncertainty of field length is calculated to be 1%.

Position of beam path

As the magnetic field profile is not uniform in the transverse direction along the beam pipe, magnetic field depends on the beam path whereas the field efficiency is measured at the center of the beam path. Although, Until now, it is assumed that the beam path coincides with the center of the beam pipe, they can be different each other during the data acquisition.

To estimate the contribution of this uncertainty, the transverse field map is calculated by ANSYS. Figure 4.12 shows the result of the simulation. The boxes are Cu-wire of the coils whose height is 3.0 [mm] and width is 1.0 [mm]. The center of the figure corresponding to the center of the beam pipe whose inner diameter is 5.35 [mm].

The possible position of the beam center is estimated to be as follows. When beam is close to the surface of the beam pipe, the beam acquires additional loss due to the interruption of beam by the beam pipe. Finesse of a Fabry-Pérot cavity including loss is expressed as

$$F = \frac{\pi}{1 - R + P_{\text{loss}}}, \tag{4.12}$$

where P_{loss} is power loss between 2 mirrors. From this expression, to obtain $F \sim 500,000$, the loss should be sufficiently smaller than 6 ppm. The power loss of the beam by the surface of the beam pipe is estimated to be

$$P_{\text{loss}} = \exp\left(-\frac{2r^2}{\omega^2}\right), \tag{4.13}$$

where r is the distance from the center of beam to the surface of the beam pipe and ω is beam radius. From these equations, the minimum distance from beam center to the surface of the beam pipe is calculated to be 1.6 [mm] whereas the radius of the beam pipe is 2.67 [mm]. Thus, the position of the beam center is located within ± 1 [mm] from the center of the beam pipe.

From the simulation performed above, the position dependence of the magnetic field compared to the center of the beam pipe within this region is $+1.1$ % and -1.0 %. The contribution of this position dependence to the uncertainty of k_{CM} is $+2.2$ % and -2.0 %.

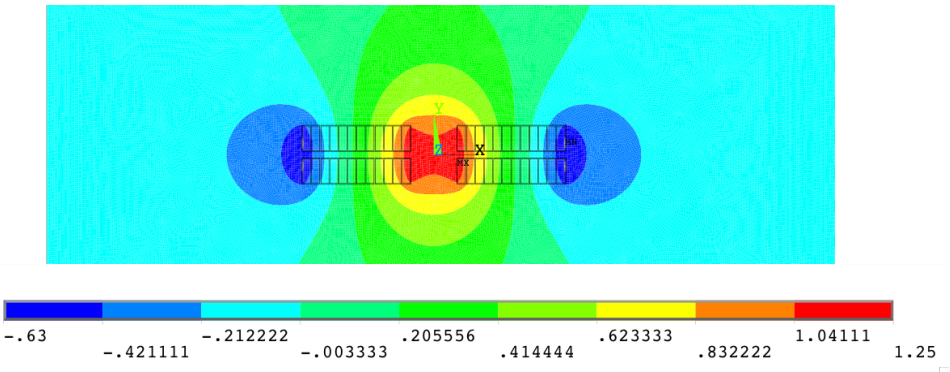

Figure 4.12: The field map [T/kA] of the transverse direction along the beam path (simulation). The boxes are the cu-wire. In the center region (red) has a good uniformity.

Table 4.3: Summary of systematic uncertainties.

parameter	value
Finesse	3%
Attenuation factor	2%
Gain of photo diodes	3%
polarization angle	2%
Current transformer	4%
Field efficiency	1%
Field length	1 %
Alignment of beam pipe	+2.2%, -2.0%
Total	7.6 %

4.3.5 Comparison with previous experiment

$k_{\mathrm{CM}}^{\mathrm{N_2}}$ is measured by other groups with the same wavelength and at the room temperature. Table 4.4 shows the summary of the previous measurement. The obtained result in this measurement is consistent with the previous result within their uncertainty.

Table 4.4: Comparison of $k_{\mathrm{CM}}^{\mathrm{N_2}}$ measured by various experiments.

Ref.	$\lvert k_{\mathrm{CM}}^{\mathrm{N_2}} \rvert \times 10^{18}$
[55]	2.50 ± 0.11
[56]	2.17 ± 0.21
[46]	$2.02 \pm 0.16 \pm 0.08$
[49]	$2.00 \pm 0.08 \pm 0.06$
This result	$2.16 \pm 0.05 \pm 0.16$

4.3.6 Mirror Rotation dependence

To check that the observed signal is a cross term between birefringence of the mirror and Cotton-Mouton effect, the rotational alignment dependence of Cotton-Mouton effect is also measured.

Cotton-Mouton effect is measured at difference rotation alignment of the mirrors including the local minimum of the static ellipticity. For each point, the pulsed magnet is operated 10 cycles. Mirrors are rotated clockwise before each measurement to tune the static polarization change of a Fabry-Pérot cavity. Figure 4.13 shows the measured static ellipticity before each measurement.

Figure 4.14 shows the average of the measured ellipticity at each rotational alignment. Each waveform is the average of 10 cycles data and mean value is subtracted for comparison. The Number in the caption corresponding to the run number in Fig. 4.13. The size of measured ellpticity due to Cotton-Mouton effect depends on the rotational alignment of the mirrors. Before and after the local minimum of the static ellipticity (cyan line), the sign of the polarization change is reversed. This can be understood as the sign of Γ changes by rotating the mirrors. Figure 4.15 show the waveform of $\frac{|I_e|}{|I_t\Gamma|}$ except for the that of the local minimum of the static ellipticity. This value should not depend on the rotational alignment of mirrors. As expected, all waveforms in figure 4.15 agree each other.

From these measurements, it is confirmed that the measured ellipticity depends on the rotational alignment of the mirrors as expected.

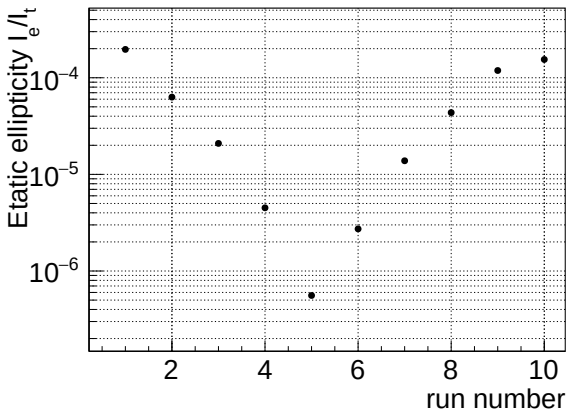

Figure 4.13: Static ellipticity for each measurement. For each measurement, data are acquired for 10 cycles. Mirrors are rotated clockwise to tune static ellipticity before each measurement.

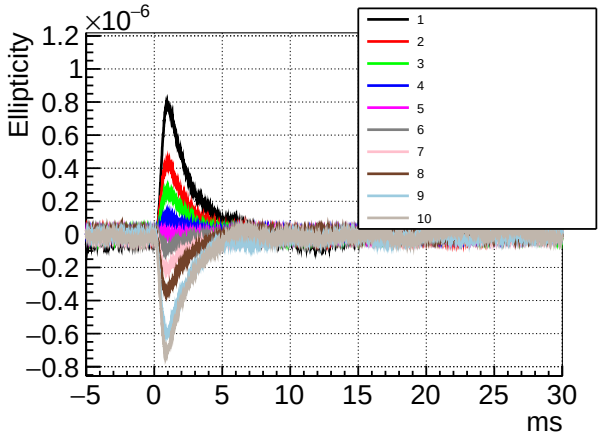

Figure 4.14: Cotton-Mouton effect at different rotational alignment. The number in the caption corresponding to the run number in figure 4.13. The waveforms are average of 10 cycles and its DC value is subtracted for comparison.

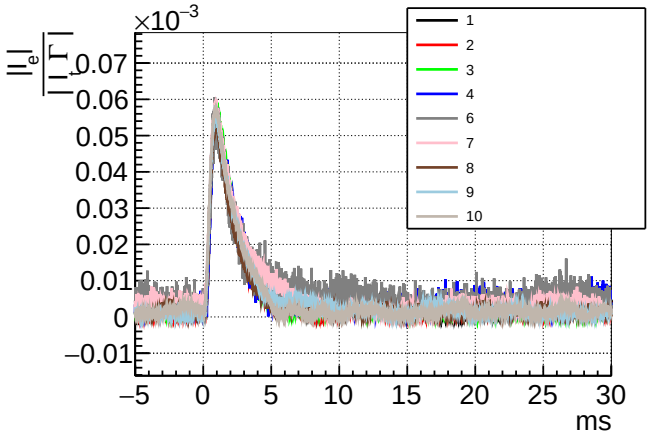

Figure 4.15: Cotton-Mouton effect at different rotational alignment normalized by Γ. All waveforms agree each other as expected.

4.3.7 Conclusion of the validation run

From the measurement of the CM effect of nitrogen gas, it is shown that $k_{\mathrm{CM}}^{N_2}$ can be measured consistently with the previous result within its uncertainty. From this result, it can be concluded that the system and analysis procedure can detect the signal of the CM effect which has the same magnetic field dependence properly, thus this system has the potential to detect VMB.

It is also shown that the sign of the static polarization change of the mirrors can be reversed by rotating mirror and the signal is proportional to the sign of the static polarization change of the mirrors. This property is used in the VMB measurement to cancel the systematic effect which is independent of the static polarization of the mirrors.

4.4 Vacuum run

4.4.1 Summary of the measurement

After the validation run, the measurement of VMB has performed. The single racetrack magnet is used for this measurement. The mirror chambers and the magnet are evacuated to vacuum. The magnet is cooled down to liquid nitrogen temperature. The typical parameters during this measurement are summarized in table 4.5.

During the measurement, the data set are divided for every $\sim$ 100 cycles depending of the timing of the serving of the liquid nitrogen, alignment of the mirrors or intervals of the measurement. For each data set, the power spectrum of the third data is averaged and used as $S(f)$ for the data set. During the run, the resonance of the cavity is lost during the pulse field is generated, or even when the resonance of the cavity is not lost, the large decrease of the internal power of the cavity is observed during the pulse field is generated. These effect is assumed to be due to the electromagnet noise from the magnet system. These events are not used for the analysis. 4% of the total acquired data is discarded and not used for the analysis.

During the measurement, the mirrors are rotated to flip the sign of the static birefringence of the mirrors while keeping the absolute of Γ same. When the sign of Γ is reversed, the sign of the VMB signal appears in the opposite direction. As the absolute sign of Γ is not measured during the run, the sign of Γ during B-1 and B-2 run are defined as positive, and k_{cm} is calculated as follows,

$$k_{\mathrm{CM}}(+) = \frac{\lambda}{4FL_{\mathrm{B}}|\Gamma|\kappa^2}\eta. \tag{4.14}$$

The sign of γ during C-1 and C-2 is defined as negative, and k_{cm} is calculated as follows,

$$k_{\mathrm{CM}}(-) = -1 \times \frac{\lambda}{4FL_{\mathrm{B}}|\Gamma|\kappa^2}\eta. \tag{4.15}$$

Finally, k_{CM} averaging the reversed sign of Γ is calculated as

$$k_{\mathrm{CM}} = \frac{k_{\mathrm{CM}}(+) + k_{\mathrm{CM}}(-)}{2}. \tag{4.16}$$

. The aim of this averaging is the cancellation of the systematic effects which do not depend on the sign of Γ. Figure 4.16 shows the example of 1st data. At t=0, the magnetic field is applied. The applied magnet field is strongest among all VMB experiments. No large destabilization of the locking can be seen after the magnetic field. This is because of the strong feedback system and isolation of acoustic and mechanical disturbances.

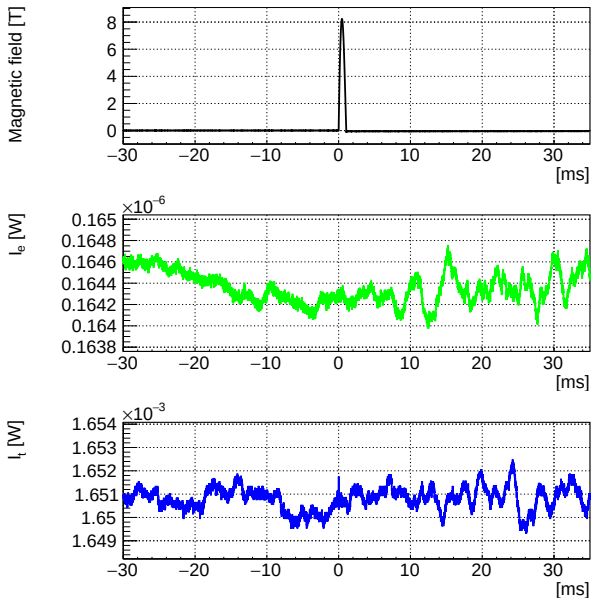

Figure 4.16: Example of the waveform of 1st data in the vacuum run. Top: magnetic field. Middle: I_e. Bottom: I_t.

4.4.2 Cancellation of the noise on I_t

It is found that at the beginning of the pulse, a small and fast intensity noise appears on I_t for every shot. Its appearance becomes clear by averaging I_t. Figure 4.17 shows the example of the waveform of I_t averaged during 50 cycles. Highpass filter whose cutoff frequency is 100 Hz is applied to highlight the fast intensity change. For each cycle, the I_t of the first and second data is averaged with appropriate weight to cancel the effect which is proportional to the magnetic field. The intensity decrease ($\Delta I_t^{\mathrm{spike}}$) is 0.1 % during 100 μs after the pulse. Currently, the origin and the mechanism of the noise is not understood. At least, as this shape appears on I_t, it is not the VMB signal.

Table 4.5: Summary of the typical parameters during vacuum run

parameter	value
Finesse	3.3×10^5
I_t	1.6×10^{-3} [W]
I_e	100 [nW]
$\kappa(\alpha)$	0.98
Peak magnetic field	8.3 [T]
Field length	170 [mm]
Pressure	10^{-4} [Pa]

As far as this noise is generated inside the Fabry-Pérot cavity due to the frequency noise, its effect also appears on I_e. The transfer function from I_t to I_e is a function of the finesse and α, and it becomes a first-order lowpass filter whose cut-off frequency is equals to the cavity pole when $\alpha = 0$ as discussed in B.2. Therefore, Its effect can be canceled by dividing I_e with I_t filtered by the cavity response. However, when the noise appears only on I_t, the noise should not be included when calculating ellipticity. Thus, the correct waveform of the ellipticity depends on the origin of the noise on I_t.

To make the result independent on the origin of $\Delta I_t^{\mathrm{spike}}$, the information of the sign of the static birefringence of the mirrors are used. Figure 4.18 shows the distribution of $\Delta I_t^{\mathrm{spike}}$ calculated from the average of every 50 shots during the measurement. The left side of Fig. 4.18 shows the measured $\Delta I_t^{\mathrm{spike}}$ during B-1 and B-2, whereas the right side of Fig. 4.18 shows that of during C-1 and C-2. The size and the sign of the distribution of $\Delta I_t^{\mathrm{spike}}$ is independent of the sign of the static birefringence of mirrors. From these information, independent on the origin of the noise, it appears in the same direction and the same size on ellipticity not depending on the sign of Γ. Therefore, the effect of $\Delta I_t^{\mathrm{spike}}$ is expected to be canceled out in the final result after averaging k_{CM} with different signs of Γ.

4.4.3 Parameter estimation

The parameter estimation is performed as performed during the validation run. The parameter estimation is performed in 2 patterns. One is that assuming the I_t^{spike} is generated inside the Fabry-Pérot cavity, and the other is assuming I_t^{spike} appears only on I_t.

Firstly, the analysis is performed assuming that the noise on I_t is generated inside the Fabry-Pérot cavity. In this case, the corresponding noise should appear on I_e, thus I_e is divided by I_t filtered by the cavity response.

Figure 4.19 shows an examples of parameter estimation. As the intensity noise at 50 Hz is dominant in the time series, all the wavefrom including the signal shape is drawn after applying bandstop filter whose central frequency is 50 Hz to make

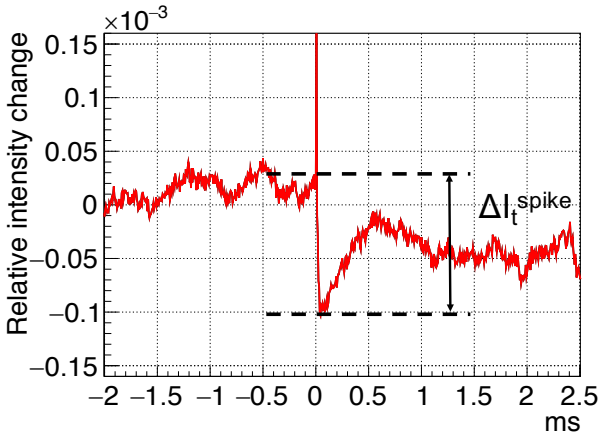

Figure 4.17: Example of the noise on I_t. The waveform is average of the 50 cycle of I_t (100 shots) after the cancellation of the effect proportional to the magnetic field. At $t = 0$, the magnetic field is generated. The sudden change of the output intensity ($\sim 0.01\%$) is observed at the same time with the beginning of the magnetic field.

it easier to compare the waveforms. The black line is the sign averaged ellipticity. The red line is the estimated signal. Again, the mean value of the estimated signal is decided from the ellipticity just before applying the magnetic field.

The left side of Fig. 4.20 shows the distribution of k_{CM} measured during B-1 and B-2, and the right side of Fig. 4.20 shows the distribution of k_{CM} measured during C-1 and C-2. Total 12855 cycles are used for the parameter estimation. Its breakdown is 6007 cycles for positive Γ and 6848 cycles for negative Γ. The distribution is fitted by Gaussian. The result of the fitting is shown in each figure. The p-value for each fitting indicates the reasonable values. Thus, it is good assumption that $k_{\rm CM}$ during all the run distributes obeying on the normal distribution. From the fitting result, the mean value and its error of $k_{\rm CM}$ is obtained for each histograms. $k_{\rm CM}$ after the averaging the sign of Γ is calculated from Eq. 4.16, and the obtained $k_{\rm CM}$ is

$$k_{\rm CM} = (2.6 \pm 5.4) \times 10^{-21}\ [\mathrm{T}^{-2}]. \tag{4.17}$$

The result is consistent with 0 within its uncertainty. The statistical uncertainty for one cycle can be calculated from the result by using the total event as

$$\Delta k_{\rm CM}^{\rm cycle} = 5.4 \times 10^{-21} \times \sqrt{12855} \sim 6 \times 10^{-19}. \tag{4.18}$$

The ideal sensitivity calculated from the noise spectrum and the magnetic field is 5.7×10^{-19}. Although the obtained sensitivity is slightly larger than the ideal sensitivity (5 %), the value is almost identical. Thus, it can be concluded the

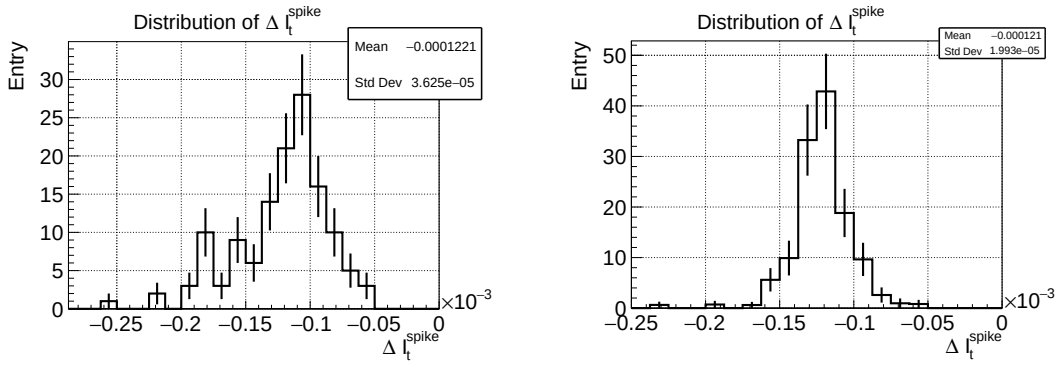

Figure 4.18: Distribution of I_t^{spike} calculated from the average of every 50 cycles. Left: I_t^{spike} obtained during B-1 and B-2. Right: I_t^{spike} obtained during C-1 and C-2. The size and sign of the noise is not depends on the sign of Γ. Therefore, its effect is expected to be canceled not depending of the origin of this noise.

sensitivity is mainly limited by the intrinsic birefringence noise not depending on the magnetic field as expected.

To show the effect of the noise on I_t does not affect the sensitivity, the same analysis is performed assuming that the noise is appears only on I_t. In this assumption, the mean value of I_t is used to calculate the ellipticity as the corresponding noise does not appears on I_e. Figure 4.21 shows the distribution of k_{CM} during B-1 and B-2 (left) and k_{CM} during C-1 and C-2 (right). Again, each histogram is fitted by Gaussian, and p-value is reasonable in this analysis again. k_{CM} after the averaging the sign of Γ is calculated from Eq. 4.16, and the obtained k_{CM} is

$$k_{\mathrm{CM}} = (5.8 \pm 5.5) \times 10^{-21}\ [\mathrm{T}^{-2}]. \tag{4.19}$$

Though the result is slightly different from the previous analysis (0.6 σ), the results are consistent with each other not depending on the assumption of the noise origin of I_t. The difference of the central value is included to the systematic uncertainty .

4.4.4 Systematic uncertainties

Table 4.7 shows a summary of the systematic uncertainties during the vacuum run. The uncertainties which are in common with the validation run is not discussed here. (See section 4.3.4.)

Position of beam path

As the difference magnet is used than the validation run, the systematic uncertainty related to the magnet should be discussed. The uncertainty due to the position of the beam path is evaluated in the same way as discussed in the validation run. In this case, however, as the beam path is not parallel

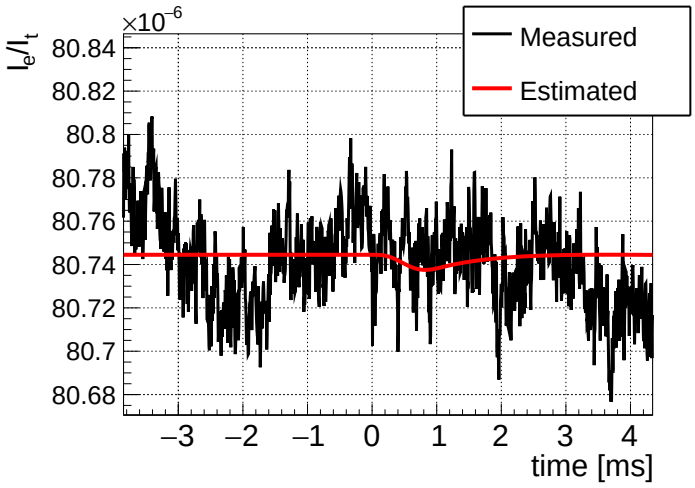

Figure 4.19: Example of the result of the parameter estimation. Black line: averaged ellipticity. Red line: Estimated signal

to the coil, not only the field efficiency but also the field map changes at the same time depending on the position of the beam path.

Figure 4.22 shows the field map calculated by ANSYS at the center of the beam pipe and at the beam path where the B^2L becomes smallest within ± 1 [mm] from the center of the beam path. By comparing these 2 field maps, the uncertainty from the beam position is calculated to be 6.4%.

Effect of the noise on I_t

As discussed above, the analysis procedure depends on the origin of the noise on I_t. In this work, different analysis is performed assuming that the noise on I_t is generated inside the Fabry-Pérot cavity or the noise appears only on I_t. The difference of the center value of each analysis is 0.65 σ against the static uncertainty of the parameter estimation. This difference is used as the systematic uncertainty of the analysis procedure.

Effect of the asymmetry of Γ

Although the birefringence signal depends only on the sign of Γ, the size of the non-birefringence noise depends on the absolute of Γ. The example of the Γ dependence of the noise is summarized in Table 4.6. Basically, all of the noises should depends on $|\Gamma|$ or $|\Gamma|^{-1}$. Thus, the cancellation of the non birefringence noise depends on the asymmetry of Γ between each run and the noise source of the systematic effect.

To discuss the effect of the asymmetry of Γ, the mean values of Γ are calculated from the distribution of Γ for each run. The mean value of $|\Gamma|$ of

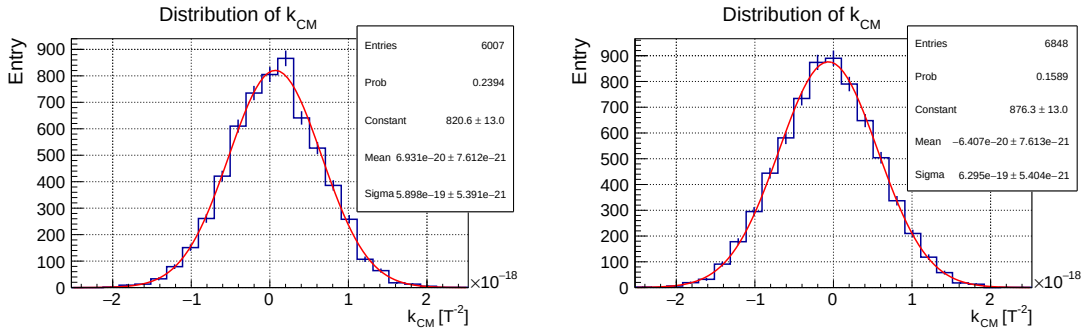

Figure 4.20: Distribution of k_{CM} assuming the noise on I_t is generated inside the Fabry-Pérot cavity. Left: k_{CM} obtained during B-1 and B-2. Right: k_{CM} obtained during C-1 and C-2. Each distribution is fitted by Gaussian. From the fitting result, the mean value and its error of k_{CM} is obtained.

positive Γ and negative Γ is

$$\langle\,|\,\Gamma(+)\,|\,\rangle \quad = 6.08 \times 10^{-3} \tag{4.20}$$
$$\langle\,|\,\Gamma(-)\,|\,\rangle \quad = 7.14 \times 10^{-3}, \tag{4.21}$$

where the standard error of each mean value is 0.2 % and 0.1% respectively. Therefore, the asymmetry of about 16% exists between two measurement. Currently, the dominant noise source of the non birefringence noise during the measurement is not understood. Thus, the effect of this asymmetry is evaluated as follows.

When it is assumed that the dominant noise source depends on $|\Gamma|$, the average of k_{CM} should be calculated as follows instead of Eq. 4.16,

$$k_{\mathrm{CM}}^{\Gamma} \equiv \frac{\langle\,|\,\Gamma(-)\,|\,\rangle\, k_{\mathrm{CM}}(+) + \langle\,|\,\Gamma(+)\,|\,\rangle\, k_{\mathrm{CM}}(-)}{\langle\,|\,\Gamma(+)\,|\,\rangle + \langle\,|\,\Gamma(-)\,|\,\rangle} \tag{4.22}$$

On the other hand, when it is assumed that the dominant noise source depends on $|\Gamma|^{-1}$, the average of k_{CM} should be calculated as follows,

$$k_{\mathrm{CM}}^{\Gamma^{-1}} \equiv \frac{\langle\,|\,\Gamma(-)\,|^{-1}\rangle\, k_{\mathrm{CM}}(+) + \langle\,|\,\Gamma(+)\,|^{-1}\rangle\, k_{\mathrm{CM}}(-)}{\langle\,|\,\Gamma(+)\,|^{-1}\rangle + \langle\,|\,\Gamma(-)\,|^{-1}\rangle}. \tag{4.23}$$

The k_{CM} is calculated to be as follows from the measured asymmetry of Γ,

$$k_{\mathrm{CM}}^{\Gamma} \quad = 7.4 \pm 10^{-21}\ [\mathrm{T}^{-2}] \tag{4.24}$$
$$k_{\mathrm{CM}}^{\Gamma^{-1}} \quad = -3.3 \pm 10^{-21}\ [\mathrm{T}^{-2}] \tag{4.25}$$

Depending on the assumption of the origin of the non-birefringence noise, the central value of k_{CM} varies $\sim 0.9\sigma$ compared to the result obtained in

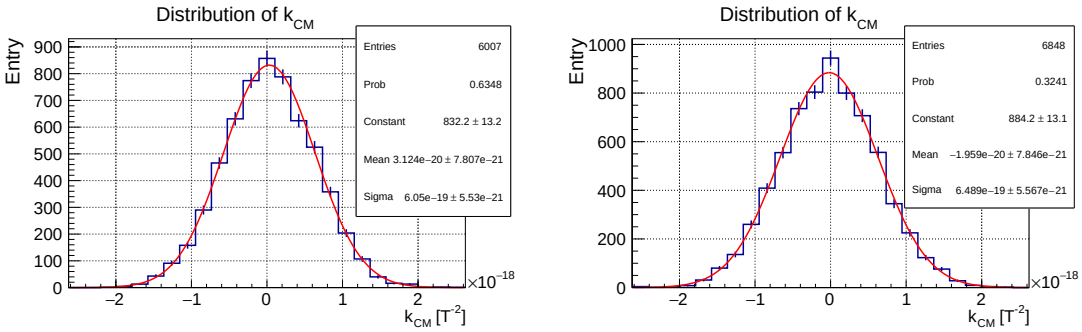

Figure 4.21: Distribution of k_{CM} assuming the noise on I_t appears on $I_t only$. Left: k_{CM} obtained during B-1 and B-2. Right: k_{CM} obtained during C-1 and C-2. Each distribution is fitted by Gaussian. From the fitting result, the mean value and its error of k_{CM} is obtained.

Table 4.6: Example of the Γ dependence of the noise sources against the birefringence signal

parameter	Γ dependence
Intensity noise	$\lvert\Gamma\rvert$
Frequency noise	$\lvert\Gamma\rvert$
Polarization rotation	$\lvert\Gamma^{-1}\rvert$
Scattering or stray light	$\lvert\Gamma^{-1}\rvert$ or $\lvert\Gamma\rvert$
Electromagnetic noise on $\mathrm{PD_t}$	$\lvert\Gamma\rvert$
Electromagnetic noise on $\mathrm{PD_e}$	$\lvert\Gamma^{-1}\rvert$

Eq. 4.17. This uncertainty of the average of k_{CM} is included to the systematic uncertainty due to the asymmetry of Γ, and it is assumed that the true k_{CM} uniformly distribute within this uncertainty.

4.5 Result

The following result is obtained from the analysis described in this chapter. As the relative sign of k_{CM} can not be decided, the limit is obtained for the absolute value of k_{CM}

$$|k_{\mathrm{CM}}| < 1.8 \times 10^{-20} \text{ (95\% C.L.)} \tag{4.26}$$

The comparison with the previous experiment in discussed in the next section.

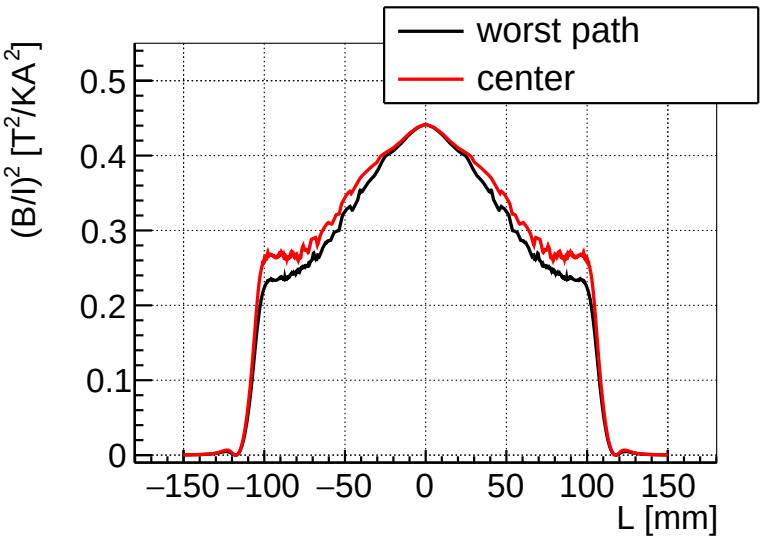

Figure 4.22: Beam path dependence of the field map. Red: the field map at the center of the beam pipe. Black: the field map when $B^2 \times L$ becomes smallest within ± 1 [mm] from center.

Table 4.7: Summary of the systematic uncertainties.

parameter	value
Finesse	3%
Attenuation factor	2 %
Gain of photo diodes	3 %
polarization angle	2 %
Current transformer	4 %
Field efficiency	4.1 %
Field length	1 %
Alignment of beam pipe	6.4%
Analysis procedure	$+3.2 \times 10^{-21}$ [T^{-2}]
Asymmetry of Γ	$+4.9 \times 10^{-21}$ [T^{-2}], -5.8×10^{-21} [T^{-2}]

Chapter 5

Discussion and prospect

In the first section of this Chapter, the limit obtained in the previous chapter is compared with the other limits. In the next section, upgrades for future experiment are described.

5.1 Discussion of the experimental result

5.1.1 Significance of this work

As discussed in the previous chapter, the obtained sensitivity is almost identical to the expected sensitivity. Thus, it can be concluded that the experimental setup emphasizing on the reduction of the disturbance and analysis procedure works as expected. It is succeeded to search for the VMB signal at higher frequency region where intrinsic noise of the optical system is smaller by taking the advantage of the pulsed magnet. At the same time, it has also succeeded the operation of the pulsed magnet with the optical system during one month. No sign of the destruction can be observed at the pulsed magnet throughout and after the measurement, this work demonstrate the feasibility of the long term operation of the pulsed magnet.

5.1.2 Comparison with previous experiment

Figure 5.1 shows the limit of $|k_{\mathrm{CM}}|$ obtained for this work and previous experiment, and Table 5.1 shows a summary of the comparison with the previous experiment.

Compared with the previous experiment, the strongest the magnetic field has applied inside the Fabry-Pérot cavity in this experiment. Compared to the previous VMB search with pulsed magnet, the obtained statistic is more than 100 times larger. This is due to the successful establishment of the stable operation of the Fabry-Pérot cavity with the high repetitive pulsed magnet.

Though the system works as expected, the obtained sensitivity is not reached the sensitivity obtained by the previous experiment. The difference between the world record sensitivity obtained by PVLAS can be explained well by the difference of the parameter in Table 5.1. The difference mainly comes from the size of the

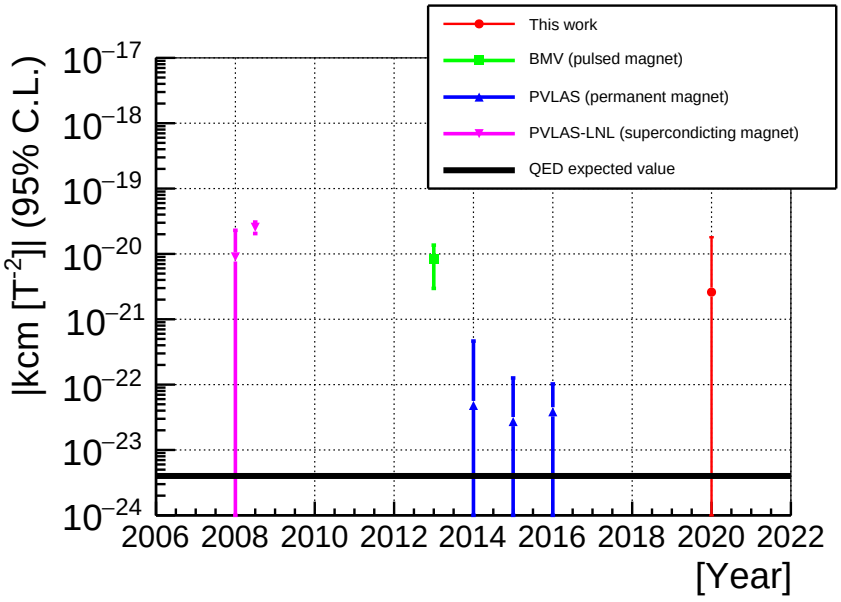

Figure 5.1: Limit on $|k_{\mathrm{CM}}|$ obtained by this work and previous experiments. The values derives from the following references: BMV [38], PVLAS [35].

magnet and statistic. Figure 5.2 shows the limit to ALPs obtained for this work and previous experiments. Though the obtained limit is not better than the limit obtained by PVLAS, the sensitivity is already better than other type of ALPs search experiments around 0.01 to 0.1 eV.

5.2 Upgrade for future experiment

Based on the discussion in the previous section, the upgrade plan for the future experiment is discussed in this section.

The factors which are related to the sensitivity can be classified as follow,

- Peak magnetic field
- Field length
- Repetition rate
- Reduction of the systematic
- Reduction of the birefringence noise

Table 5.1: Summary of the experimental parameter

parameter	PVLAS	BMV	this result
Type of the Magnet	DC	pulse	pulse
B^2_{eff} [T^2]	6.5	20	28
Field length [m]	1.6	0.137	0.17
statistics	60 days	0.3 s (100 pulses)	40 s (10^4 pulses)
Noise level [m/$\sqrt{\mathrm{Hz}}$]	6×10^{-19}	$\sim 1 \times 10^{-19}$	$\sim 1 \times 10^{-19}$
Obtained sensitivity	2.7×10^{-23}	2.8×10^{-21}	7×10^{-21}

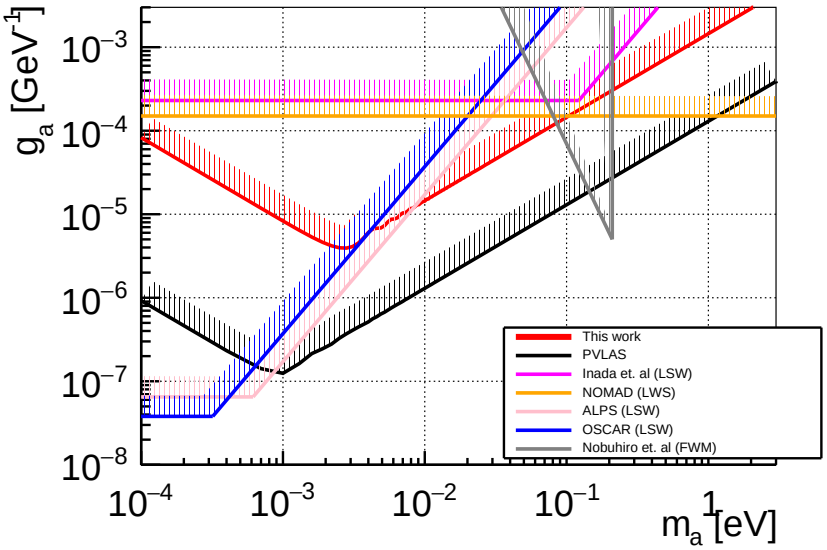

Figure 5.2: Limit on ALPs by this work and previous experiments.

5.2.1 Upgrade of the magnet

The destruction field of the current magnet measured at the center of the beam pipe is 12 T. As the tensile strength of the copper is about 300 MPa, the destruction field of the copper wire in the case of the single wire coil is roughly calculated to be 28 T. At the destruction field of the current magnet, the maximum magnetic field is 15 T at the inner wire of the coil. Thus, the maximum magnetic field is assumed to be not limited by the material properties of the wire but the reinforcement structure. As the destruction occurred at the corner of the coil, it is assumed that the destruction is induced by the insufficient reinforcement at the corner. The 1st step of the upgrade of the magnet is to develop sufficient reinforce structure.

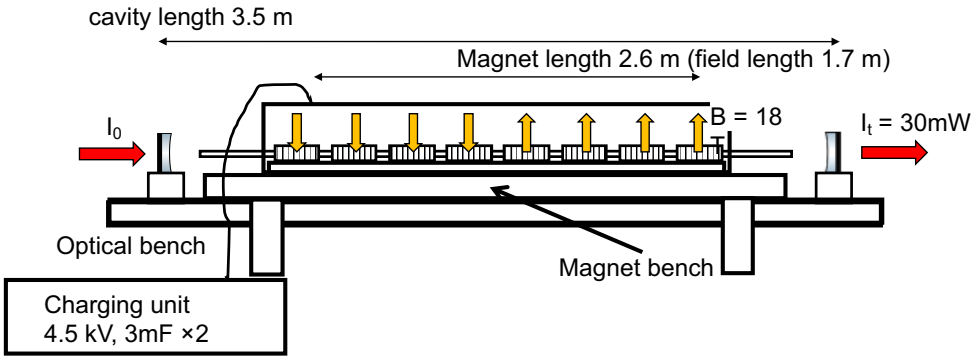

Figure 5.3: Schematic of the setup after the upgrade. Total 8 magnets are operated by 2 capacitor bank, and its peak magnetic field is 18 T.

The improvement of the magnet should include the improvement of the field efficiency. This is because increasing the current leads to higher temperature of the coil, then makes the repetition rate worse. One of the ideas is adopting the dipole structure. From the simulation by ANSYS, the field efficiency becomes 1.8 times larger by keeping the inductance of the coil and the field length the same. This design gives 3.4 times better sensitivity per pulse with the same operation parameter of the capacitor bank.

5.2.2 Upgrade of the field length

The improvement of the field length is also needed for better sensitivity. The field length is limited by the length of the cavity and the stored energy at the capacitor bank. Thus, the improvement of these items is needed for the enhancement of the field length.

The maximum charging energy of the capacitor bank is 30 kJ, where current operating energy is 6 kJ. Therefore, 3 more magnets can be operated with the current capacitor bank. The required cavity length is at least 2.4 m. The pulse width can be kept the same when connecting 4 magnets 2 series and 2 parallel.

The stored energy of the capacitor needed to be increased to operate more magnets or to operate with stronger peak magnetic field. The current capacitor bank has two charging unit, and one of the two is not used during this work. Therefore, 4 more magnets can be operated by installing another capacitor whose capacitance is 3 mF. when using 8 magnets, required minimum cavity length becomes 3.5 m. The cutoff frequency of the Fabry-Pérot cavity becomes 2.5 times higher. The input power to the Fabry-Pérot cavity is needed to be increased 2 times larger to keep the contribution of the shot noise the same.

Another advantage of using multiple magnets is that the magnetic field can be generated in different direction at the same time. When generating the magnetic field in the opposite direction at the same time, the VMB signal is not changed as

it depends on the square of the magnetic field, but the background which depends on the linear of the magnetic field can be canceled for one shot. This leads to the more reduction of the systematic noise.

5.2.3 Improvement of the repetition rate

The thermal constant needed to be reduced to improve the repetition rate. Figure 5.4 show the cross section of the single coil racetrack magnet and the thermal resistance of each material is described. The thermal constant is determined from the heat capacity of the coil and thermal resistance of the backup and insulating materials. The heat capacitance can not be reduced as far as using the same structure of the coil. The kapton film is necessary for insulation of the coil. Therefore, the reduction of the thermal resistance of the glass epoxy (0.081 k/W) or the stainless back up (0.07K/W) is required to improve the thermal constant.

The glass epoxy is used for the safety, thus it can be removed totally as the kapton film has enough electric breakdown voltage. It occupies 40% of total thermal resistance. It is not straightforward to estimate the possible reduction of the stainless backup as it also affects the destruction of the coil. The basic idea is to make the thickness along y-axis thin where Maxwell stress is not strong, and make holes in the backup. By these upgrades, it is aimed to reduce the thermal resistance half times smaller. The repetition rate becomes half times smaller due to this upgrade.

After the upgrade of the capacitor bank, there are still room to generate 20% larger magnetic field for each magnet. This leads to 40% better sensitivity for each shot. From the numerical calculation, the increase of the flowing current 20% larger results in the increase of the temperature of the coil 30 K higher than current setup. After all, the repetition rate could be reduced to 13 s/pulse from 18 s/pulse.

5.2.4 Gain on k_{CM} from the upgrade of the magnet system

Finally, the possible improvement of the sensitivity by the upgrade of the magnet system is summarized in 5.2. The sensitivity per pulse can be calculated assuming the birefringence noise level is the same as follows,

$$\Delta k_{\mathrm{CM}} = 9.2 \times 10^{-21}\ [\mathrm{T}^{-2}/\mathrm{pulse}]. \tag{5.1}$$

This can be interpreted as the sensitivity per second as

$$\Delta k_{\mathrm{CM}} = 3.4 \times 10^{-20}\ [\mathrm{T}^{-2}/\sqrt{\mathrm{Hz}}]. \tag{5.2}$$

This sensitivity is 2 times better than the obtained sensitivity by PVLAS.

5.2.5 Upgrade of a Fabry-Pérot cavity

From the study of the intrinsic birefringence noise of the Fabry-Pérot cavity, it is found that the unexpected birefringence noise limits the sensitivity. To upgrade

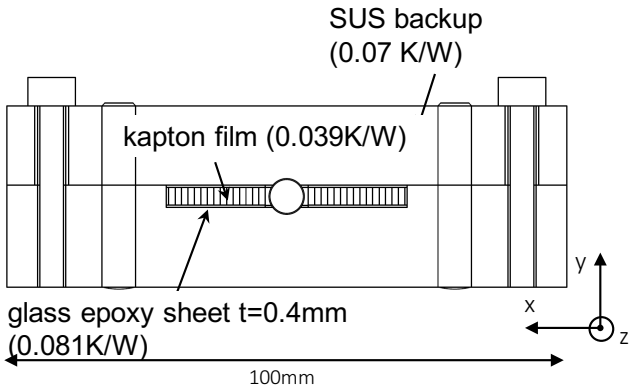

Figure 5.4: Cross section of the magnet. The heat resistance of each material is noted.

Table 5.2: Summary of the gain on k_{CM} by the upgrade of the magnet system. It is assumed that the observed birefringence noise of the Fabry-Pérot cavity is the same after the upgrade.

parameter	current Value	upgrade	gain on k_{CM}
Peak field [T]	8.3	18	4.8
Field length [m]	0.17	1.4	8
Repetition rate [Hz]	0.05	0.075	1.18
Expected sensitivity $[\mathrm{T}^{-2}/\sqrt{\mathrm{Hz}}]$	1.5×10^{-18}	3.4×10^{-20}	46

the sensitivity of a Fabry-Pérot cavity, the understanding of the mechanism of the observed noise excess is necessary. It is assumed that the noise is generated inside a Fabry-Pérot cavity. Therefore, the improvement of finesse has less contribution to the optical pass length sensitivity. In the same way, the increase of the input power to a Fabry-Pérot cavity improves the sensitivity above ∼700 Hz where the signal power is not strong. When the cavity length becomes 3.5 m by the increase of the magnet, the required output power of the ordinary light is 30 mW to make the contribution of the shot noise small enough.

The first step to understand the unexpected birefringence noise further is to identify whether the noise origin is the thermal like noise of the mirror or not. One idea is to study the temperature dependence of the noise. This found to be difficult by previous experiment [35]. Another idea is to study the beam spot size dependence. Generally, the effect of thermal noise of mirrors become small when beam spot size become larger. The study can be achieved building the shorter Fabry-Pérot cavity. For example, the beam spot size becomes 0.5 times smaller when cavity length is 20 cm with the same mirror. Other idea is to study the

material dependence of the coating or the substrate of the mirror to see the material dependence of the noise.

5.2.6 Reduction of the systematic uncertainty

The systematic uncertainty should be also reduced for the future experiment.
The largest systematic uncertainty comes from the uncertainty regarding to the asymmetry of Γ. To reduce this uncertainty, the understanding and the reduction of the non birefringence noise observed in Fig. 4.20 is necessary. Currently, although the origin is not understood, it is assumed that the origin is related to the movement of the beam pipe against the beam path as discussed in 3.5.7. For the investigation of the effect of the beam pipe, the dependence of the size of the noise against the material of the beam pipe or against the radius of the beam pipe should be studied in the future. The property of the noise can be studied by measuring the $|\Gamma|$ dependence of the non birefringence noise as the dependence depends on the origin of the noise as discussed in Chapter 4.4.4.

Another systematic uncertainty comes from the spike noise on I_t which is discussed in Chapter 4.4.2. The origin of the noise can be identified by measuring the I_t by two independent photodetector. When the noise is generated inside the Fabry-Pérot cavity, the same noise is expected to be observed for each detector, whereas no coherence is observed when the noise is generated outside the Fabry-Pérot cavity. The origin of the noise can be also identified by measuring the noise on I_t without the Fabry-Pérot cavity. When noise is generated outside the Fabry-Pérot cavity, the same noise is expected to appear even without the Fabry-Pérot cavity.

5.2.7 Improvement of the analysis procedure

The analysis procedure can be also improved. Currently, the length of the timing window is chosen to be 40 ms. The length is chosen so that the distortion of the Fourier spectrum by the large peak at 50 Hz becomes small and the spectrum has enough frequency resolution to remove the effect of the peak. Instead of that, it is also possible to remove the effect of the peak structures by filtering the waveform with notch filters in time domain before the Fourier transformation. This procedure makes it possible to reduce the length of time window shorter. Although the expected sensitivity does not depend on the length of time windows as far as the signal shape is well-included in the time window, it could be beneficial for the Fourier transformation. Currently, the rectangular window is used as the window function. As the signal is located on the end of the timing window, it is difficult to use another window function which gradually becomes 0 at the beginning and the end of the timing window. When the length of the timing window becomes $\sim$10 ms, the signal located at the center of the timing window. At this situation, other window functions can be applied, which would lead to reduce distortion of the spectrum due to the discontinuity of the waveform.

It could be also possible to suppress the effect of disturbance by analysis procedure. The VMB signal spectrum distributes among the wide frequency region due to its timing profile, whereas the spectrum of the effects of disturbance would have peaks when they are generated by the mechanical resonance of the experimental setup. These peak can be eliminated by applying the band-pass filter before performing the Fourier transformation. It is also possible to suppress these effects by not using these frequencies for the parameter estimation.

Chapter 6

Conclusion

The search for vacuum magnetic birefringence (VMB) has performed using the high repetitive pulsed magnet and the high finesse Fabry-Pérot cavity in this thesis. The experimental setup to operate the Fabry-Pérot cavity and the pulsed magnet has developed. The peak magnetic field is 8.3 T which is the strongest magnetic field as VMB search and field length is 0.17 m.

Dedicated study of the intrinsic noise of the optical system is performed up to 1 kHz. The noise evaluation method with the homodyne detection scheme is established both theoretically and experimentally. The optical pass length sensitivity at signal frequency reaches to 1×10^{-19} m/$\sqrt{\text{Hz}}$ which is 5 times better than the sensitivity at around 10 Hz, which is used in the VMB search with pulsed magnet. This result shows the advantage of the pulsed magnet. However, even in the high frequency, birefringence noise excess is observed, and indicates the existence of the birefringence noise source not depending on the detection scheme or the detail of the experimental setup even at the high frequency region.

The calibration of the system and analysis is performed by measuring the Cotton-Mouton effect of N_2 gas. The obtained result is consistent with the previous experiments.

The search for VMB has performed from 13. Nov. to 10. Dec. Total 26000 pulses are generated during the operation. No significant signal is observed and obtained limit to k_{CM} is

$$|k_{\text{CM}}| < 1.8 \times 10^{-20} \ (95\%\text{C.L.}) \tag{6.1}$$

This experiment demonstrates the feasibility of VMB search with the high repetitive pulsed magnet, especially the stable operation of the Fabry-Pérot cavity with the pulsed magnet and analysis method. With using multiple magnets with stronger field, the improvement of the sensitivity on k_{CM} can be achieved in the future experiment.

Appendix A

Optical cavity and PDH method

Fabry-Pérot cavity is an optical resonator which is composed with 2 high reflective mirrors. Pound-Drever-Hall (PDH) method is a basic method to extract the difference between a resonance frequency of the cavity and frequency of the input laser. The extracted information is used as an error signal for the feedback system to lock the laser frequency to the resonance frequency of the cavity. In this section, firstly the basic properties of Fabry-Pérot cavity is explained. After that, a detection scheme of PDH method is explained.

A.1 Fabry-Pérot cavity

A.1.1 Transmittance and reflectance

A Fabry-Pérot cavity is an optical resonator consists of 2 high reflective mirrors facing each other. Fig. A.1 show a schematics of a Fabry-Pérot cavity. A part of input laser transmitted front mirror. For each reflection, a part of transmitted light is reflected by mirrors and the rest is transmitted from mirrors.

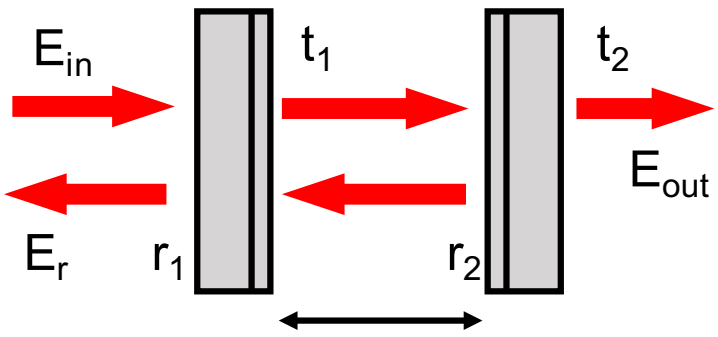

Figure A.1: A schematics of a Fabry-Pérot cavity

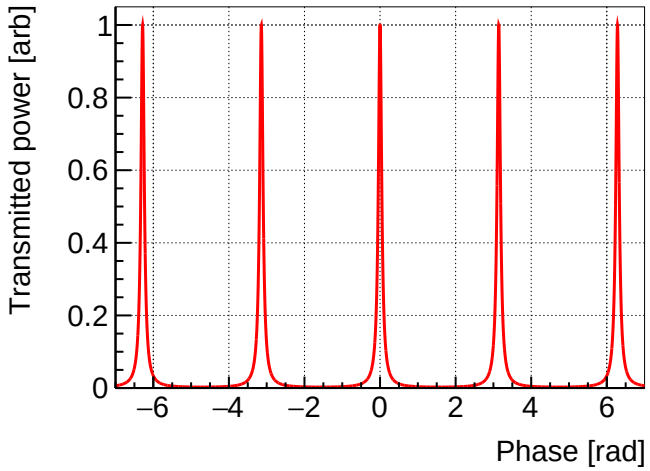

Figure A.2: Example of transmitted power from a Fabry-Pérot cavity as a function of phase ϕ when $r^2 = 0.99$ and $t^2 = 0.01$

The output of a Fabry-Pérot cavity can be written as

$$\begin{aligned} E_{out} &= E_{in} t_1 t_2 \sum_n (r_1 r_2 e^{-2\phi})^n \\ &= E_{in} \frac{t_1 t_2 e^{i\phi}}{1 - r_1 r_2 e^{-2i\phi}}, \end{aligned} \tag{A.1}$$

where $\phi = 2\pi \frac{L}{c} \nu$ is a phase change during traveling along the cavity length. From above expression, the amplitude transmittance and reflectance of a Fabry-Pérot cavity can be defined as follows.

$$t_{FP} = \frac{t_1 t_2 e^{i\phi}}{1 - r_1 r_2 e^{i2\phi}}, \tag{A.2}$$

$$r_{FP} = r_1 - \frac{r_1 t_1 t_2 e^{i2\phi}}{1 - r_1 r_2 e^{i2\phi}}. \tag{A.3}$$

The intensity of transmitted light and reflected light from a Fabry-Pérot cavity can be written as follows,

$$I_t = |t_{FP} E_{in}|^2 = \frac{t_1^2 t_2^2}{(1 - r_1 r_2)^2 (\frac{4 r_1 r_2}{1 + (1 - r_1 r_2)^2} \sin^2(\phi))} |E_{in}|^2, \tag{A.4}$$

$$I_r = |r_{FP} E_{in}|^2 = \frac{((t_1^2 + t_2^2) r_1 - r_2)^2 + 4 r_1 r_2 (r_1^2 r_2^2) \sin^2(\phi)}{(1 - r_1 r_2)^2 (\frac{4 r_1 r_2}{1 + (1 - r_1 r_2)^2} \sin^2(\phi))} |E_{in}|^2. \tag{A.5}$$

Hereafter, let us assume $r_1 = r_2 = r$ and $t_1 = t_2 = t$ for simplicity. As an example of transmitted power from a Fabry-Pérot cavity is shown in Fig. A.2 as a function of ϕ.

A.1.2 Finesse, free spectrum range and photon lifetime

From Eq. (A.4),when $\nu = m \times \frac{c}{2L}$ $(m \in \mathbb{Z})$, the transmittance become maximum. The frequency interval between each maximum $\nu_{FSR} = \frac{c}{2L}$ is called free spectrum range (FSR).

Finesse is defined as the ratio between FSR and FWHM of each resonance curve.

$$Finesse = \frac{\nu_{\mathrm{FSR}}}{\nu_{\mathrm{FWHM}}} = \frac{\pi r}{1 - r^2}. \tag{A.6}$$

Finesse is a index of a sharpness of cavity resonance and its depends on the amplitude reflectance of each mirror.

A photon life time is a decay constant of an internal power of a Fabry-Pérot cavity. Let's assume a steady state Fabry-Pérot cavity and at certain time, the input laser to a Fabry-Pérot cavity is suddenly turned off. For each round trip, the amplitude loss of the light inside a Fabry-Pérot cavity ΔE can be expressed as follows,

$$\Delta E = -(1 - r^2)E_{\mathrm{intra}}. \tag{A.7}$$

where E_{intra} is internal amplitude of a Fabry-Pérot cavity. From this expression, a differential equation about internal amplitude of the light can be derived as follows,

$$\frac{\mathrm{d}E_{\mathrm{intra}}}{\mathrm{d}t} = -\frac{c}{2L}(1 - r^2)E_{\mathrm{intra}}. \tag{A.8}$$

By solving above equation with a initial condition that is $E_{\mathrm{intra}}(t = 0) is E_0$, the time evolution of the amplitude inside the Fabry-Pérot cavity become

$$E_{\mathrm{intra}}(t) = E_0 e^{-\frac{c}{2L}(1-r^2)t}. \tag{A.9}$$

Therefore, the time evolution of the output power from a Fabry-Pérot cavity becomes as follows,

$$I_{\mathrm{out}}(t) = I_{in}(0)e^{-\frac{c}{L}(1-r^2)t}. \tag{A.10}$$

Now, a photon lifetime τ of a Fabry-Pérot cavity is defined as a decay constant of the output power of a Fabry-Pérot cavity.

$$\begin{aligned} \tau &= \frac{L}{c(1 - r^2)} \\ &\sim \frac{FL}{c\pi}. \end{aligned} \tag{A.11}$$

Thus, by measuring the decay constant of a Fabry-Pérot cavity, finesse of a Fabry-Pérot cavity can be calculated. This method is called cavity ringdown method.

A.2 PDH method

From the previous section, the resonance condition of a high finesse Fabry-Pérot cavity is very severe. Suppose input laser frequency is 300 THz, a cavity length is 1 m and finesse is 300,000, the FWHM is corresponding to cavity length fluctuation of 3 pm. It is necessary to obtain the difference between laser frequency and resonance frequency and feedback it to laser frequency or cavity length to keep the resonance condition. PDH method is one of the most basic method to extract the difference.

A.2.1 a basic setup

A basic setup for PDH method is shown in Fig. A.3. An Electric Optical Modulator (EOM) is used to modulate the frequency of input laser. The amplitude after the modulation can be written as follows,

$$\begin{aligned} E_{in} &= E_0 \mathrm{exp}(\mathrm{i}\omega \mathrm{t} + \mathrm{i}\beta \mathrm{sin}(\Omega \mathrm{t})) \\ &\sim E_0 e^{i\omega t}[J_0(\beta) + J_1(\beta)e^{i\Omega t} - J_{-1}e^{-i\Omega t}], \end{aligned} \tag{A.12}$$

where Ω is a modulation frequency by EOM, β is called modulation depth and J_m is Bessel function of m-th order. PDH method uses the reflected light from a cavity to extract the errors signal. As the amplitude reflectivity of a Fabry-Pérot cavity is a function of acquired phase for each trip during the cavity length, the reflectivity depends on the frequency of the input laser. In this situation, the amplitude of reflected light can be written as

$$E_r \sim E_0 e^{i\omega t}[r_{FP}(\omega)J_0(\beta) + r_{FP}(\omega+\Omega)J_1(\beta)e^{i\Omega t} - r_{FP}(\omega+\Omega)J_{-1}e^{-i\Omega t}]. \tag{A.13}$$

The power of the reflected light has a constant term and oscillation term of a frequency Ω and 2Ω. By detecting the reflected with a photo detector and demodulating it with a frequency Ω by a Mixer, the obtained voltage signal can be written as follows.

$$V_{PDH} = -\chi q I_{in} \times 2J_0(\beta)J_1(\beta)\mathrm{Im}[r^*_{FP}(\omega)r_{FP}(\omega+\Omega) - r_{FP}(\omega)r^*_{FP}(\omega-\Omega)], \tag{A.14}$$

Where q A/W is an efficiency of photo diode and χ V/A is the efficiency of the mixer and gain of photo diode circuit. If ω is near the resonance frequency ω_0, ω can be written as $\omega = \omega_0 + \delta\omega$. It is also assumed that Ω is large than FWHM. In this situation, the amplitude reflectivity of each frequency can be written as

$$r_{FP}(\omega) \sim r_{FP}(0) + r'_{FP}(0)\delta\omega, \tag{A.15}$$

$$r_{FP}(\omega+\Omega) \sim 0. \tag{A.16}$$

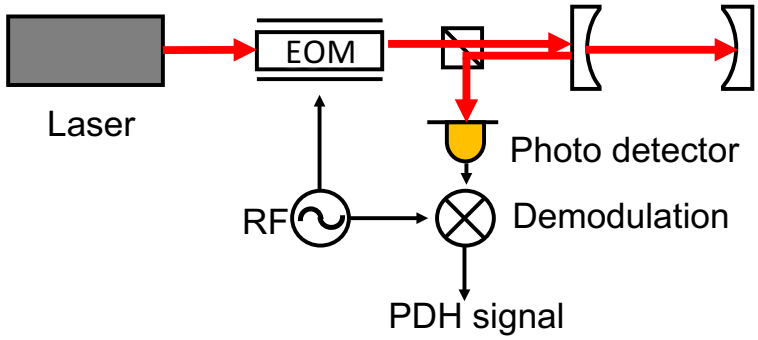

Figure A.3: Schematic of the PDH method. An EOM is used to modulate the input laser frequency. The information of the resonance frequency is implemented on the reflected light from the mirror.

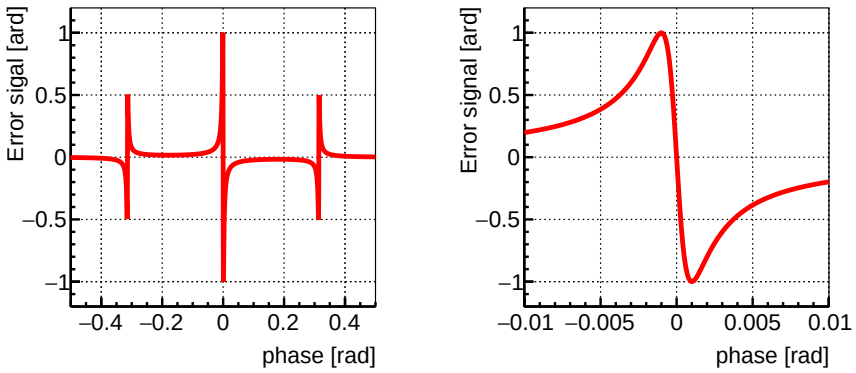

Figure A.4: Example of PDH signal as a function of a phase acquired during the trip between 2 mirrors when $r^2 = 0.999$ and $t^2 = 0.001$. Left:PDH signal in wide phase region. A sharp peak can be seen around the resonance frequency Right: PDH signal enlarged around the resonance frequency. PDH signal almost proportional to the difference between laser frequency and resonance frequency.

By substituting these expressions, the PDH signal becomes

$$\begin{aligned} V_{PDH} &\sim -\chi q I_{in} \times 2J_0(\beta)J_1(\beta)\mathrm{Im}[r'(0)]\delta\omega \\ &= -\chi q I_{in} \times \frac{8t^2 rL}{(1-r^2)^2 c} J_0(\beta)J_1(\beta)\delta\omega \end{aligned} \tag{A.17}$$

Fig. A.4 shows normalized PDH signal. At around the resonance PDH signal is almost proportional to the difference between laser frequency and resonance frequency. Therefore, PDH signal can be used as an error signal for feedback of laser frequency to sustain the resonance of a Fabry-Pérot cavity.

A.2.2 Basic properties of PDH method

In this section, basic properties of PDH method is shown.

The detection limit

As PDH method uses a power of reflected light to extract error signal, its detection limit is defined by the shot noise of reflected light.
By assuming $r^2 + t^2 = 1$, the efficiency of PDH signal can be written as

$$\begin{aligned} V_{PDH} &\sim -\chi q I_{in} \times \frac{8LF}{\pi c} J_0(\beta) J_1(\beta) \delta\omega, \\ &\equiv G_{\mathrm{PDH}} \delta\nu. \end{aligned} \tag{A.18}$$

where $\nu = \frac{\omega}{2\pi}$ and G_{PDH}V/Hz is efficiency of PDH method. At resonance, the DC power of reflected light is

$$I_{DC} \sim 2|J_1(\beta)|^2 I_{in} \tag{A.19}$$

The shot noise $i_{\mathrm{shotnoise}}$ at the photo diode induced with this PD power is

$$i_{\mathrm{shotnoise}} = \sqrt{2eq2|J_1(\beta)|^2 I_{in}}. \tag{A.20}$$

Thus, the minimum frequency difference which can be extracted by PDH method is

$$\begin{aligned} \delta\nu_{\mathrm{min}} &= \frac{\chi \times i_{\mathrm{shotnoise}}}{G_{\mathrm{PDH}}} \\ &= \frac{c}{8J_0(\beta)LF} \sqrt{\frac{e}{qI_{in}}}. \end{aligned} \tag{A.21}$$

Frequency response

For simplicity, let us assume that $r \sim 1$ and $\phi \sim 0$. In this situation, the amplitude reflectance of a Fabry-Pérot cavity can be written as

$$r_{\mathrm{FP}} \sim \frac{i2\phi}{1 - r^2 + i2r^2\phi}. \tag{A.22}$$

When the input laser has small phase noise, the amplitude of the input laser can be written as

$$\begin{aligned} E_{\mathrm{in}} &= E_0 e^{i\omega t + i\phi(t)} \\ &= E_0 e^{i\omega t} + iE_0 e^{i\omega t} \int d\omega' \tilde{\phi}(\omega') e^{i\omega' t}. \end{aligned} \tag{A.23}$$

When the drive frequency of the EOM is larger than FWHM of a Fabry-Pérot cavity, the amplitude of the reflected light from the input mirror becomes as follows,

$$\begin{aligned} E_{\mathrm{r}} = J_0 r_{\mathrm{FP}}(\omega) E_0 e^{i\omega t} + iJ_0 E_0 e^{i\omega t} \int d\omega' r_{\mathrm{FP}}(\omega + \omega') \tilde{\phi}(\omega') e^{i\omega' t} \\ + i\sin(\Omega t) J_1 E_{\mathrm{in}}. \end{aligned} \tag{A.24}$$

When the input laser frequency satisfies the resonance condition, the intensity of the reflected light can be written as

$$I_{\mathrm{r}} = I_0|J_0 r_{\mathrm{FP}}(\omega) + iJ_0 \int d\omega' r_{\mathrm{FP}}(\omega')\tilde{\phi}(\omega')e^{i\omega' t} + i\sin(\Omega t)J_1|^2. \tag{A.25}$$

By demodulating reflected power by $\sin(\Omega t)$, we can obtain the error signal as

$$\begin{aligned} V_{\mathrm{err}} &\propto 4J_0J_1 \int d\omega' r_{\mathrm{FP}}(\omega')\tilde{\phi}(\omega')e^{i\omega' t} \\ &= 4J_0J_1 \int d\omega' \frac{i\frac{2F}{\pi}\frac{\omega' L}{c}}{1+\frac{2F}{\pi}\frac{\omega' L}{c}}\tilde{\phi}(\omega')e^{i\omega' t} \\ &\propto \int d\omega' \frac{1}{1+i\frac{\omega'}{2\pi f_c}}\nu(\omega')e^{i\omega' t}. \end{aligned} \tag{A.26}$$

At the last line in the above equation, the cavity pole frequency f_c is defined as

$$f_c = \frac{c}{4FL}, \tag{A.27}$$

which defines a typical time constant of a Fabry-Pérot cavity.

From these expression, one can see that the PDH signal acts as a 1st order lowpass filter against the frequency noise and its cutoff frequency is f_c.

Appendix B

Birefringent Fabry-Pérot Cavity

This section shows the basic knowledge of the birefringent Fabry-Pérot cavity. As mirrors have small but non-zero birefringence, a Fabry-Pérot cavity itself behaves as a birefringence material. The birefringence of the cavity leads a polarization dependence of the resonance frequency, attenuation of VMB signal and additional dynamical. The dynamic behavior of the Fabry-Pérot cavity against VMB signal in the heterodyne detection scheme is originally discussed in [53]. In this section, dynamical behavior of birefringence cavity in the case of the homodyne detection scheme with static mirror's birefringence is derived.

B.1 Mirrors as a birefringence material

To take into account the birefringence of the mirror, it is assumed that each mirror has phase retardation α_i (i = 1,2) and placed with incident angles θ_i (i=1,2) against the polarization angle of the input laser. These 2 mirrors can be described as one equivalent waveplate whose phase retardation is α_{eq} and incident angle is θ_{eq}. α_{eq} [43]. θ_{eq} is expressed by α_i and θ_i as

$$\alpha_{\mathrm{eq}} = \sqrt{(\alpha_1 - \alpha_2)^2 + 4\alpha_1\alpha_2\cos^2(\theta_1 - \theta_2)}, \tag{B.1}$$

$$\theta_{\mathrm{eq}} = \frac{1}{2}\arccos\left(\frac{\frac{\alpha_1}{\alpha_2} + \cos(2(\theta_1 - \theta_2))}{\sqrt{(\frac{\alpha_1}{\alpha_2} - 1)^2 + 4\frac{\alpha_1}{\alpha_2}\cos^2(\theta_1 - \theta_2)}}\right). \tag{B.2}$$

To taken into account the birefringence of mirrors, the Jones matrix for the reflection by mirror should be modified. From above discussion, it can be interpreted for each reflection, each mirrors acts as a waveplate whose phase retardation is $\alpha' \equiv \frac{\alpha_{\mathrm{eq}}}{2}$, and its angle is θ_{eq}. Thus, the Jones matrix should be modified as follows.

$$R = re^{i\phi}\begin{pmatrix} e^{-i\alpha'/2}\cos^2(\theta_{\mathrm{eq}}) + \mathrm{e}^{\mathrm{i}\alpha'/2}\sin^2(\theta_{\mathrm{eq}}) & -i\sin(\alpha'/2)\sin(2\theta_{\mathrm{eq}}) \\ -i\sin(\alpha'/2)\sin(2\theta_{\mathrm{eq}}) & e^{-i\alpha'/2}\sin^2(\theta_{\mathrm{eq}}) + \mathrm{e}^{\mathrm{i}\alpha'/2}\cos^2(\theta_{\mathrm{eq}}) \end{pmatrix}. \tag{B.3}$$

B.2 resonance frequency splitting

A unique feature of mirror birefringence is that the resonance frequency of the cavity depends on the polarization. In VMB measurement, the laser frequency is lock to the resonance frequency of input polarization where the signal light is orthogonal to the input polarization. Therefore, the signal light is slightly off resonance and it leads to the attenuation of the signal. To take into account these effects, the signal should be calculated with taking into account the mirror birefringence. In basic calculation is done by PVLAS experiment with the assumption that $\theta_{eq} = 0$ [53]. In this experiment θ_{eq} is small but non-zero. Therefore, we assume that the θ_{eq} is non-zero but we can ignore higher order term of θ_{eq}.

When $\theta_{\rm eq}$ is satisfies $1 \gg \theta_{\rm eq}$, the Jones Matrix for the reflection can be approximated as

$$R \sim re^{i\phi} \begin{pmatrix} e^{-i\alpha'/2} & -i\sin(\alpha'/2) \times 2\theta_{\rm eq} \\ -i\sin(\alpha'/2) \times 2\theta_{\rm eq} & e^{i\alpha'/2} \end{pmatrix}. \tag{B.4}$$

These mirrors are used to generate static birefringence term in ellipticity. Thus, the amplitude of ordinary light becomes as follows,

$$\begin{aligned}
\boldsymbol{E}_t &= A_t T_{\rm out} T_{\rm in} \sum_n^{\infty} (RX)^{2n} X \boldsymbol{E}_{in} \\
&= A_t t^2 e^{i\phi} (\boldsymbol{I} - (RX)^2)^{-1} X \boldsymbol{E}_{in} \\
&\sim A_t t^2 e^{i\phi} \begin{pmatrix} 1 - r^2 e^{i(2\phi - \alpha')} & ir^2 e^{i2\phi}(2\Psi e^{-i\alpha'} + \sin(\alpha')2\theta_{\rm eq}) \\ ir^2 e^{i2\phi}(2\Psi e^{i\alpha'} + \sin(\alpha')2\theta_{\rm eq}) & 1 - r^2 e^{i(2\phi+\alpha')} \end{pmatrix}^{-1} \boldsymbol{E}_{in} \\
&\sim \frac{A_t t^2 e^{i\phi}}{(1 - r^2 e^{i(2\phi-\alpha')})(1 - r^2 e^{i(2\phi+\alpha')})} \\
&\quad \begin{pmatrix} 1 - r^2 e^{i(2\phi - \alpha')} & -ir^2 e^{-i2\phi}(2\Psi e^{-i\alpha'} + \sin(\alpha')2\theta_{\rm eq}) \\ -ir^2 e^{-i2\phi}(2\Psi e^{i\alpha'} + \sin(\alpha')2\theta_{\rm eq}) & 1 - r^2 e^{i(2\phi+\alpha')} \end{pmatrix} \boldsymbol{E}_{in} \\
&= \begin{pmatrix} \frac{t^2 e^{i\phi}}{1 - r^2 e^{2\phi + \alpha'}} \\ 0 \end{pmatrix}.
\end{aligned} \tag{B.5}$$

The amplitude of extraordinary light becomes as follows,

$$\begin{aligned}
\boldsymbol{E}_e &= A_e T_{\rm out} T_{\rm in} \sum_n^{\infty} (RX)^{2n} X \boldsymbol{E}_{in} \\
&= A_t t^2 e^{i\phi} (\boldsymbol{I} - (RX)^2)^{-1} X \boldsymbol{E}_{in} \\
&\sim \begin{pmatrix} 0 \\ \frac{t^2 e^{i\phi}}{1 - r^2 e^{2\phi+\alpha'}} \frac{-ir^2 e^{-i2\phi}(2\Psi e^{i\alpha'} + \sin(\alpha')2\theta_{\rm eq})}{1 - r^2 e^{2\phi - \alpha'}} \end{pmatrix}.
\end{aligned} \tag{B.6}$$

From Eq. (B.5), the cavity is on resonance when $\phi - \frac{\alpha_{eq}}{4} = m\pi$ ($m \in \mathbb{Z}$). When cavity is on the resonance, the measured ellipticity becomes as,

$$\begin{aligned}\frac{I_e}{I_t}(t) &= \frac{\left(\frac{F}{\pi}\right)^2}{1-(\frac{2F}{\pi})^2\sin^2(\frac{\alpha_{\rm eq}}{2})}[\sin(\alpha')2\theta_{\rm eq}e^{-i\alpha'} + 2\Psi(t)]^2 \\ &\equiv k(\alpha_{\rm eq})^2[\Gamma e^{-i\frac{\alpha_{\rm eq}}{2}} + \psi]^2 \\ &\sim k(\alpha_{\rm eq})^2(\Gamma^2 + 2\Gamma\psi).\end{aligned} \tag{B.7}$$

In the last line of above expression, the attenuation factor $k(\alpha_{eq})^2$ is defined as $k(\alpha_{eq}) = \frac{1}{1+(\frac{2F}{\pi})^2\sin(\alpha_{\rm eq}/2)}$. As its depends on the birefringence of the mirrors, the birefringence of the mirrors induces the attenuation of the ellipticity. This is understood as follows. Due to the birefringence of the mirror, the optical pass length of the mirrors depends on the polarization. This leads to the polarization dependent resonance frequency. Now, it is assumed that input polarization is almost aligned to the eigen mode of the resonance frequency. Thus, the ordinary light and extraordinary light in on the difference mode of resonance frequency. Thus, the ellipticity is attenuated when ordinary light is on the resonance. In previous research, it is measured that $\alpha_{\rm EQ} \sim 10^{-6}$ rad [53]. In Fig. B.1, an example of the transmittance of ordinary light from a Fabry-Pérot cavity and ellipticity signal is shown. The used parameters are $F = 300,000$ and $\alpha_{\rm EQ} = 4 \times 10^{-6}$ [rad]. These transmittance can not be 1 at the same time.

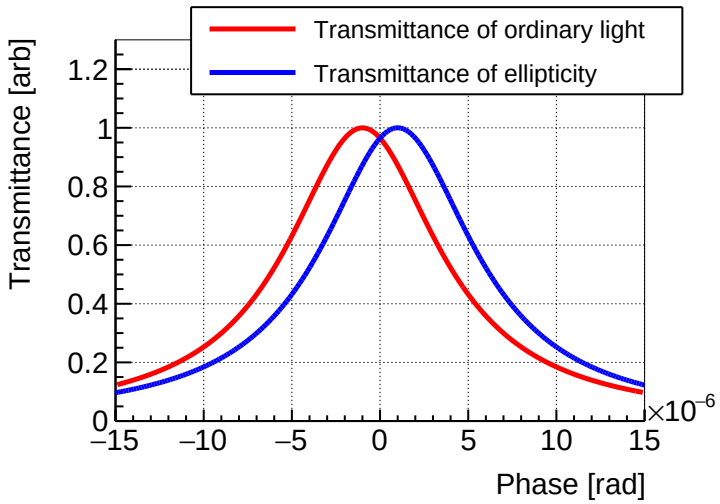

Figure B.1: Example of the signal attenuation by birefringence of the mirrors. Red: The transmittance of the ordinary light of a Fabry-Pérot cavity. Blue: transmittance of ellipticity signal from a Fabry-Pérot cavity. The used parameters are $F = 300,000$ and $\alpha_{\rm EQ} = 4 \times 10^{-6}$ rad

B.3 Frequency response of a Fabry-Pérot cavity against the ellipticity

In this section ,the frequency response of a Fabry-Pérot cavity towards an ellipticity which is not discussed in Section 2 is discussed. The frequency response of the Fabry-Pérot cavity when the birefringence of the mirrors is also considered. The frequency response of a Fabry-Pérot cavity against the VMB signal with non-zero mirror birefringence is originally discussed in [53] in the case of the heterodyne detection scheme. In this section, we derive the frequency response for homodyne setup. In addition to that, the frequency response against input power modulation and frequency modulation is also derived. Because of the non zero static ellipticity generated in the mirror, the results are slightly different compared to [53].

VMB signal

From Eq. B.4, it is approximated that for one round trip during the mirror, $-i(\sin(\alpha'/2) \times 2\theta_{\rm eq} + 2\Psi(t))E_{\rm intra}$ appears as the amplitude of extraordinary light where $E_{\rm intra}$ is the amplitude of the ordinary light in the cavity. It is also approximated that after n-th round trip, the relative phase delay which the extraordinary light acquires against the ordinary light is $n\alpha$.

The amplitude of the extraordinary light transmitted from cavity at time t is sum of the amplitude of the extraordinary light generated before $t - n \times \frac{2L}{c}$ and reflected n-th times. When cavity is on the resonance, the transmitted light can be written as follows,

$$\begin{aligned}
E^e_{out}(t) &= it_m\Sigma(r_m^2 e^{-\alpha_{\rm eq}})^j \times \\
&\left((\sin(\alpha_{\rm eq}/2) \times 2\theta_{\rm eq} + 2\Psi(t - \frac{2L}{c}j)\right) E^t \\
&= it_m\Sigma(r_m^2 e^{-\alpha_{\rm eq}})^j \times \\
&\left((\sin(\alpha_{\rm eq}/2) \times 2\theta_{\rm eq} + 2\int d\omega\Psi(\omega)e^{-i\omega(t-\frac{2L}{c}j)}\right) E^t \\
&= it_m E^t \times (\frac{\sin(\alpha_{\rm eq}/2) \times 2\theta_{\rm eq}}{1 - r_m^2 e^{-i\alpha_{\rm eq}}} + \int d\omega \frac{2\Psi(\omega)e^{i\omega t}}{1 - r_m^2 e^{-i(\alpha_{\rm eq} - 2\frac{2L}{c}\omega)}}) \\
&= E_{\rm in}\frac{F}{\pi}(\frac{\sin(\alpha_{\rm eq}/2) \times 2\theta_{\rm eq}}{1 + i\frac{F}{\pi}\alpha_{\rm eq}} + \int d\omega \frac{2\Psi(\omega)e^{i\omega t}}{1 + i\frac{F}{\pi}(\alpha_{\rm eq} - \frac{2L}{c}\omega)}) \\
&= E_{\rm in}(\frac{\Gamma}{1 + i\frac{F}{\pi}\alpha_{\rm eq}} + \int d\omega \frac{\psi(\omega)e^{i\omega t}}{1 + i\frac{F}{\pi}(\alpha_{\rm eq} - \frac{2L}{c}\omega)}).
\end{aligned} \tag{B.8}$$

From, above equation, the elliptivity can be written as follows

$$\begin{aligned}
I_e/I_t &= |E^e_{out}|/|E^t_{out}| \\
&= k(\alpha)\Gamma^2 + 2\Gamma\int d\omega H(\omega)\Psi(\omega)e^{i\omega t},
\end{aligned} \tag{B.9}$$

where $H(\omega)$ is defines as

$$H(\omega) = \frac{\frac{F}{\pi}}{(1 - i\frac{F}{\pi}\alpha_{\mathrm{eq}})(1 + i\frac{F}{\pi}(\alpha_{\mathrm{eq}} - \frac{2L}{c}\omega))} + \frac{\frac{F}{\pi}}{(1 + i\frac{F}{\pi}\alpha_{\mathrm{eq}})(1 - i\frac{F}{\pi}(\alpha_{\mathrm{eq}} + \frac{2L}{c}\omega))}. \tag{B.10}$$

When α_{eq} is 0, $H(\omega)$ reduces to 1st order low-pass filter as discussed in Chapter 2, and when ω is 0, $H(\omega)$ becomes $\frac{2F}{\pi}k(\alpha)$ as discussed in Chapter B.2.

intensity noise or modulation

For simplicity, it is assumed that the birefringence inside the mirror is all static and it is denoted as γ. The extraordinary light from the Fabry-Pérot cavity can be calculated as

$$\begin{aligned} E^e_{out} &\sim it_{\mathrm{e}}\Sigma(r_{\mathrm{e}}^2 e^{i\alpha_{\mathrm{eq}}})^j \times 2\gamma E^t e^{ij2\phi} \\ &= i2\gamma \frac{t_{\mathrm{e}}}{1 - r_{\mathrm{e}}^2 e^{i\alpha_{\mathrm{eq}}+2\phi}} E_t. \end{aligned} \tag{B.11}$$

where t_{e} and r_{e} is the transmittance and reflectance against extraordinary light, and ϕ is acquired phase for each trip. E_{t} is the amplitude of the ordinary light inside the cavity and it can be written as follows,

$$E^{\mathrm{t}} = \frac{t_{\mathrm{t}} e^{i\phi}}{1 - r_{\mathrm{t}}^2 e^{i2\phi}} E_{\mathrm{in}}, \tag{B.12}$$

where t_{e} and r_{e} is the transmittance and reflectance against ordinary light and E_{in} is the amplitude of the input light. For simplicity, it is also assumed that $r_{\mathrm{e}} = r_{\mathrm{t}}$ and $t_{\mathrm{e}} = t_{\mathrm{t}}$. From these equations, the amplitude of the extraordinary light can be expressed by the E_{in} and ϕ as follows,

$$\begin{aligned} E^{\mathrm{e}} &\sim i2\gamma \frac{t_{\mathrm{e}}}{1 - r_{\mathrm{e}}^2 e^{i2\phi}} \frac{t_{\mathrm{t}}}{1 - r_{\mathrm{t}}^2 e^{i2\phi}} E_{\mathrm{in}} \\ &\sim i2\gamma \frac{\frac{t}{1-r^2}}{1 - i\frac{r^2(\alpha_{\mathrm{eq}}+2\phi)}{1-r^2}} \frac{\frac{t}{1-r^2}}{1 - i\frac{2r^2\phi}{1-r^2}} E_{\mathrm{in}} \\ &\equiv i\Gamma t_{\mathrm{FP}}(\omega) h_{\mathrm{FP}}(\omega) E_{\mathrm{in}}. \end{aligned} \tag{B.13}$$

In the last line it is defined as $\Gamma \equiv \frac{2F}{\pi}$ and t_{FP} defined in Appendix. A is used. $h_{\mathrm{FP}}(\omega)$ is defined as

$$h_{\mathrm{FP}}(\omega) \equiv \frac{1}{1 - i\frac{r^2(\alpha_{\mathrm{eq}}+2\phi)}{1-r^2}}. \tag{B.14}$$

When the input power is modulated at Ω and its modulation is small, the

amplitude can be expressed as

$$\begin{aligned} E_{\text{in}} &= E_0 + E_1 \sin(\Omega t) \\ &= \int d\Omega' \left(E_0 \delta(0) + \frac{E_1}{2i} (\delta(\Omega' - \Omega) - \delta(\Omega' - \Omega) \right)) e^{i\Omega' t} \\ &\equiv \int d\Omega' \left(E_0 \delta(0) + \tilde{E}_1(\Omega') \right)) e^{i\Omega' t} \end{aligned} \tag{B.15}$$

where $E_1 \ll 1$. When input light is on the resonance and modulation frequency is small enough compared to FSR, the power of the extraordinary light becomes as follows,

$$\begin{aligned} I_e &= \Gamma^2 \left| \int d\Omega' t_{\text{FP}}(\Omega') h_{\text{FP}}(\Omega') \left(E_0 \delta(0) + \tilde{E}_1(\Omega') \right) e^{i\Omega' t} \right| \\ &= \Gamma^2 \left| t_{\text{FP}}(0) h_{\text{FP}}(0) E_0 + \int d\Omega' t_{\text{FP}}(\Omega') h_{\text{FP}}(\Omega') \tilde{E}_1(\Omega') e^{i\Omega' t} \right|^2 \\ &= k(\alpha) \Gamma^2 E_0^2 + \Gamma^2 \int d\Omega' \left(h^*_{\text{FP}}(0) t_{\text{FP}}(\Omega') h_{\text{FP}}(\Omega') + h_{\text{FP}}(0) t^*_{\text{FP}}(-\Omega') h^*_{\text{FP}}(-\Omega') \right) E_0 \tilde{E}_1(\Omega') e^{i\Omega' t} \\ &\equiv k(\alpha) \Gamma^2 E_0^2 + 2 \int d\Omega' T_{\text{FP}}(\Omega) E_0 \tilde{E}_1(\Omega') e^{i\Omega' t}, \end{aligned} \tag{B.16}$$

in the last line, the transfer function from input power modulation to the power of extraordinary light modulation is defined as

$$\begin{aligned} T_{\text{FP}}(\Omega) = \Gamma^2 &\frac{1}{2(1 + i\frac{F}{\pi}\alpha_{\text{eq}})(1 - i\frac{F}{\pi}\alpha_{\text{eq}} - i\frac{f}{f_c})(1 - i\frac{f}{f_c})} \\ + \Gamma^2 &\frac{1}{2(1 - i\frac{F}{\pi}\alpha_{\text{eq}})(1 + i\frac{F}{\pi}\alpha_{\text{eq}} - i\frac{f}{f_c})(1 - i\frac{f}{f_c})}. \end{aligned} \tag{B.17}$$

where $f = \frac{\Omega}{2\pi}$ and $f_{\text{c}} = \frac{c}{4FL}$.

From above equation, when α_{eq} is 0, it is shown that a Fabry-Pérot acts as the 2nd order low-pass filter against the input intensity modulation whose cutoff frequency is f_c. This result is consistent with previous calculation [57].

In the same way, the transfer function from the intensity noise of I_{t} to the intensity noise of I_{e} can be derived as follows,

$$\begin{aligned} T_{\text{FP}}(\Omega) = \Gamma^2 &\frac{1}{2(1 + i\frac{F}{\pi}\alpha_{\text{eq}})(1 - i\frac{F}{\pi}\alpha_{\text{eq}} - i\frac{f}{f_c})} \\ + \Gamma^2 &\frac{1}{2(1 - i\frac{F}{\pi}\alpha_{\text{eq}})(1 + i\frac{F}{\pi}\alpha_{\text{eq}} - i\frac{f}{f_c})}. \end{aligned} \tag{B.18}$$

This expression becomes a first order low-pass filter against whose cutoff frequency is f_c when $alpha_{\text{eq}} = 0$. This result is consistent with previous calculation [57].

frequency noise or modulation

In the same way as the intensity modulation, the frequency response against the laser frequency modulation can be also calculated.

It is assumed that the input laser is injected to the Fabry-Pérot cavity and its frequency is slightly detuned from its resonance frequency and is detuned phase is ϕ_0. In this situation, the amplitude of the input laser becomes as follows,

$$E_{\rm in} = E_0 e^{i\omega t}(1 + i\phi(t)), \tag{B.19}$$

The output intensity of the extraordinary light can be written as follows,

$$I^e = const + \int df H_{\rm FP}(f)\tilde{\nu}(f)e^{-2\pi ft}, \tag{B.20}$$

where $H_{\rm FP}$ is the transfer function of the input laser frequency modulation $\nu \equiv \frac{1}{2\pi}\frac{d\phi(t)}{dt}$ to the intensity of the extraordinary light.

$$\begin{aligned} H_{\rm FP}(f) = &\frac{\Gamma^2/f}{2(1+i\frac{2F}{\pi}\phi_0)(1+i\frac{F}{\pi}\alpha_{\rm eq})(1-i\frac{f}{f_c}-i\frac{2F}{\pi}\phi_0-i\frac{F}{\pi}\alpha)(1-i\frac{f}{f_c}-i\frac{2F}{\pi}\phi_0)} \\ &- \frac{\Gamma^2/f}{2(1-i\frac{2F}{\pi}\phi_0)(1-i\frac{F}{\pi}\alpha_{\rm eq})(1-i\frac{f}{f_c}+i\frac{2F}{\pi}\phi_0+i\frac{F}{\pi}\alpha)(1-i\frac{f}{f_c}+i\frac{2F}{\pi}\phi_0)}. \end{aligned} \tag{B.21}$$

Appendix C

Charging unit

This Chapter describes the basic properties of the charging unit. which is originally developed for the ALPs search at SPring 8.

C.1 Basic specifications

The charging unit consists with the capacitor and the control unit. Figure C.1 shows the picture of the overview of the charging unit and that of the capacitor unit. Table C.1 summaries the specification of the charging unit.

Table C.1: Specification of the charging unit

parameter	values [unit]
size (control unit)	1 m × 1.5 m × 2 m
size (capacitor)	2 m × 2 m × 1 m
Capacitance	3 mF
maximum charged voltage	± 4.5 kV
detector noise	3.5×10^{-21}
number of the control unit	2

C.2 Operation sequence

Figure shows the schematic view of the circuit of the charging unit. The unit has two type of switches. One is the mechanical relay (R_c) controlling the charging of the capacitor, the the other is the thyristors (T_1, T_2) to control the discharge to the magnet. R_c controls the start, stop and the sign (positive /negative) of the charging to the capacitor. The feature of this unit is that it has two anti-parallel thyristors. They are normally opened, and the direction of the following current

Figure C.1: Picture of the charging unit. Right: Overview of the charging unit. It consists of the control unit and capacitor unit. Left: Picture of the capacitor. The capacitor unit consists of total 12 capacitors whose capacitance is 0.25 mF.

can be determined by closing one of them selectively. The operation of the charging unit when the repetitive operation mode is selected is designed as follows,

1. all switched are opened.
2. R_c is closed to charge the positive voltage. R_c is opened when the charged voltage reaches to the pre-defined value.
3. T_1 is closed and the pulse field is generated. A part of the current is consumed as the joule heating, the residual returns to the capacitor. It charges the capacitor in the negative direction automatically.
4. T_1 is opened. R_c is closed to charge the negative voltage.
5. T_2 is closed, and the negative pulse field is generated. A part of the current is consumed as the joule heating, the residual returns to the capacitor again. It charges the capacitor in the positive direction automatically.

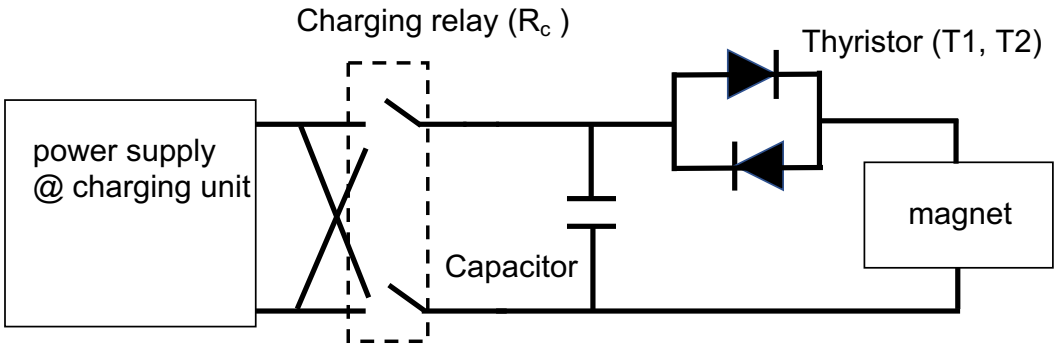

Figure C.2: Schematic view of the charging unit. The unit has 2 switches. One is the charging relay (R_c) to control the charging to the capacitor. The other is thyristors (T_1, T_2) to control the discharge to the magnet.

Appendix D

Discussion of the possible birefringence noise source

In this section, the possible candidate of the noise source which could explain the observed noise excess is discussed.

D.1 Evaluation of the correlation with other possible noise source

There are other possible and reported noise source which induce the optical pass length difference noise, although the transfer mechanism is not understood. As there is no theoretical prediction of their transfer function, the coherence between obtained noise spectrum and possible noise source is studied.

Mechanical vibration of the system

In previous experiment, it is observed the seismic motion of the optical bench induce the optical pass length difference noise [58]. To study the possibility of this coupling, the displacement noise of the system and its coherency with the birefringence noise is studied. The setup is composed with 5 mechanically isolated parts. As an example, the measured displacement spectrum of the optical bench is shown in left side of Fig. D.1. From these displacement spectrums, the coherence spectrum with the optical pass length difference noise is calculated. The result is shown in the right side of Fig. D.1. Except for the sharp peaks around 15 Hz and 50 Hz, no strong coherence can be observed. The coherence between measured noise and quantization noise of ADC which is totally uncorrelated with the measured noise is drawn for comparison. In the same way, the coherence spectrum between 4 mechanically isolated part of the setup is measured. The result is shown in Fig. D.2. Again, no strong coherence is observed between measured noise and displacement noise of the system. From these measurements, it can be conclude that the displacement noise is not the origin of the noise excess.

Input beam pointing

The coherence between the pointing fluctuation of reflected light from the input mirror and birefringence noise is observed in previous experiment [59] with lower finesse configuration. They assume that the input beam angle fluctuation couples with birefringence of the coating. To study this coherence in our setup, the beam pointing fluctuation of reflected beam is monitored with QPD. Figure D.3 shows the measured coherence. Again, no strong coherence has been observed.

Pointing fluctuation on the mirror

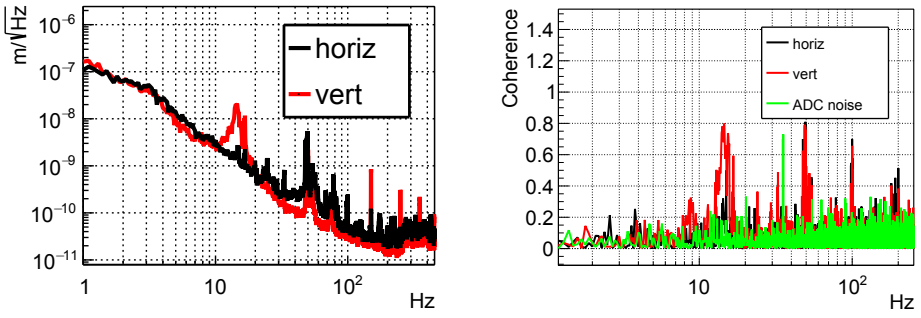

Figure D.1: Left: displacement spectrum of the optical bench. Right: Coherent spectrum between the birefringence noise and displacement noise. No significant coherence can be observed except for some sharp peaks. The coherence between ADC noise and the birefringence noise is also shown as an example of the coherence spectrum between uncorrelated noise.

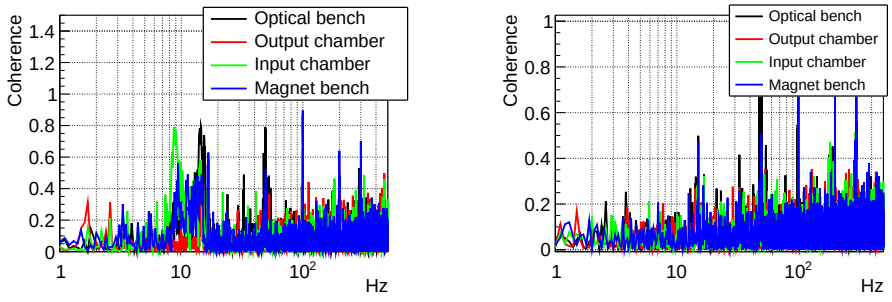

Figure D.2: Left: Coherent spectrum between the birefringence noise and displacement noise of horizontal direction at 4 difference points. Right: coherent spectrum between vertical motion and birefringence noise. Again, no significant coherence can be observed except for some sharp peaks.

Another proposed story to generate additional birefringence noise is pointing fluctuation at the mirror surface couples to non-uniformity of the birefringence of the mirrors' surface [60]. Assuming that birefringence on the mirror depends on the point at the surface, the birefringence acquired after the Fabry-Pérot cavity can be written as

$$\gamma = \gamma_i(X_1, Y_1, X_2, Y_2), \tag{D.1}$$

where (X_i, Y_i) is the point of the center of the laser at the surface of each mirror whose coordinate system is fixed to the surface of each mirror. Assuming that the pointing fluctuation is small enough, the birefringence fluctuation can be written as

$$\Delta\gamma = \frac{\partial\gamma}{\partial X_1}\Delta X_1 + \frac{\partial\gamma}{\partial Y_1}\Delta Y_1 + \frac{\partial\gamma}{\partial X_2}\Delta X_2 + \frac{\partial\gamma}{\partial Y_2}\Delta Y_2, \tag{D.2}$$

where $(\Delta X_i, \Delta Y_i)$ is the pointing fluctuation at each mirror against the coordinate system fix to each mirror's surface. It is also assumed that as mirrors are fix to the optical bench rigidly, the pointing fluctuation $(\Delta X_i, \Delta Y_i)$ is not so much different from the pointing fluctuation $(\delta x_i, \delta y_i)$ whose coordinate system is fixed to the optical bench. After all, the fluctuation of birefringence can be written as follows

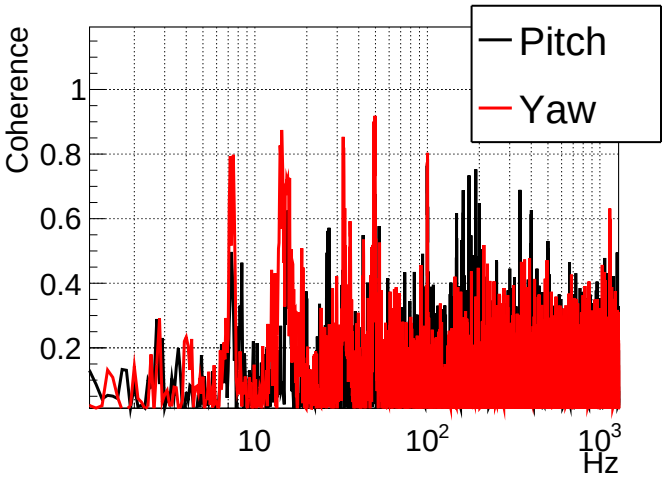

Figure D.3: The coherence spectrum of the birefringence noise spectrum and pointing noise of the reflected light. No strong coherence can be observed except for some sharp peaks.

$$\begin{aligned}\Delta\gamma &= \frac{\partial\gamma}{\partial X_1}\Delta x_1 + \frac{\partial\gamma}{\partial Y_1}\Delta y_1 + \frac{\partial\gamma}{\partial X_2}\Delta x_2 + \frac{\partial\gamma}{\partial Y_2}\Delta y_2 \\ &\equiv \boldsymbol{A}\cdot\begin{pmatrix}\Delta x_1\\ \Delta y_1\\ \Delta x_2\\ \Delta y_2\end{pmatrix}\end{aligned} \tag{D.3}$$

To evaluate the contribution of this effect, the measurement of the pointing fluctuation and $\boldsymbol{A}$ is performed. The conceptual view of this study is shown in Fig. D.4. The pointing fluctuation at each mirror's surface transferred to each QPD by appropriate lense. The coherence spectrum of measured birefringence noise and pointing noise measured at each QPD is shown in Fig. D.5. No strong coherence is observed.

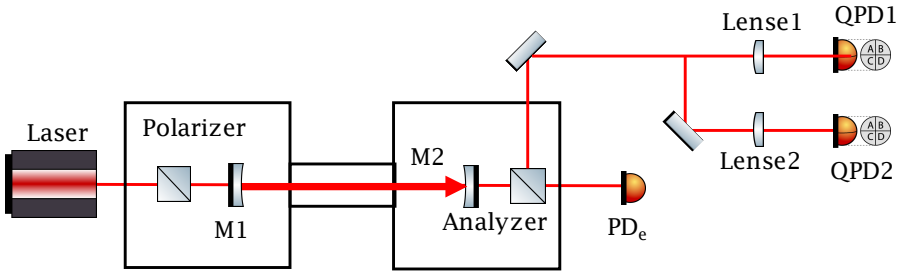

Figure D.4: Schematic view of the set up to study the correlation between the pointing fluctuation and birefringence noise. QPD1 (QPD2) is used to monitor the pointing fluctuation at the M1 (M2). Lense1 (Lense2) is used to transfer the spot at the M1 (M2) to the QPD1 (QPD2).

It should be noted that these measurements just show that at least there are no coherence with birefringence noise and possible noise candidate. The amount of the contribution of these noise to the birefringence noise is still not clear. For future works, the measurement of the transfer function of these noise to the birefringence noise should be performed. In order to perform these measurement, the setup which can modulate the alignment of the mirrors, input pointing and displacement of the system is needed.

D.2 Comparison with thermal noise

The possibility that the thermal noise could become the dominant noise source of VMB search had pointed out by the previous experiment. The measured optical pass length difference noise is compared with the thermal noise derived in

Appendix E. Among the thermal noise discussed in Appendix E, the largest contribution comes from the photo-elastic effect coupling with the brownian motion. Figure D.6 show the comparison between measured noise and theoretical prediction of the thermal noise. Although the spectrum has the same frequency dependence, the observed noise is 10 times larger than the predicted thermal noise level. It should be noted that the thermal noise derived in Appendix E is assuming the isotropic material. There are still possibility that the unexpected anisotropy of the material could induce the birefringence thermal noise.

D.3 Comparison with the lower finesse configuration

Figure D.7 shows the measured optical pass length difference noise with $F \sim 20,000$ and the estimated noise budget around 40 Hz to 2 [kHz]. The setup for the measurement is the same with the setup in chapter 3 except for the reflectance of the mirror. From Fig. D.7, it is clear that the noise budget can explain the measured noise spectrum well. The dominant contribution comes from shot noise and frequency noise. This result supports the validity of the noise estimation around this frequency region. This result also supports the story that the unexpected noise is generated inside a Fabry-Pérot cavity. If the birefringence noise generated outside a Fabry-Pérot cavity, the same noise spectrum with Fig. 3.20 should be appeared in this measurement and as the noise flour is proportional to finesse^{-1}, it should dominate the measured noise spectrum.

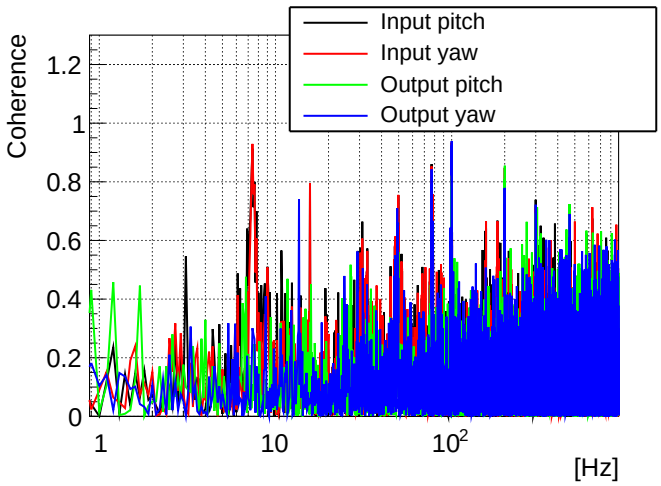

Figure D.5: Coherence spectrum between birefringence noise and measured pointing noise of the mirror. Again, no strong coherence is observed.

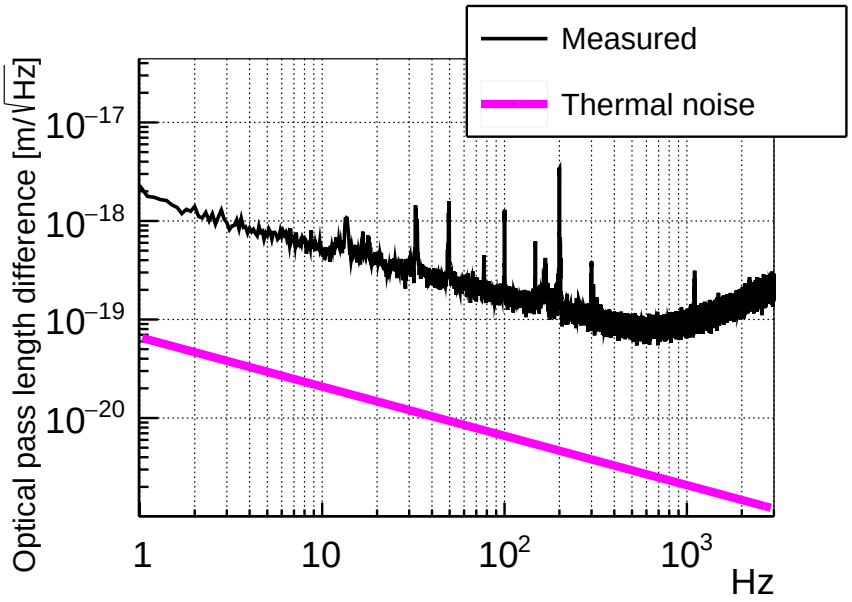

Figure D.6: Comparison between measured noise spectrum and thermal noise calculation. Measured noise is almost 10 times larger than the calculated noise assuming the isotropic material

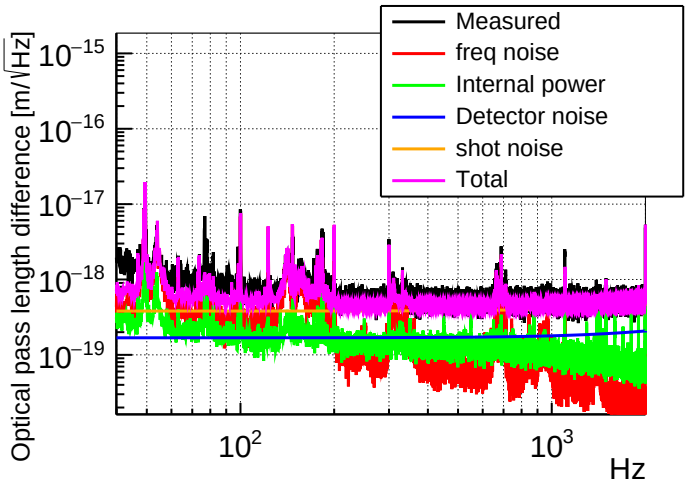

Figure D.7: Measurement of the optical pass length difference measurement with lower finesse cavity and its noise budget.

D.4 Comparison with previous experiment

The noise excess is also reported in the previous experiment. According to [35], the observed noise spectrum in previous experiment can be explained by sum of 2 difference function and it can be written as follows,

$$S(f) = \frac{A}{f \times (1 + (f/f_0)^2)} + \frac{B}{\sqrt{f}} \ [\mathrm{m}^2/\mathrm{Hz}], \tag{D.4}$$

where $A = 4 \times 10^{-36}$, $B = 2.1 \times 10^{-37}$ and $f_0 = 15$. To discuss the possibility that the noise source of each experiment has common origin, the measured noise spectrum in this experiment is fitted with Eq. (D.4) including the contribution of the shot noise at higher frequency by setting A and B as free parameters. The result is shown in Fig. D.8.The red line is the fitting result by Eq. (D.4) including the contribution of the shot noise. One can see that the noise spectrum measured in previous experiment can not explain the noise spectrum in this experiment.

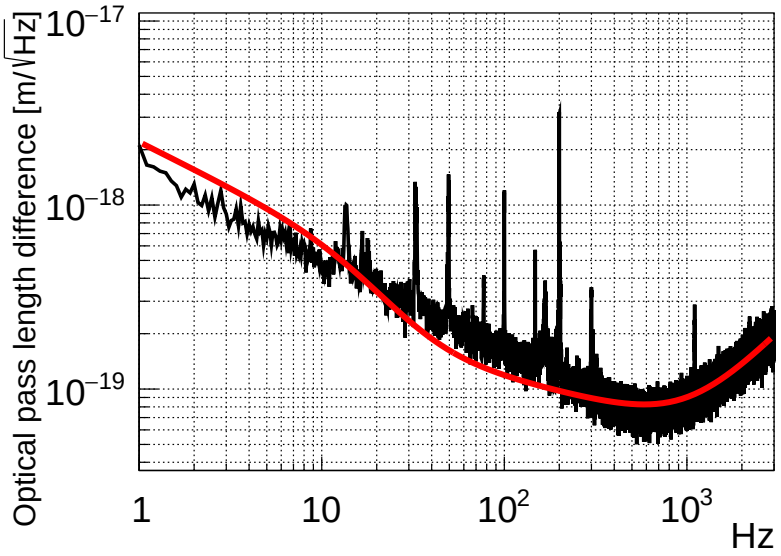

Figure D.8: Comparison with the noise spectrum measured in previous experiment. The black line is measured noise in this experiment. The red line is the fitting result by the Eq. D.4 including the contribution of the shot noise.

D.5 Summary of the noise excess

From the discussion above, the characteristic of the observed noise excess is summarized as follows.

- From the mirror rotation dependence, the noise behaves as birefringence.
- The noise is generated by a Fabry-Pérot cavity
- Thermal noise due to the photo-elastic effect can not explain the observed noise level.
- From the comparison with previous result, the noise spectrum depends on the experimental setup.
- Coherence with vibration noise or pointing noise, which are reported previously is not observed.

Appendix E

Thermal noise

According to the fluctuation dissipation theorem [61], a physical system connected to the thermal bath receive fluctuation from the thermal bath depending on the energy dissipation of the system and the temperature of the thermal bath. As both the substrate and the coating of mirrors have internal mechanical loss and heat loss, physical quantities corresponding to these energy losses fluctuate [62]. The internal mechanical loss results in the shape fluctuation and the heat loss results in the temperature fluctuation of the mirrors. These thermal fluctuation become the cavity length fluctuation which is called thermal noise. It is known thermal noise is the one of the fundamental noise sources of experiments with a Fabry-Pérot cavity [63] including the gravitational wave detectors [64].

In the previous experiment, the possibility that the thermal noise could be the source of the observed noise excess is pointed out [37]. According to the study, the possible candidate is the coupling of the photo elastic effect with strain fluctuation of the mirror. But so far, no theoretical calculation of the thermal noise from the fluctuation dissipation theorem has been performed and only qualitative consideration has been made. In this section, the possible effect of the thermal noise to the birefringence measurement is discussed and the first direct calculation of the birefringence thermal noise due to the photo elastic effect is performed.

E.1 General consideration

In this experiment, what is measured is the optical pass length difference between 2 orthogonal polarization for each round trip inside the cavity ΔL.

$$\Delta L = d \times \Delta n \times \sin(2\theta), \tag{E.1}$$

where Δ n is the birefringence of the material, d is the thickness of the material and θ is the relative angle between the input polarization and the optical axis of the material. It is known that the thermal noise results in the fluctuation of the thickness of the material and the refractive index of the material. The effect of these fluctuation is discussed.

E.2 Effect of thickness fluctuation

Due to the thermal noise, the thickness of the substrate and the coating of the mirror fluctuate. According to Eq. E.1, the thickness fluctuation only in the birefringence material could cause the optical pass length difference noise when input polarization angle against the fast (slow) axis of the mirror is not zero. Although in the previous study, it is assumed that $\theta = 0$, as the coating of the mirrors have birefringence and input polarization angle is not zero in this experiment, the thickness fluctuation of the coating is needed to be concerned.

E.2.1 Brownian noise

Brownian noise is the fluctuation of the mirror's surface due to the internal friction of the material. The power spectrum of the surface displacement of the coating measured by the Gaussian laser is calculated as follows [65],

$$S_x^{\mathrm{B}}(f) = \frac{2k_{\mathrm{B}}T}{\sqrt{\pi^3 f}} \frac{1-\sigma^2}{\omega Y} \phi_{\mathrm{eff}}, \tag{E.2}$$

where Y is the Young modulus, σ is the Poisson's ratio, ω is the radius of the laser and ϕ_{eff} is the effective loss angle of the coating which represent the energy loss in the coating. One can roughly expect that the fluctuation of the optical pass length difference due to this Brownian motion is

$$S_{\Delta L;B}(f) \lesssim S_x^{\mathrm{B}}(f) \times \Delta n_{\mathrm{c}}^2 \ [\mathrm{m}^2/\mathrm{Hz}], \tag{E.3}$$

where $\Delta n_{\mathrm{c}} \sim 10^{-6}$ is the birefringence of the coating.

$S_{\mathrm{x}}^{\mathrm{B}}(f)$ is calculated from the value in Table E.1. From these calculations, the expected effect of the Brownian motion to the optical length difference is

$$\sqrt{S_{\Delta L;B}(f)} \lesssim 6 \times 10^{-24}/f^{1/2} \ [\mathrm{m}/\sqrt{\mathrm{Hz}}]. \tag{E.4}$$

This is negligibly small compared to the shot noise limit sensitivity.

E.2.2 Thermoelastic noise

It is also known that the mirror's surface fluctuates due to the thermal expansion of the material cause by the temperature fluctuation. This thermal noise is called thermoelastic noise [66–68]. The power spectrum density of thermoelastic noise of the coating is calculated as follows,

$$S_x^{\mathrm{TE}}(f) = \frac{8(1+\sigma)^2}{\pi} \frac{\alpha^2 d^2 k_{\mathrm{B}} T^2}{\omega^2 \sqrt{\kappa \rho C f}} \ [\mathrm{m}^2/\mathrm{Hz}]. \tag{E.5}$$

The size of the induced optical pass length difference can be calculated as follows like the previous section,

$$\sqrt{S_{\Delta L;TE}(f)} \lesssim 6 \times 10^{-25}/f^{1/4} \ [\mathrm{m}/\sqrt{\mathrm{Hz}}]. \tag{E.6}$$

This effect can be also neglected compared to the shot noise.

Table E.1: Material parameters used to calculate the thermal noise of mirrors [62]

Parameter(Symbol)	value
Thermal expansion coefficient (α)	3.6×10^{-6} [1/K]
Thermo refractive coefficient (dn/dt)	8×10^{-6} [$1/K$]
Thermal conductivity (κ)	1.38 [W/mK]
Specific heat capacity (C)	745 [J/Kms]
Density (ρ)	2200 [kg/m^3]
Young module (Y)	70 [GPa]
Poisson ratio (σ)	0.17
refractivity (n_0)	1.45
photoelastic coefficient (β)	0.23
Loss angle of the coating (ϕ_c)	3.3×10^{-4}

Table E.2: Material paramters used to calculat the thermal noise of mirrors [62]

Parameter(Symbol)	value
Thermal expansion coefficient (α)	3.6×10^{-6} [1/K]
Thermo refractive coefficient (dn/dt)	14×10^{-6} [$1/K$]
Thermal conductivity (κ)	33 [W/mK]
Specific heat capacity (C)	290 [J/Kms]
Density (ρ)	7200 [kg/m^3]
Young module (Y)	140 [GPa]
Poisson ratio (σ)	0.23
refractivity (n_0)	2.06
Loss angle of the coating (ϕ_c)	3.3×10^{-4}
photoelastic coefficient (β)	0.17

Table E.3: Material parameters used to calculate the thermal noise of mirrors

Parameter(Symbol)	value
Temperature (T)	300 [K]
beam waist (ω)	0.5×10^{-3} [m]
wavelength (μ)	1064 [nm]

E.3 Effect of birefringence fluctuation

E.3.1 Thermorefracrive effect

The refractive index of material depends on the temperature. The thermo-refractive coefficient is defined as

$$\beta \equiv \frac{\partial n}{\partial T}. \tag{E.7}$$

It is known this coefficient couples to the temperature fluctuation of the coating and generates the effective cavity length fluctuation [69]. It power spectrum is

$$S_{\mathrm{x}}^{\mathrm{TR}}(f) = \frac{2k_{\mathrm{B}}T^2}{\pi\omega^2\sqrt{\pi f\kappa\rho C}}\beta^2\lambda^2. \tag{E.8}$$

Though this is not birefringence fluctuation, when the birefringence also depends on the temperature, the birefringence noise could also appear as discussed in [37].

$$S_{\Delta\mathrm{L}}^{\mathrm{TR}}(f) \lesssim \frac{2k_{\mathrm{B}}T^2}{\pi\omega^2\sqrt{\pi f\kappa\rho C}}\beta_{\mathrm{bire}}^2\lambda^2, \tag{E.9}$$

where β_{bire} is defined as

$$\beta_{\mathrm{eff}} \equiv \frac{\partial \Delta n}{\partial T}. \tag{E.10}$$

For now, such a properties of the coating has not been reported. As the static birefringence of the mirror is order of 10^{-6}, It can be guessed that β_{eff} is at least smaller than 10^{-6}. With these assumptions, the amount of $S_{\Delta\mathrm{L}}^{\mathrm{TR}}(f)$ is

$$S_{\Delta\mathrm{L}}^{\mathrm{TR}}(f) < 1.6 \times 10^{-20}. \tag{E.11}$$

This is at least more than 10 times smaller than the measured noise level.

E.3.2 Photoelastic effect of longitudinal strain

The stress applied to the material changes the refractive index of the material. This effect is referred as photoelastic effect [70, 71]. In general, this effect is expressed with the photoelastic tensor p_{ijkl} as

$$\epsilon_{ij}^{-1} = p_{ijkl}\partial_k u_l = p_{ijkl}s_{kl}, \tag{E.12}$$

where ϵ_{ij}^{-1} is inverse permittivity tensor, u_l is the linear displacement and s_{kl} is the stress tensor. Here it is assumed that the photoelastic tensor is an isotropic tensor which can be written as

$$p_{ijkl} = \alpha\delta_{ij}\delta_{kl} + \beta\delta_{ik}\delta_{lj} + \beta\delta_{il}\delta_{kj}, \tag{E.13}$$

First, let us discuss the effect of the longitudinal deformation of the mirror's surface

due to the thermal noise which is well studied in the context of the gravitational wave detectors. Let's assume the light traveling along the z axis and input polarization in along the x axis. In this case the inverse permittivity tensor becomes,

$$\epsilon^{-1} = \begin{pmatrix} 1/n_0^2 + \alpha s_{zz} & 0 \\ 0 & 1/n_0^2 + \alpha s_{zz} \end{pmatrix}. \tag{E.14}$$

The eigen value λ_i of this tensor is

$$\lambda = 1/n_0^2 + \alpha s_{zz}, \tag{E.15}$$

As inverse permittivity tensor has only one eigen value, it is clear that the material is not birefringent.

From these calculations, it is concluded that the as far as the material is isotropic, the longitudinal strain could not induce any birefringence fluctuation. So far, no anisotropy of the photoelastic tensor of the coating of the mirror is reported.

E.3.3 Photoelastic effect of transverse strain

In the previous study, it is pointed out that, in general, the effect of photo elastic effect due to the transverse strain fluctuation of the coating should be about $\left(\frac{l_{\text{coating}}}{\omega}\right)^2$ times smaller comparing effect due to the longitudinal strain, where l_{coating} is thickness of the coating which is much smaller than the beam size [72]. The transverse effect is negligible comparing to the longitudinal effect and has not been calculated so far. Considering birefringence, however, as the longitudinal effect is canceled out, it is needed to take into account the strain in the transverse plane of the mirrors.

Again, it is assumed that the photoelastic tensor is an isotropic tensor which can be written as

$$p_{ijkl} = \alpha\delta_{ij}\delta_{kl} + \beta\delta_{ik}\delta_{lj} + \beta\delta_{il}\delta_{kj}, \tag{E.16}$$

In this situation, the impermiitivity tensor becomes

$$\epsilon^{-1} = \begin{pmatrix} 1/n_0^2 + (\alpha+2\beta)s_{xx} + \alpha s_{yy} & 2\beta s_{xy} \\ 2\beta s_{xy} & 1/n_0^2 + (\alpha+2\beta)s_{yy} + \alpha s_{xx} \end{pmatrix}, \tag{E.17}$$

where the strain in longitudinal direction is ignored.
The induced birefringence can be calculated from the difference of the eigan value λ_i like previous section and it becomes as follows,

$$\Delta n_{\text{t}} = \frac{n_0^3}{2}(\lambda_1 - \lambda_2) = \frac{n_0^3}{2}\beta\sqrt{(s_{xx} - s_{yy})^2 + 4s_{xy}^2}. \tag{E.18}$$

The azimuth angel ϕ of the optical axis of this material satisfies

$$\epsilon^{-1} = \begin{pmatrix} \cos\phi & \sin\phi \\ -\sin\phi & \cos\phi \end{pmatrix} \begin{pmatrix} \lambda_1 & 0 \\ 0 & \lambda_2 \end{pmatrix} \begin{pmatrix} \cos\phi & -\sin\phi \\ \sin\phi & \cos\phi \end{pmatrix}. \tag{E.19}$$

When the input polarization is along the x-axis, the measured optical pass length difference after traveling Δz becomes

$$\Delta l = \Delta z \frac{n_0^3}{2} \times \int (\lambda_1 - \lambda_2) I(z) e^{-2\frac{x^2+y^2}{\omega^2}} \sin(2\phi) dxdy \times \frac{2}{\pi\omega^2}, \tag{E.20}$$

From Eq. (E.19), ϕ satisfies the relation shown below,

$$(\lambda_1 - \lambda_2) \times \frac{1}{2}\sin(2\phi) = \beta s_{xy}. \tag{E.21}$$

By using this relation, the opticl pass length difference can be written as follows,

$$\Delta L = \frac{n_0^3}{2} \times \int 4\beta s_{xy} I(z) e^{-2\frac{x^2+y^2}{\omega^2}} dxdydz \times \frac{2}{\pi\omega^2}. \tag{E.22}$$

As this value is finite in general, the transverse deformation could induce birefringence fluctuation. To estimate the fluctuation of this term, several simplifications is assumed. First, as coating is thin, it is assumed that the strain does not depend on z and the mirror occupies the infinite half plane and its surface locates as $z = 0$. In addition to that, it is assumed that the material parameter of the coating is same with that of the substrate except for the loss angle. It is also assumed that the effective traveling length of the laser for each reflection is z_{eff}. This is calculated later.

As s_{sy} is defined as $s_{xy} = \frac{1}{2}(\partial_x u_y + \partial_y u_x)$, by substituting this relation and perform integration by parts, finally, ΔL becomes as follows,

$$\Delta L = 2\beta z_{\text{eff}} \frac{n_0^3}{2} \times \frac{2}{\pi\omega^2} \times \int (\frac{4y}{\omega^2} u_x + \frac{4x}{\omega^2} u_y) e^{-2\frac{x^2+y^2}{\omega^2}} dxdy. \tag{E.23}$$

When we define the weighting vector $\vec{p}$ as

$$\vec{p} = 2\beta z_{\text{eff}} \frac{n_0^3}{2} \times \frac{2}{\pi\omega^2} \begin{pmatrix} \frac{4y}{\omega^2} \times e^{-2\frac{x^2+y^2}{\omega^2}} \\ \frac{4x}{\omega^2} \times e^{-2\frac{x^2+y^2}{\omega^2}} \\ 0 \end{pmatrix}, \tag{E.24}$$

the optical pass length difference can be written as

$$\Delta L = \int \vec{u}(x, y, z = 0) \cdot \vec{p}\, dxdy \tag{E.25}$$

According to the FDT calculation and Levin's theorem [73], the power spectrum density of ΔL can be calculated by

$$S_{\Delta L} = \frac{2k_B T}{\pi^2 f^2} \frac{W_{\text{diss}}}{F^2}, \tag{E.26}$$

where W_{diss} is dissipated power when force pressure $F\vec{p}\sin(2\pi ft)$ is applied to the surface of the mirror.
In the case of the brownian motion, $W_{\rm diss}$ can be written as

$$W_{\rm diss} = 2\pi f U_{max}\phi, \tag{E.27}$$

where U_{max} is maximum stored energy under the applied pressure. U_{max} can be calculated by solving the elastic equation when applying force pressure $F\vec{p}\sin(2\pi ft)$ at $z = 0$. Finally the power spectrum density becomes as follows,

$$\begin{aligned}\Delta S_{\Delta L}^{\rm BPE} &= \left(2\beta z_{\rm eff}\frac{n_0^3}{2}\right)^2 \times \frac{2k_BT}{\pi^{3/2}f}\frac{(1+\sigma)(2-\sigma)}{\omega^3 Y}\phi_{\rm eff} \\ &= \left(2\beta\frac{n_0^3}{2}\right)^2 \times \left(\frac{z_{\rm eff}}{\omega}\right)^2 \times \frac{2k_BT}{\pi^{3/2}f}\frac{(1+\sigma)(2-\sigma)}{\omega Y}\phi_{\rm eff}.\end{aligned} \tag{E.28}$$

The effective loss angle $\phi_{i\rm eff}$ can be calculated as discussed in [65]. Though coating has larger loss angle, as it is thin, less energy is stored in the coating. Thus the loss angle should be weighted by the ratio of stored energy in each material. The effective loss angle should be written as follows,

$$\phi_{\rm eff} = \phi_{\rm s} + \frac{\delta U}{U}d\phi_{\rm c}, \tag{E.29}$$

where δU is the stored energy in the coating per unit length and U is the total stored energy.

In our case, the $\phi_{\rm eff}$ becomes as follows,

$$\phi_{\rm eff} = \phi_{\rm s} + \frac{4(5-2\sigma)}{(2-\sigma)\sqrt{\pi}}\frac{d}{\omega}\phi_{\rm c}. \tag{E.30}$$

The evaluation of z_{eff} is performed as follows. In the calculation of the thermorefractive noise, the effective length fluctuation when the refractive index of the material of the multi layers fluctuate is calculated as follows [69],

$$\Delta z = \frac{\lambda}{4\pi}\times\delta\phi = \frac{\lambda}{4\pi}\frac{n_1n_2\pi}{n_1^2-n_2^2}\left(n_2\frac{\Delta n_1}{n_1}+n_1\frac{\Delta n_2}{n_2}\right). \tag{E.31}$$

where $\delta\phi$ is the phase delay for each reflection and n_i is the refractive index of the odd or even layer. From this calculation, the phase delay acquired by the light whose polarization is parallel to the fast axis of the material is

$$\delta\phi_{\rm f} = \frac{n_1n_2\pi}{n_1^2-n_2^2}\left(n_2\frac{\Delta n_{1;\rm f}}{n_1}+n_1\frac{\Delta n_{2;\rm f}}{n_2}\right), \tag{E.32}$$

where $\Delta n_{i;f}$ denotes the refractive index fluctuation of the fast axis. And for the light whose polarization is parallel to the slow axis is

$$\delta\phi_{\rm s} = \frac{n_1n_2\pi}{n_1^2-n_2^2}\left(n_2\frac{\Delta n_{1;\rm s}}{n_1}+n_1\frac{\Delta n_{2;\rm s}}{n_2}\right), \tag{E.33}$$

where $\Delta n_{i;s}$ denotes the refractive index fluctuation of the slow axis. As it is assumed that the photoelastic tensor for each material is the same, the angle of fast axis for given stress is the same for each material. The acquired ellipticity for the light whose incident angle is θ is calculated to be

$$\Delta\psi = (\delta\phi_{\rm f} - \delta\phi_{\rm s}) \times \sin(2\theta). \tag{E.34}$$

By the definition of the optical pass length difference (Eq. (2.23)), the optical pass length difference due to this ellipticity is

$$\begin{aligned}\Delta L &= \frac{\lambda}{2\pi}(\delta\phi_{\rm f} - \delta\phi_{\rm s}) \times \sin(2\theta) \\ &= \frac{\lambda}{2\pi} \times \frac{n_1 n_2 \pi}{n_1^2 - n_2^2}\left(\frac{n_1}{n_2}(\Delta n_{2;\rm f} - \Delta n_{2;\rm s}) + \frac{n_2}{n_1}(\Delta n_{1;\rm f} - \Delta n_{1;\rm s})\right) \times \sin(2\theta).\end{aligned} \tag{E.35}$$

By comparing this equation with Eq. E.1, $z_{\rm eff}$ for even (odd) layer can be determined as

$$z_{\rm eff;1} = \frac{\lambda}{4\pi} \times \frac{n_1 n_2 \pi}{n_1^2 - n_2^2}\frac{n_1}{n_2} \tag{E.36}$$

$$z_{\rm eff;2} = \frac{\lambda}{4\pi} \times \frac{n_1 n_2 \pi}{n_1^2 - n_2^2}\frac{n_2}{n_1}. \tag{E.37}$$

After all, the formula to calculate the optical pass length difference noise due becomes as follows,

$$\Delta S_{\Delta L}^{\rm BPE} = \left(2\beta\frac{n_1^3}{2}\frac{z_{\rm eff;1}}{\omega} + 2\beta\frac{n_2^3}{2}\frac{z_{\rm eff;2}}{\omega}\right)^2 \times \frac{2k_B T}{\pi^{3/2} f}\frac{(1+\sigma)(2-\sigma)}{\omega Y}\phi_{\rm eff}. \tag{E.38}$$

E.3.4 Photo-thermo-photo-elastic effect

As mirrors of a Fabry-Pérot cavity has non zero absorption of laser power and the beam profile is not uniform, the absorbed power induce a temperature gradient. This temperature gradient results in the thermal stress and birefringence due to the photo-elastic effect. This phenomenon is called thermal birefringence. The detailed calculation is studied in [70, 71].
For simplicity, let us ignore the longitudinal strain and the strain has an axial symmetry against the z-axis. It is also assumed that the photo elastic tensor is an isotropic tensor which can be written as

$$p_{ijkl} = \alpha\delta_{ij}\delta_{kl} + \beta\delta_{ik}\delta_{kj} + \beta\delta_{il}\delta_{kj}, \tag{E.39}$$

In this situation, when we use cylindrical coordinate (r, θ, z), the impermittivity tensor can be written as

$$\epsilon_{xx}^{-1} = (\alpha+2\beta)(\cos^2\theta s_{rr} + \sin^2\theta s_{\theta\theta}) + \alpha(\sin^2\theta s_{rr} + \cos^2\theta s_{\theta\theta}) \tag{E.40}$$

$$\epsilon_{yy}^{-1} = \alpha(\cos^2\theta s_{rr} + \sin^2\theta s_{\theta\theta}) + (\alpha+2\beta)(\sin^2\theta s_{rr} + \cos^2\theta s_{\theta\theta}) \tag{E.41}$$

$$\epsilon_{xy}^{-1} = 2\beta(s_{rr} - s_{\theta\theta})\sin\theta\cos\theta. \tag{E.42}$$

As we assume the cylindal symmetry, $s_{r\theta} = 0$ and every strain component does not depend on θ.
The eigen value of this tensor is

$$\lambda_1 = 1/n_0^2 + (\alpha(s_{rr} + s_{\theta\theta}) + 2\beta s_{rr}) \tag{E.43}$$
$$\lambda_2 = 1/n_0^2 + (\alpha(s_{rr} + s_{\theta\theta}) - 2\beta s_{\theta\theta}). \tag{E.44}$$

It is also shown that the azimuth angle of the optical axis is θ.

The optical pass length difference is

$$\begin{aligned}\Delta L &= \int \frac{n_0^3}{2} 2\beta(s_{rr} - s_{\theta\theta}) \sin\theta \times e^{-2\frac{2r^2}{\omega^2}} r dr d\theta dz \times \frac{2}{\pi\omega^2} \\ &= 0.\end{aligned} \tag{E.45}$$

In the previous study, it is also shown the stress induced by the TEM 00 beam has axial symmetry. From these calculations, it is shown that as far as the beam profile is axial symmetry, the absorption of the internal power does not induce the optical pass length difference noise. It should be noted in the previous study, the thermal birefringence is not zero. This is because they calculated the square of the electric field of the extraordinary light whereas we are interested in the linear term.

Acknowledgements

First, I would like to express my gratitude to my supervisor Prof. Shoji Asai (the university of Tokyo) for giving me the opportunity of this work and his continuous support and encouragement.

I would also like to express my great gratitude to Assosiate Prof. Toshio Namba (ICEPP, the university of Tokyo). He supported this work from the beginning to the end. His insightful advice always helps me to solve the problems in the best way.

My special thanks go to Dr. Toshiaki Inada (ICEPP, the university of Tokyo) and Takayuki Yamazaki (ex-ICRPP) for their excellent contributions in developing the pulsed magnet system. Without their support, this work could never have been accomplished.

My sincere gratitude goes to Prof Kosuke Yoshioka and President Makoto Kuwata-Gonokami (The university of Tokyo) for their technical support to develop the laser system. I gratefully thank to Prof. Koichi Kindo, Dr. Akira Matsuo, and Dr. Takashi Kawaguchi (ISSP, The University of Tokyo) for their technical advice on development of the pulsed magnet. I would also thank to Prof. Hiroyuki Nojiri (IMR, Tohoku University) for his advice on the design of the magnet and capacitor bank.

I sincerely appreciate Mr. Xing Fan (ex-the university of Tokyo). He is the pioneer of this experiment. After he left this experiment, he continuously encourages me and gives a lot of useful advice.

I would like to thank all the staffs and students of ICEPP and Dept. of Physics at the university of Tokyo for their supports.

Bibliography

[1] W. Heisenberg and H. Euler, Folgerungen aus der Diracschen Theorie des Positrons, Zeitschrift fur Physik **98**, 714–732 (Nov. 1936).

[2] J. J. Klein and B. P. Nigam, Dichroism of the Vacuum, Phys. Rev. **136**, B1540–B1542 (Dec 1964).

[3] A. Di Piazza, K. Z. Hatsagortsyan, and C. H. Keitel, Light Diffraction by a Strong Standing Electromagnetic Wave, Phys. Rev. Lett. **97**, 083603 (Aug 2006).

[4] F. Moulin and D. Bernard, Four-wave interaction in gas and vacuum: definition of a third-order nonlinear effective susceptibility in vacuum: χvacuum(3), Optics Communications **164**(1), 137 – 144 (1999).

[5] Z. Bialynicka-Birula and I. Bialynicki-Birula, Nonlinear Effects in Quantum Electrodynamics. Photon Propagation and Photon Splitting in an External Field, Phys. Rev. D**2**, 2341–2345 (Nov. 1970).

[6] C. A. Baker, D. D. Doyle, P. Geltenbort, K. Green, M. G. D. van der Grinten, P. G. Harris, P. Iaydjiev, S. N. Ivanov, D. J. R. May, J. M. Pendlebury, J. D. Richardson, D. Shiers, and K. F. Smith, Improved Experimental Limit on the Electric Dipole Moment of the Neutron, Phys. Rev. Lett. **97**, 131801 (Sep 2006).

[7] J. M. Pendlebury et al., Revised experimental upper limit on the electric dipole moment of the neutron, Phys. Rev. D **92**, 092003 (Nov 2015).

[8] R. D. Peccei and H. R. Quinn, CP Conservation in the Presence of Pseudoparticles, Phys. Rev. Lett. **38**, 1440–1443 (Jun 1977).

[9] S. Weinberg, A New Light Boson?, Phys. Rev. Lett. **40**, 223–226 (Jan 1978).

[10] F. Wilczek, Problem of Strong P and T Invariance in the Presence of Instantons, Phys. Rev. Lett. **40**, 279–282 (Jan 1978).

[11] H. Leutwyler, The ratios of the light quark masses, Physics Letters B **378**(1), 313 – 318 (1996).

[12] H. Primakoff, Photo-Production of Neutral Mesons in Nuclear Electric Fields and the Mean Life of the Neutral Meson, Phys. Rev. **81**, 899–899 (Mar 1951).

[13] A. Ringwald, Axions and Axion-Like Particles, 2014.

[14] L. Covi, J. E. Kim, and L. Roszkowski, Axinos as Cold Dark Matter, Phys. Rev. Lett. **82**, 4180–4183 (May 1999).

[15] P. Svrcek and E. Witten, Axions in string theory, Journal of High Energy Physics **6**, 051 (June 2006).

[16] J. P. Conlon, The QCD axion and moduli stabilisation, Journal of High Energy Physics **2006**(05), 078–078 (jun 2006).

[17] G. Raffelt and L. Stodolsky, Mixing of the photon with low-mass particles, Phys. Rev. D**37**, 1237–1249 (Mar. 1988).

[18] J. Redondo and A. Ringwald, Light shining through walls, Comtemp. Phys **52**(211) (2011).

[19] A. Nobuhiro, Y. Hirahara, K. Homma, Y. Kirita, T. Ozaki, Y. Nakamiya, M. Hashida, S. Inoue, and S. Sakabe, Extended search for sub-eV axion-like resonances via four-wave mixing with a quasi-parallel laser collider in a high-quality vacuum system, Progress of Theoretical and Experimental Physics **2020**(7) (07 2020), 073C01.

[20] P. Astier et al., Search for eV (pseudo)scalar penetrating particles in the SPS neutrino beam, Physics Letters B **479**(4), 371 – 380 (2000).

[21] K. Ehret, M. Frede, S. Ghazaryan, M. Hildebrandt, E.-A. Knabbe, D. Kracht, A. Lindner, J. List, T. Meier, N. Meyer, D. Notz, J. Redondo, A. Ringwald, G. Wiedemann, and B. Willke, New ALPS results on hidden-sector lightweights, Physics Letters B **689**(4), 149 – 155 (2010).

[22] R. Ballou, G. Deferne, M. Finger, M. Finger, L. Flekova, J. Hosek, S. Kunc, K. Macuchova, K. A. Meissner, P. Pugnat, M. Schott, A. Siemko, M. Slunecka, M. Sulc, C. Weinsheimer, and J. Zicha, New exclusion limits on scalar and pseudoscalar axionlike particles from light shining through a wall, Phys. Rev. D **92**, 092002 (Nov 2015).

[23] T. Inada, T. Yamazaki, T. Namba, S. Asai, T. Kobayashi, K. Tamasaku, Y. Tanaka, Y. Inubushi, K. Sawada, M. Yabashi, T. Ishikawa, A. Matsuo, K. Kawaguchi, K. Kindo, and H. Nojiri, Search for Two-Photon Interaction with Axionlike Particles Using High-Repetition Pulsed Magnets and Synchrotron X Rays, Physical Review Letters **118**(7), 071803 (Feb. 2017).

[24] J. Jaeckel and A. Ringwald, The Low-Energy Frontier of Particle Physics, Annual Review of Nuclear and Particle Science **60**(1), 405–437 (2010).

[25] B. Holdom, Two U(1)'s and χ charge shifts, Physics Letters B **166**(2), 196 – 198 (1986).

[26] S. Davidson, S. Hannestad, and G. Raffelt, Updated bounds on milli-charged particles, Journal of High Energy Physics **2000**(05), 003–003 (may 2000).

[27] S. Chatrchyan et al., Search for fractionally charged particles in *pp* collisions at $\sqrt{s} = 7$ TeV, Phys. Rev. D **87**, 092008 (May 2013).

[28] A. A. Prinz, R. Baggs, J. Ballam, S. Ecklund, C. Fertig, J. A. Jaros, K. Kase, A. Kulikov, W. G. J. Langeveld, R. Leonard, T. Marvin, T. Nakashima, W. R. Nelson, A. Odian, M. Pertsova, G. Putallaz, and A. Weinstein, Search for Millicharged Particles at SLAC, Phys. Rev. Lett. **81**, 1175–1178 (Aug 1998).

[29] A. Badertscher, P. Crivelli, W. Fetscher, U. Gendotti, S. N. Gninenko, V. Postoev, A. Rubbia, V. Samoylenko, and D. Sillou, Improved limit on invisible decays of positronium, Phys. Rev. D **75**, 032004 (Feb 2007).

[30] S. Davidson and M. Peskin, Astrophysical bounds on millicharged particles in models with a paraphoton, Phys. Rev. D **49**, 2114–2117 (Feb 1994).

[31] A. D. Dolgov, S. L. Dubovsky, G. I. Rubtsov, and I. I. Tkachev, Constraints on millicharged particles from Planck data, Phys. Rev. D **88**, 117701 (Dec 2013).

[32] M. Ahlers, H. Gies, J. Jaeckel, and A. Ringwald, Particle interpretation of the PVLAS data: Neutral versus charged particles, Phys. Rev. D **75**, 035011 (Feb 2007).

[33] E. Zavattini, G. Zavattini, G. Ruoso, E. Polacco, E. Milotti, M. Karuza, U. Gastaldi, G. Di Domenico, F. Della Valle, R. Cimino, S. Carusotto, G. Cantatore, and M. Bregant, Experimental Observation of Optical Rotation Generated in Vacuum by a Magnetic Field, Phys. Rev. Lett. **96**, 110406 (Mar 2006).

[34] E. Zavattini, G. Zavattini, G. Ruoso, E. Polacco, E. Milotti, M. Karuza, U. Gastaldi, G. Di Domenico, F. Della Valle, R. Cimino, S. Carusotto, G. Cantatore, and M. Bregant, Editorial Note: Experimental Observation of Optical Rotation Generated in Vacuum by a Magnetic Field [Phys. Rev. Lett. 96, 110406 (2006)], Phys. Rev. Lett. **99**, 129901 (Sep 2007).

[35] A. Ejlli, F. D. Valle, U. Gastaldi, G. Messineo, R. Pengo, G. Ruoso, and G. Zavattini, The PVLAS experiment: a 25 year effort to measure vacuum magnetic birefringence, 2020.

[36] F. Della Valle, A. Ejlli, U. Gastaldi, G. Messineo, E. Milotti, R. Pengo, G. Ruoso, and G. Zavattini, The PVLAS experiment: measuring vacuum magnetic

birefringence and dichroism with a birefringent Fabry-Perot cavity, European Physical Journal C **76**, 24 (Jan. 2016).

[37] G. Zavattini, F. Della Valle, A. Ejlli, W. T. Ni, U. Gastaldi, E. Milotti, R. Pengo, and G. Ruoso, Intrinsic mirror noise in Fabry–Perot based polarimeters: the case for the measurement of vacuum magnetic birefringence, The European Physical Journal C **78**(7), 585 (2018).

[38] A. Cadène, P. Berceau, M. Fouché, R. Battesti, and C. Rizzo, Vacuum magnetic linear birefringence using pulsed fields: status of the BMV experiment, European Physical Journal D **68**, 16 (Jan. 2014).

[39] R. P. Mignani, V. Testa, D. González Caniulef, R. Taverna, R. Turolla, S. Zane, and K. Wu, Evidence for vacuum birefringence from the first optical-polarimetry measurement of the isolated neutron star RX J1856.5-3754, Monthly Notices of the Royal Astronomical Society **465**(1), 492–500 (11 2016).

[40] L. M. Capparelli, A. Damiano, L. Maiani, and A. D. Polosa, A note on polarized light from magnetars, The European Physical Journal C **77**(11), 754 (2017).

[41] K. Kindo, New pulsed-magnets for 100 T, long-pulse and diffraction measurements, Journal of Physics: Conference Series **51**, 522–528 (nov 2006).

[42] M. T. Hartman, A. Rivere, R. Battesti, and C. Rizzo, Noise characterization for resonantly-enhanced polarimetric vacuum magnetic-birefringence experiments, ArXiv e-prints (Dec. 2017).

[43] F. Brandi, F. Della Valle, A. M. De Riva, P. Micossi, F. Perrone, C. Rizzo, G. Ruoso, and G. Zavattini, Measurement of the phase anisotropy of very high reflectivity interferential mirrors, Applied Physics B **65**(3), 351–355 (1997).

[44] F. Herlach, Pulsed magnets, Reports on Progress in Physics **62**(6), 859–920 (jan 1999).

[45] A. Cotton and H. Mouton, Compt. Rend. Acad. Sci. Paris **141**(317) (1905).

[46] H.-H. Mei, W.-T. Ni, S.-J. Chen, and S. shi Pan, Measurement of the Cotton–Mouton effect in nitrogen, oxygen, carbon dioxide, argon, and krypton with the Q & A apparatus, Chemical Physics Letters **471**(4), 216 – 221 (2009).

[47] F. Della Valle, A. Ejlli, U. Gastaldi, G. Messineo, E. Milotti, R. Pengo, L. Piemontese, G. Ruoso, and G. Zavattini, Measurement of the Cotton Mouton effect of water vapour, Chemical Physics Letters **592**, 288 – 291 (2014).

[48] F. Della Valle, E. Milotti, A. Ejlli, G. Messineo, L. Piemontese, G. Zavattini, U. Gastaldi, R. Pengo, and G. Ruoso, First results from the new PVLAS

apparatus: A new limit on vacuum magnetic birefringence, Phys. Rev. D **90**, 092003 (Nov 2014).

[49] P. Berceau, M. Fouché, R. Battesti, and C. Rizzo, Magnetic linear birefringence measurements using pulsed fields, Phys. Rev. A **85**, 013837 (Jan 2012).

[50] A. Cadène, D. Sordes, P. Berceau, M. Fouché, R. Battesti, and C. Rizzo, Faraday and Cotton-Mouton effects of helium at $\lambda = 1064$ nm, Phys. Rev. A **88**, 043815 (Oct 2013).

[51] G. Bialolenker, E. Polacco, C. Rizzo, and G. Ruoso, First evidence for the linear magnetic birefringence of the reflecting surface of interferential mirrors, Applied Physics B: Lasers and Optics **68**, 703–706 (1999).

[52] R. W. P. Drever, J. L. Hall, F. V. Kowalski, J. Hough, G. M. Ford, A. J. Munley, and H. Ward, Laser phase and frequency stabilization using an optical resonator, Applied Physics B **31**(2), 97–105 (1983).

[53] A. Ejlli, F. Della Valle, and G. Zavattini, Polarisation dynamics of a birefringent Fabry–Perot cavity, Applied Physics B **124**(2), 22 (2018).

[54] A. Cadène, *Mesures de biréfringences magnétiques dans l'hélium et le xénon gazeux, et dans le vide*, PhD thesis, University of Toulouse, 2015.

[55] S.-J. CHEN, H.-H. MEI, and W.-T. NI, Q & A EXPERIMENT TO SEARCH FOR VACUUM DICHROISM, PSEUDOSCALAR–PHOTON INTERACTION AND MILLICHARGED FERMIONS, Modern Physics Letters A **22**(37), 2815–2831 (2007).

[56] M. Bregant, G. Cantatore, S. Carusotto, R. Cimino, F. Della Valle, G. Di Domenico, U. Gastaldi, M. Karuza, E. Milotti, E. Polacco, G. Ruoso, E. Zavattini, and G. Zavattini, Measurement of the Cotton–Mouton effect in krypton and xenon at 1064 nm with the PVLAS apparatus, Chemical Physics Letters **392**(1), 276 – 280 (2004).

[57] P. Berceau, M. Fouché, R. Battesti, F. Bielsa, J. Mauchain, and C. Rizzo, Dynamical behaviour of birefringent Fabry–Perot cavities, Applied Physics B **100**(4), 803–809 (2010).

[58] F. Della Valle, G. Di Domenico, U. Gastaldi, E. Milotti, R. Pengo, G. Ruoso, and G. Zavattini, Towards a direct measurement of vacuum magnetic birefringence: PVLAS achievements, Optics Communications **283**(21), 4194 – 4198 (2010).

[59] M. T. Hartman, R. Battesti, and C. Rizzo, Characterization of the Vacuum Birefringence Polarimeter at BMV: Dynamical Cavity Mirror Birefringence, IEEE Transactions on Instrumentation and Measurement **68**(6), 2268–2273 (2019).

[60] M. T. Hartman, A. Rivère, R. Battesti, and C. Rizzo, Noise characterization for resonantly enhanced polarimetric vacuum magnetic-birefringence experiments, Review of Scientific Instruments **88**(12), 123114 (2017).

[61] H. B. Callen and T. A. Welton, Irreversibility and Generalized Noise, Phys. Rev. **83**, 34–40 (Jul 1951).

[62] *Optical Coatings and Thermal Noise in Precision Measurement*, Cambridge University Press, 2012.

[63] M. Notcutt, L.-S. Ma, A. D. Ludlow, S. M. Foreman, J. Ye, and J. L. Hall, Contribution of thermal noise to frequency stability of rigid optical cavity via Hertz-linewidth lasers, Phys. Rev. A **73**, 031804 (Mar 2006).

[64] M. Pitkin, S. Reid, S. Rowan, and J. Hough, Gravitational Wave Detection by Interferometry (Ground and Space), Living Reviews in Relativity **14**(1), 5 (2011).

[65] G. M. Harry, A. M. Gretarsson, P. R. Saulson, S. E. Kittelberger, S. D. Penn, W. J. Startin, S. Rowan, M. M. Fejer, D. R. M. Crooks, G. Cagnoli, J. Hough, and N. Nakagawa, Thermal noise in interferometric gravitational wave detectors due to dielectric optical coatings, Classical and Quantum Gravity **19**(5), 897–917 (feb 2002).

[66] V. Braginsky, M. Gorodetsky, and S. Vyatchanin, Thermodynamical fluctuations and photo-thermal shot noise in gravitational wave antennae, Physics Letters A **264**(1), 1 – 10 (1999).

[67] V. Braginsky and A. Samoilenko, Measurements of the optical mirror coating properties, Physics Letters A **315**(3), 175 – 177 (2003).

[68] M. M. Fejer, S. Rowan, G. Cagnoli, D. R. M. Crooks, A. Gretarsson, G. M. Harry, J. Hough, S. D. Penn, P. H. Sneddon, and S. P. Vyatchanin, Thermoelastic dissipation in inhomogeneous media: loss measurements and displacement noise in coated test masses for interferometric gravitational wave detectors, Phys. Rev. D **70**, 082003 (Oct 2004).

[69] V. Braginsky, M. Gorodetsky, and S. Vyatchanin, Thermo-refractive noise in gravitational wave antennae, Physics Letters A **271**(5), 303 – 307 (2000).

[70] W. Koechner and D. Rice, Effect of birefringence on the performance of linearly polarized YAG:Nd lasers, IEEE Journal of Quantum Electronics **6**(9), 557–566 (1970).

[71] M. Varnham, D. Payne, A. Barlow, and R. Birch, Analytic solution for the birefringence produced by thermal stress in polarization-maintaining optical fibers, Journal of Lightwave Technology **1**(2), 332–339 (1983).

[72] T. Hong, H. Yang, E. K. Gustafson, R. X. Adhikari, and Y. Chen, Brownian thermal noise in multilayer coated mirrors, Phys. Rev. D **87**, 082001 (Apr 2013).

[73] Y. Levin, Internal thermal noise in the LIGO test masses: A direct approach, Phys. Rev. D **57**, 659–663 (Jan 1998).